ABSTRACT

Title of dissertation: TRACKING SPECTRAL CHANGES IN BLAZARS WITH THE ENERGETIC GAMMA RAY EXPERIMENT TELESCOPE (EGRET)

Giridhar Nandikotkur, Doctor of Philosophy, 2007

Dissertation directed by: Professor Jordan Goodman
Department of Physics

I analyze the entire blazar data from the Energetic Gamma Ray Experiment Telescope (EGRET) on board the Compton Gamma Ray Observatory (CGRO), using the skymaps that were regenerated to include the changes in performance during the mission. The sample of 98 sources consists of 66 flat spectrum radio quasars (FSRQs), 17 low-frequency peaked BL Lac objects (LBLs), 4 high-frequency peaked BL Lac objects (HBLs), 10 flat spectrum radio sources and 1 radio galaxy. I do not detect any clear pattern in the variation of spectral index with flux. Some of the blazars do not show any statistical evidence for spectral variability. The spectrum hardens with increasing flux in a few cases. There is also evidence for a flux-hardness anticorrelation at low fluxes in five blazars. I examine the EGRET spectral energy distribution (SED) for all the sources to identify these trends. I also observe a previously unreported spectral hysteresis in the spectral index Vs. flux space at weekly timescales, in all the three FSRQs for which data from flares lasting 3-4 weeks were available. All three sources show a counterclockwise rotation despite the widely

different flux profiles. The time-averaged spectra of the HBLs are inconsistent with the predictions of the current theoretical models that have had success in describing simultaneous X-ray/TeV observations, and suggest additional components in the GeV band, as well as complex time variability. Current theoretical pictures explain the GeV emission as comptonization of the synchrotron photons in the jet, and predict hard spectra that should join smoothly with the TeV emission. The current analysis shows that the situation is more complex. The spectrum ranges from hard to soft during individual epochs, and the Mrk 421 SED shows a convex break in the aggregated data. The mission averaged EGRET spectrum for PKS 2155-304 also shows a similar (but not as pronounced) convex curvature. Simultaneous GLAST and X-ray observations of high X-ray states will address the issue of the convex curvature in the future. Such data will also explore the possibility of the steep EGRET emission originating from photons produced by electrons accelerated close to the limit of diffusive shock acceleration.

Tracking Spectral Changes in Blazars with the Energetic Gamma Ray Experiment Telescope (EGRET)

by

Giridhar Nandikotkur

Dissertation submitted to the Faculty of the Graduate School of the
University of Maryland, College Park in partial fulfillment
of the requirements for the degree of
Doctor of Philosophy
2007

Advisory Committee:
Professor Jordan Goodman, Chair/Advisor
Dr. Keith M. Jahoda, Co-Advisor
Dr. Robert C. Hartman
Dr. David J. Thompson
Professor Nicholas S. Chant
Professor Konstantina Trivisa

Dedication

To my wife Sangeeta, who showed me how to appreciate the brighter side of life

&

To my Parents, who have always stood by me.

Acknowledgments

I am immensely grateful to Dr. Keith Jahoda, my advisor at Goddard Space Flight Center, for helping me fulfill a cherished childhood dream of mine: conducting research at NASA. Government sanctions imposed against India by the US after the nuclear tests, and, the heightened security after September 11 required that I be escorted in every single day. The constant paperwork to get the permission approved as well as walking to the Goddard main gate even on the coldest of winter days reflect Dr. Jahoda's sincere efforts to bring this degree to a fitting conclusion. Hiding the kindest of hearts behind a stern professional demeanor, he has patiently supported me during the slow progress of my first (unusually large) project and has always been available to address any queries and concerns that I might have.

I would also like to express my gratitude to Professor Jordan Goodman for being a constant source of encouragement. His willingness to stand by me and his unconditional promise to offer me financial support if ever US government policies made it difficult for me to continue my Ph.D. at Goddard gave me the confidence to pursue my education fearlessly. I was readily welcomed in the MILAGRO group office during the years when I was not allowed entry into Goddard.

Uncountable email exchanges, a door that was always open, a huge repertoire of knowledge, an assured sense of balance while interpreting results, the rigor of analysis, a kind nature: these are some things that come to mind when I think of Dr. Robert Hartman, with whom I have worked closely on all three projects of my dissertation.

My interactions with Dr. David Thompson during the extended time that I spent on my first project assured me that it was a task worth pursuing. He was always interested in and willing to help me at every stage of the analysis. I also thank Dr. Jean Swank for taking an interest in my research and offering me the financial assistance to pursue my dreams at NASA.

I am deeply indebted to Professor Nicholas Chant for having faith in my abilities and for considering me worthy of the Leon Herreid Fellowship for two consecutive years. During his tenure as the Graduate Director, I was always been welcomed in his office whenever I wanted advice. I especially appreciate his blocking his schedule for two whole months to accommodate my defense date.

I cannot find enough words to thank Professor Reshmi Mukherjee (Barnard College, Columbia University) who has supported and encouraged me over the years. She continues to be a constant source of inspiration to me (and my sociologist wife Sangeeta Parashar, who points out ever so often that the physical sciences tends to be very male-dominated)!

Professor Markus Böttcher (Ohio University at Athens) and Professor Markos Georganopoulos (University of Maryland, Baltimore County) stimulated my interest in theory and helped me see the "bigger picture". I am grateful to them for taking time out from their busy schedules, sometimes at a very short notice, to go over drafts.

Much thanks to Professor Konstantina Trivisa, whose class I would always look forward to, not just because of the content, but also to draw inspiration from her unwavering enthusiasm.

I thank Professor Sagdeev, Professor Papadopoulos, and Dr. Surja Sharma for providing me a place to work and simulating my interest in Plasma Physics. Thanks to David Friedlander and the entire system team at GSFC for their computing support.

Jane Hessing, a super caring person, who has always looked after my interest and gone out of her way to help me in administrative matters. I have thoroughly enjoyed several conversations about global cuisines with Bernie, who also provided me useful words of wisdom about life as well as opportunities to teach in the department.

Thanks to my family: Amma, Anna, Aruna, Vijayakumar, Swetha, Chintu, Ravi, Sailaja, Geetha, Uttam, and Achal for always standing by me and making my trips to India and San Francisco truly memorable. My nieces, Sahiti and Shravanti, have made me realize that human intelligence has an exponential growth.

The many conversations with Venu ("Professor" Venugopal Vuruputur, IISc, Bangalore) regarding India's performance in cricket, Terp basketball and NBA will be cherished. "K" (Srinivas Kotamraju) and "NR" (Sanjeev Nimishakavi) have always supported my "galactic" dreams because they understood my thirst for knowledge and the unknown.

My stay in Maryland has truly been memorable because of my friends and family. What kept me going? Among other things: Mummy & Papa's fun visits, Neeraj and Monica's many words of encouragement, Divya & Narayan's trips that were usually a surprise to Sangeeta only (thanks to my collusion with them), and of course the unabashed enthusiasm with which Tanmay and Megha eagerly, and

annually, enjoyed their dosas-and-movies vacations with us.

Satwant Kaur's resilience and positive energy, even in the face of vicissitudes, is truly inspiring. Anand Poojary, Sharmila, Murali, Uncle, Aunty and Lavanya made the occasional weekend extremely enjoyable and provided much needed nourishment to a hungry graduate student's palate. Matthew Cornick's enthusiasm for Physics and life, Namrata Uppal's passion for justice ("insaaf"), Ritvik Sahajpal's endless and bottomless cups of wit and chai, and our numerous sessions of 29 made the last year fly by a bit too fast.

This dissertation would not have been possible without my dearest wife, Sangeeta. During the course of my academic career, she inspired me to enjoy the smallest things in life and to see its brighter side. I thus finish my Ph.D. with the same level of enthusiasm that I started it with.

Table of Contents

List of Tables ix

List of Figures x

1 Introduction 1
1.1 Blazars as a Class of Active Galactic Nuclei . . . 1
1.2 Structure . . . 2
1.2.1 Black Hole and Accretion Disk . . . 3
1.2.2 BLR and NLR . . . 4
1.2.3 Torus . . . 4
1.2.4 Relativistic Jet . . . 5
1.3 Broadband Continuum emission . . . 6
1.4 Physical mechanisms underlying Blazar emission . . . 9
1.4.1 Leptonic Models . . . 10
1.4.2 Hadronic Models . . . 11
1.5 Motivation for the Thesis and its Organization . . . 12

2 Detectors and Data Analysis 15
2.1 EGRET Analysis . . . 15
2.1.1 Instrument Description . . . 16
2.1.2 EGRET characteristics . . . 19
2.1.3 EGRET analysis procedure . . . 19
2.1.3.1 Data Products . . . 19
2.1.3.2 Likelihood Analysis . . . 22
2.1.3.3 Efficiency Degradation and Recalibration . . . 24
2.2 RXTE Analysis . . . 26
2.2.1 Proportional Collimator Array(PCA) . . . 26
2.2.1.1 Analysis Procedure . . . 29
2.2.2 HEXTE . . . 35

3 Does the Blazar Gamma-ray Spectrum Harden with Increasing Flux? - Analysis of Nine Years of EGRET Data 40
3.1 Introduction . . . 40
3.2 Source Selection and Observations . . . 43
3.3 Analysis . . . 46
3.4 Results . . . 50
3.4.1 Gamma-ray spectral distribution . . . 50
3.4.2 Spectral variability with Flux . . . 66
3.4.2.1 Long term spectral variability . . . 66
3.4.2.2 Short term spectral variability: *Spectral hysteresis during a flare* . . . 73
3.5 Discussion . . . 76
3.5.1 Spectral variability in FSRQs and LBLs . . . 76

3.5.2 Spectral variability in HBLs- a possible external component? . 79
3.5.3 Blazars as a source of extragalactic gamma-ray background . . 81
3.6 Conclusions 83

4 An Intriguing Convex Break in the EGRET SED of Mrk 421 86
4.1 Introduction 86
4.2 Analysis and Results 87
4.2.1 The Multiwavelength Picture 92
4.3 Discussion and Conclusions 93

5 Intricacies in the EGRET SED of Blazars 100
5.1 Introduction 100
5.2 Analysis 103
5.3 Results and Discussion 104
5.3.1 3C279 105
5.3.2 PKS 1622-297 109
5.3.3 PKS 1406-076 109
5.3.4 PKS 0528+134 109
5.3.5 MeV Blazars 113

6 Future Research and Conclusion 134
6.1 Gamma Ray Large Area Space Telescope 134
6.2 What can we do with GLAST? 135
6.2.1 Short Term Spectral Variability 137
6.2.2 Long Term Spectral Variability 140
6.2.2.1 Overall Trend? 140
6.2.2.2 Spectral softening with Flux? 140
6.2.2.3 Is it a Power Law? 141
6.2.3 Spectral Variability in HBLs 143

Bibliography 146

List of Tables

2.1 The EGRET high level data products 22

3.1 Details of Viewing Periods(after Cycle 4) 44

3.2 EGRET Spectral Analysis Results 52

3.3 Spectral Analysis Results for well-observed Blazars. 57

3.4 Spectral Variability and Chi Squared Results 64

4.1 Details of HBL observations by EGRET. 88

List of Figures

1.1 Blazar Structure 2

1.2 Artist's conception of the image of a black hole 3

1.3 Images of AGN jets at different wavelengths 5

1.4 Phenomenological blazar SEDs 8

1.5 Different components of blazar emission 10

2.1 CGRO 15

2.2 Schematic view of EGRET 17

2.3 EGRET Point Spread function 20

2.4 Counts map for Viewing period 511.5 21

2.5 Sample EGRET spectra 25

2.6 Comparison of results from old and new maps. 27

2.7 The Rossi X-ray Timing Explorer 28

2.8 Schematic View of the Proportional Counter Array 29

2.9 Effective area of top layer of PCU 2. 30

2.10 The South Atlantic Anomaly 32

2.11 Filter file columns 33

2.12 Sample 34

2.13 HEXTE instrument aboard RXTE 36

2.14 Sample spectra from HEXTE 37

2.15 Fit parameters to simultaneous PCA HEXTE Data 38

2.16 Combined SED for PCA and HEXTE 39

3.1 EGRET spectrum of PKS 1622-297 and 3C 279 47

3.2 Spectral index Vs. Log(Synchrotron Peak Frequency) 51
3.3 EGRET photon spectral index Vs. gamma-ray flux > 100 MeV . . . 67
3.4 *Spectral index Vs Flux Continued* 69
3.5 *Spectral index Vs Flux Continued* 70
3.6 *Spectral index Vs Flux Continued* 72
3.7 *Spectral index Vs Flux Continued* 73
3.8 Spectral hysteresis in gamma ray data 75
3.9 Extragalactic Gamma-ray background 82

4.1 Mrk 421 EGRET light curve. 89
4.2 Chi-squared confidence contours showing the difference between states. 91
4.3 Convex break in Mrk 421 91
4.4 EGRET mission light curve for PKS 2155-304 and broadband spectra 94
4.5 Multiwavelength SED for Mrk421 95
4.6 Multiwavelength SED for PKS 2155-304. 96

5.1 Multi-epoch νF_ν spectra for 3C 279 107
5.2 Multi-epoch νF_ν spectra for 3C 279 108
5.3 Multi-epoch νF_ν spectra for PKS 1622-297 during the giant flare in 1997. 110
5.4 Multi-epoch νF_ν spectra for other states of PKS 1622-297 111
5.5 Multi-epoch νF_ν spectra for PKS 1406-076 during 4 consecutive viewing periods 112
5.6 Other Spectra for PKS 1406-076 112
5.7 PKS νF_ν spectra for PKS 0528+134 during a flare 114
5.8 Multi-epoch νF_ν spectra for PKS 0528+134 115
5.9 Mission Average spectrum for PKS 0528+134 116

5.10 Multi-epoch νF_ν spectra for PKS 0208-512 117
5.11 Mission average spectrum for PKS 0208-512 118
5.12 Multi-epoch νF_ν spectra for 3C 273 119
5.13 Mission Average νF_ν spectrum for 3C 273 120
5.14 Multi-epoch νF_ν spectra for PKS 1156+295 120
5.15 Multi-epoch νF_ν spectra for S 0716+714 121
5.16 EGRET SED for 0219+428 (3C 66A) 122
5.17 EGRET SED for 0430+2859 123
5.18 EGRET SED for 0827+243 (OJ 248) 124
5.19 EGRET SED for 0917+449 125
5.20 EGRET SED for 0954+556 126
5.21 EGRET SED for 1222+216 127
5.22 EGRET SED for 1219+285 128
5.23 EGRET SED for 1730-130 129
5.24 EGRET SED for 1830-210 130
5.25 EGRET SED for PKS 2230+114 131
5.26 Multi-epoch νF_ν spectra for QC 3C 454.3 132
5.27 EGRET SED for BL Lac 133

6.1 Schematic view of GLAST 136
6.2 Comparison between GLAST and EGRET 137
6.3 GLAST sensitivity to sources 137

Chapter 1

Introduction

1.1 Blazars as a Class of Active Galactic Nuclei

Active Galactic Nuclei (AGNs) have captured the imagination of astronomers at all wavelengths for more than 4 decades now. As the name suggests, the term refers to the nucleus of a galaxy, which is very often not clearly distinguishable from the host galaxy. However, the emission from the nucleus can rival or surpass (10^4 times) the combined emission from all the stars comprising the galaxy. These spectacular objects are the seat of some of the most energetic and violent physical phenomena, considering that such prodigious amounts of energy emanate from a tiny volume in space. It is widely believed that the nucleus consists of a super-massive black hole ($10^6 - 10^9$ times the mass of sun), and the power of the AGN comes from accretion onto the black hole. The matter spirals inward due to the gravitational attraction from the black hole, and plasma, consisting of possibly leptons and hadrons is ejected at relativistic speeds perpendicular to the plane of rotation, in the form of two narrow collimated jets that get wider as they propagate. Blazars is a term for AGNs that are viewed along the axis of the jet.

1.2 Structure

Figure 1.1, taken from [1], shows a cartoon view of the blazar nucleus and the presumed essential components.

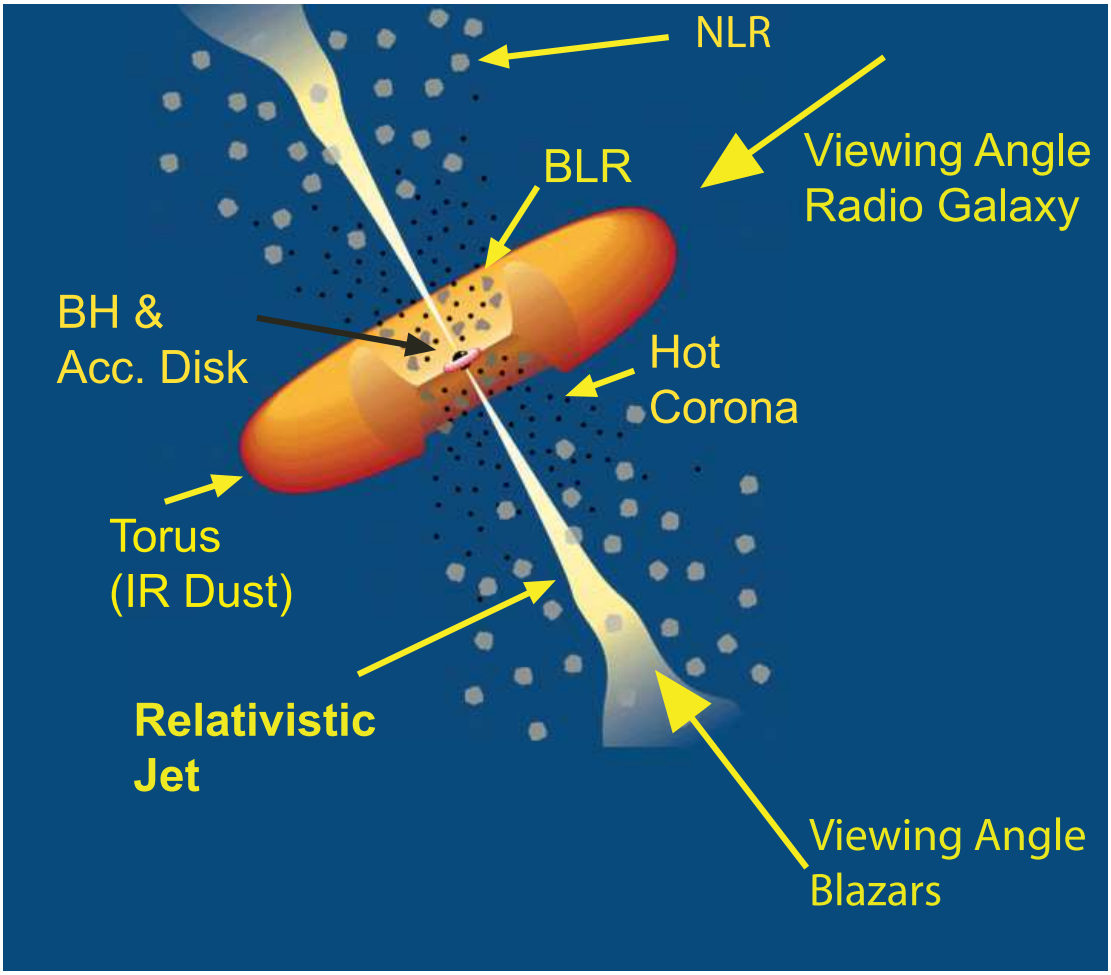

Figure 1.1: Structure of a blazar. Figure adapted from Urry and Padovani (1995) [1]. Black hole and accretion disk are at the center, surrounded by a dusty torus that emits predominantly in the infrared. The jet is ejected in two directions perpendicular to the plane of the galaxy. Jet encounters a Broad Line Region (BLR) of clouds and then the Narrow Line Region (NLR). If the observer is viewing along the axis of a jet, then the source is called a blazar. The AGN is viewed is side on in case of a radio galaxy

1.2.1 Black Hole and Accretion Disk

The nucleus of an AGN has never been resolved before to be able to conclusively show an existence of a black hole. One of the future missions in NASA's *"Beyond Einstein Program"* will consist of the " Black Hole Imager" that will be able to, for the first time, get an image of the black hole as a dark spot whose boundary will be the event horizon. However, until such time, the energy budget arguments on radiation from AGNs point towards the existence of a super massive black hole at the center of the AGN whose mass is in excess of 10^8 solar masses.

Surrounding the black hole is an accretion disk whose structure might depend on a variety of parameters such as the magnetic field strength, viscosity of the accreting material, central mass of the black hole, to name a few. There is an alternative scenario [2] in which the core could consist of young stars in a extremely compact cluster. But if this cluster is not too large, it might evolve into a super massive black hole, through a series of steps that involves an intermediate stage of neutron stars or a black hole cluster.

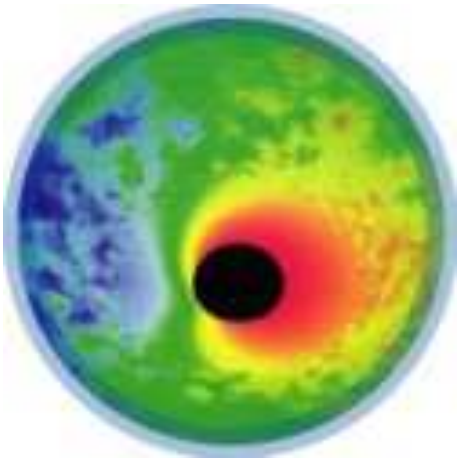

Figure 1.2: Artist's conception of the image of a black hole as expected to be captured, for the first time by NASA's Black Hole imager. The dark spot at the center is the *black hole*, with the boundary being the event horizon.

1.2.2 BLR and NLR

The broad line region (BLR) and narrow line region (NLR), are sparsely populated clouds of hot gases and dust that surround the black hole. Although not observed directly, the evidence for existence of these regions comes from the detection of broad and narrow emission lines in the optical and ultraviolet spectra, whose line widths aid in estimating the black hole mass. The width of the broad lines vary significantly. The Doppler shift in the line profiles provide clues to the bulk motion of the BLR and NLR regions, and can be connected to the black hole mass. The question of how these clouds stay confined in the region is still open, since the individual size is too small for gravity to hold the mass together. Assuming that each cloud is related to a giant star also leads to an overestimation of the mass of the BLR region.

1.2.3 Torus

The broad line region is obscured from the transverse line of sight by a torus that is possibly axially symmetric and contains clouds of dust. While it has not been imaged so far, the theoretical models of infrared emission from circumnuclear dust match the observed spectra reasonably well. Some of the models assume the torus to contain a distribution of granular dust [3] of varying sizes. The tori have also been considered as a uniform distribution of clouds of dust [4].

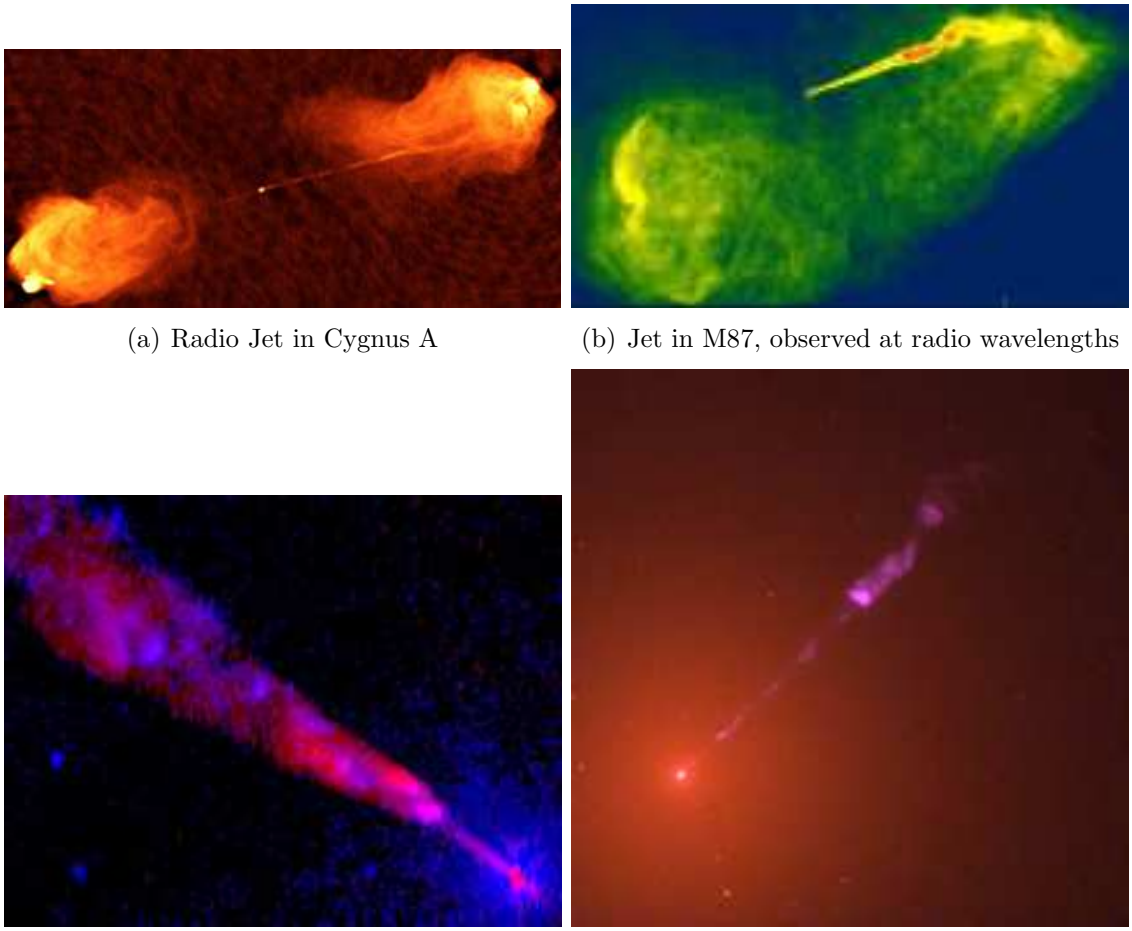

(a) Radio Jet in Cygnus A

(b) Jet in M87, observed at radio wavelengths

(c) Centaurus A -jet observed in X-rays by the Chandra ACIS instrument

(d) M87 jet at the optical wavelengths

Figure 1.3: Images of AGN jets at different wavelengths

1.2.4 Relativistic Jet

A portion of The accreting mass is somehow ejected in the form of jets probably along the black hole rotation axis. The jets start very narrow near the black hole and expand as they move forward, and have been observed in the radio, optical and X-ray images of AGNs. However, the complete extent of the jets is revealed in radio images of galaxies which are viewed along the plane of rotation of the galaxy. Figure 1.3 shows two radio images, an optical and an X-ray image of jets seen in AGNs. The jet in some cases could be one-sided.

The apparent speeds of some of the ejecta exceed the speed of light, suggesting that the material in the jet approaches relativistic speeds [5, 6]. But it is still not very clear how the jets, which draw the power from the accretion, are formed in the first place. The only successful solution proposed to date has been the *Blandford and Znajek* mechanism [7], through which electron positron plasma can be created through cascade production near the vicinity of a black hole. Theoretical efforts that model blazar emission start from this point by injecting a relativistic blob of charged plasma at some distance above the plane of the accretion disk. The plasma subsequently radiates via synchrotron and inverse-Compton mechanisms to produce the observed spectrum.

1.3 Broadband Continuum emission

One of the striking features of blazars (AGNs in general) is their emission of radiation over an extraordinarily broad range of frequencies suggesting a non-thermal origin for the underlying physical mechanisms. Thermal emission, such as from stars or the accretion disk, can be essentially modeled by blackbody radiation and cannot span more than 4-5 orders of magnitude in frequencies.

The broadband spectral energy distribution (SED) is a plot of the energy flux per waveband (νF_ν) Vs. the frequency ν (Hz), usually plotted on a log scale to account for the broad range of frequencies and flux. νF_ν is a useful quantity to compare energy emissions in different wavebands, and is in units of ergs cm^{-2} s^{-1} or Jy-Hz (1 Jy-Hz=10^{-23} ergs cm^{-2} s^{-1}). F_ν is the specific flux detected at frequency

ν, and is in ergs cm^{-2} s^{-1} hz^{-1}.

Prior to 1991, the spectrum was sampled, in the increasing order of frequencies, in radio, optical, ultraviolet and X-rays. The launch of the Compton Gamma Ray Observatory (CGRO) heralded a new era in blazar research. The Energetic Gamma Ray Experiment Telescope (EGRET) (30 MeV - 10 GeV), one of the four instruments aboard CGRO, detected gamma-ray emission from blazars [8] (67 confirmed detections over a 9 year period from 1991-2000), thus extending the SED to the gamma-ray region. A majority of them were flat spectrum radio quasars, while the rest of them were BL Lac objects.

The detection of Mrk 421 at TeV energies by the WHIPPLE Cerenkov telescope [9] pushed the spectrum to even higher frequencies. Although Mrk 421 was a strong TeV gamma-ray emitter, it did not radiate as strongly in the GeV (EGRET) region. EGRET however did detect Mrk 421. In 1996, Mrk 501 was detected by WHIPPLE [10] and became the second blazar to be detected at TeV energies, but again not producing a strong detection at GeV energies. The only time EGRET saw Mrk 501 was during a campaign in 1996, when the source was weakly detected, at a significance of 3.5σ. These two blazars hinted at a possible inherent dichotomy in the nature of gamma-ray emission in blazars. Similar classification could also be seen at lower frequencies where the TeV blazars were bright in X-rays and weak at radio wavelengths. In contrast, the radio-loud FSRQs were faint at X-ray frequencies. Observationally, the class of blazars includes both flat-spectrum radio quasars (FSRQ) and BL Lac objects. FSRQs have strong and broad optical emission lines while the lines are weak in BL Lac objects. A large-sample study conducted by

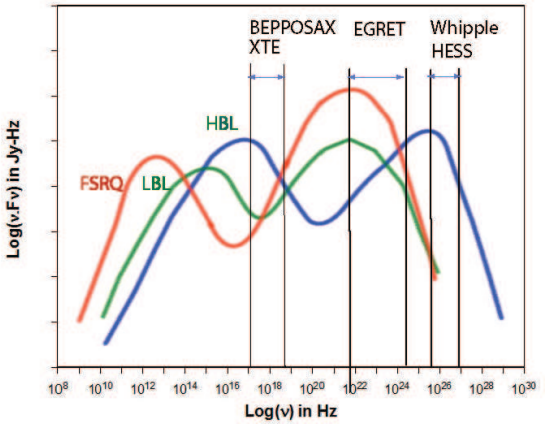

(a) Flux Vs. frequency νF_ν

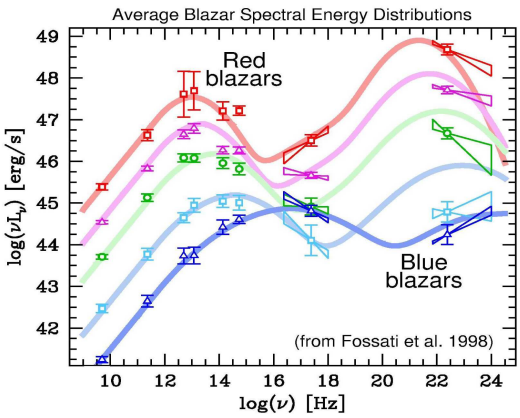

(b) Luminosity Vs. frequency νL_ν. Taken from Fossati *et al.* (1998) [12]

Figure 1.4: Phenomenological broadband spectral energy distribution (SED) of blazars

Giommi and Padovani (1994) [11], Sambruna, Maraschi & Urry (1996) [13], Fossati *et al.* (1998) [12] pointed to a continuity in the observed spectral properties of blazars.

The SEDs of blazars show two peaks. The spectral-peak position allows a further division of BL Lac objects into two categories: low-frequency-peaked BL Lac objects (LBLs) and high-frequency peaked BL Lac objects (HBLs). The first peak is at infra-red/optical frequencies for *red blazars* which could be either FSRQs or LBLs and at UV/X-rays for *blue blazars* (HBLs). The second peak is in the gamma-ray range (MeV-GeV) for LBLs/FSRQs and the TeV range for HBLs. Figure 1.4-(a) shows the empirical νF_ν plot for blazars. FSRQs are typically high redshift sources and have a higher intrinsic luminosity than the BL Lac objects. The BL Lac objects also show a difference with LBLs having higher luminosity than HBLs. This difference in redshifts separates the SEDs further when luminosity (L_ν) is used instead of flux (F_ν). The luminosity, $4\pi r^2 F_\nu$, is calculated assuming an isotropic distribution

of flux. This is not true of blazars, as the radiation is beamed at gamma-ray wavelengths, but the use of the same prescription for all blazars still allows a comparison to be made. The νL_ν SED plot, shown in Figure 1.4-(b) is taken from [12]. The color coding in these plots is according to the peak-frequency position. HBLs, that have their peaks at higher frequencies are coded in blue. Consequently they are somtimes referred to as *blue* blazars. Also shown in figure 1.4-(a) is the frequency coverage by some of the instruments.

1.4 Physical mechanisms underlying Blazar emission

The jet consists of blobs of plasma moving at relativistic speeds. Theoretical efforts that model the emission throughout the electromagnetic spectrum fall into two broad categories, on the basis of their assumption about the content of the radiating plasma. The leptonic models assume that the emission is from ultrarelativistic electrons and/or electrons or positrons, whereas the hadronic models assume the emission to arise out of hadrons (protons and secondary muons, electrons, positrons, and mesons). The particles are assumed to have a power law distribution in Lorentz factors as given by the expression $N(\gamma) = Const.\gamma^{-s}$, $\gamma_1 < \gamma < \gamma_2$, where γ_1 & γ_2 are the lower and upper limits of the Lorentz factor of the particles. The assumption of a power law distribution is made in order to fit the observations that show a power law dependence in flux. The observed number distribution of photons can be modeled as $N(E) = Const.E^{-\alpha}$. The flux then has a dependence of $F(E) = Const.E^{-\alpha+1}$

1.4.1 Leptonic Models

It has been widely accepted, in the scenario of leptonic models, that the lower-frequency peak is due to synchrotron emission from relativistic plasma moving along the jet away from the core of the AGN while the second peak is attributed to inverse-Compton scattering of relativistic electrons and/or electron-positron pairs by soft ambient photons, produced either internal or external to the jet. These "seed-photons" for inverse-Compton emission could come from synchrotron emission itself as postulated by synchrotron-self Compton (SSC) models [14, 15, 16, 17]. The SSC models have been successful in fitting simultaneous X-ray and TeV data from HBLs.

The source of the soft photons could also be external to the jet under the broad class of external Compton (EC) models. The photons could be entering the jet either directly from the accretion disk as in the ECD (external Compton scattering of direct disk radiation) models [18, 19], or they could reach the jet after being re-scattered by surrounding broad-line-

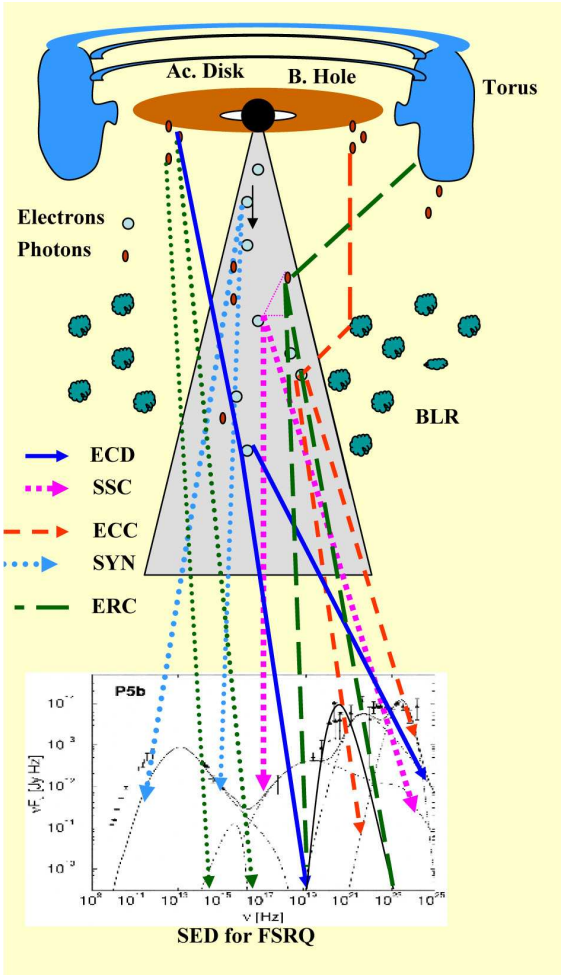

(a)

Figure 1.5: Different components to electromagnetic emission from blazars.

region (BLR) clouds as in the ECC (external Compton scattering from clouds) models [20, 21, 22]. In addition, the BLR could also reflect the synchrotron photons back into the jet to undergo inverse-Compton scattering (External-Reflection-Compton model; [23]). Finally, the seed photons could be produced by the infrared (IR) dust that surrounds the blazar nucleus (External Compton from infrared dust-ERC(IR); [24, 25]). The dust is concentrated in a torus that lies in the equatorial plane of the blazar [26]. Figure 1.5 shows a schematic view of the different components to blazar emission. The plot at the bottom of the figure shows the relative position of each component in frequency space.

Similar to a continuity in observational properties, an intrinsic difference is also manifested in the physical properties (Ghisellini *et al.* 1998 [27]). The extent of contribution from external fields is decreases from FSRQs to LBLs to HBLs. As a result of this, BL Lac objects (HBLs or LBLs) do not show prominent emission lines. HBLs have the lowest intrinsic power; FSRQs are the most powerful blazars. The intrinsic difference is also manifested in the relativistic beaming, with BL Lac objects having smaller Doppler factors than FSRQs.

1.4.2 Hadronic Models

The jet could consist of $e^{\pm}$, proton and muon plasma under the class of "hadronic models". A wide variety of secondary processes are possible in this scenario [28, 29]. The first peak is still from synchrotron radiation from primary and secondary electrons (produced by particle cascades [30]). However, the 2nd peak

is generated by synchrotron emission itself, unlike the leptonic models, where it is generated via inverse-Compton processes. The synchrotron emission could come from primary protons [31, 32], or from secondary muons and mesons [33, 32, 34, 30]. Several particle cascade processes are possible [35]. Electromagnetic cascades can be initiated by photons from π^0-decay (π^0 cascade), electrons from the $\pi^{\pm} \rightarrow \mu^{\pm} \rightarrow e^{\pm}$ ("$\pi^{\pm}$ Cascade"), p-synchrotron cascade, and $\mu^{\pm}$ cascade. These cascades differ in their predictions of the shape of the second broadband peak.

1.5 Motivation for the Thesis and its Organization

Multiwavelength fits using hadronic models have been fewer in the literature. In the context of leptonic models, very often a combination of inverse Compton models is required to fit the data near the second peak. Data from the same blazar requires differing contributions from the various EC models based on whether the blazar was undergoing a flare or not.

On the observational front, the gamma-ray spectral indices are supposed to show a smooth transition from FSRQs to LBLs to HBLs. Since the the flux shows a power law dependence ($F(E) = Const.E^{-\alpha+1}$), a νF_{ν} or equivalently an E^*F_E plot will have a $E^{-\alpha+2}$ dependence. Consequently, spectral indices of 2 will appear as a horizontal line on the SED plot. The EGRET energy range lies on the decreasing portion of the inverse-Compton peak for FSRQs. As a result, the spectral indices would be steeper than 2. The HBLs are the other extreme, as the EGRET energy range falls on the rising portion of the inverse-Compton peak. As result their spec-

tral indices are supposed to be less than 2. LBLs have indices somewhere in between. This simplified picture does not take the spectral variations into account. FSRQs are known to show a large variability in the gamma-ray region. The only previous study presenting gamma-ray spectral indices for blazars from multiple epochs is by Mukherjee *et al.* (1997) [36], which presents data only until end of 1995 (EGRET was functional till 2000). The largest collection of broadband data for blazars was by Von Montigny *et al.* (1995) [37], but it had one spectrum each for 33 blazars. Multi epoch νF_ν spectra for the entire mission have only been presented for 3C 279 (Hartman *et al.* 2001, [38]) and PKS 0528-512 (Mukherjee *et al.* 1999 [39]).

The EGRET is mission is complete. The wealth of results from the mission has ushered in a exciting period for blazar research. The launch of the next generation gamma-ray observatory, the Gamma Ray Large Area Telescope (GLAST) in February 2008 will be a leap forward into the future. But the complete EGRET archives still present a wonderful opportunity to conduct comprehensive studies that have never been done before. This thesis is a dedicated effort towards examining the spectral variability in blazars using the *entire* EGRET archives. It will be the largest spectral study ever conducted for blazars in the gamma-ray region and will also hopefully serve as a compendium of results for the upcoming GLAST mission.

I describe the EGRET instrument, its data, and the analysis methods used in Chapter 2. The RXTE analysis is discussed in Chapter 2.Chapter 3 presents a comprehensive and detailed spectral study of blazars. In the course of this study I observed an intriguing feature in the HBL spectra that could have exciting prospects for the GLAST mission. If confirmed, it will challenge out current understanding of

gamma-ray emission from HBLs. I used multiwavelength data from the literature and analyzed the X-ray data from the Rossi X-ray Timing Explorer (RXTE) for constructing the broadband SED. Chapter 4 presents the results of the HBL spectral variability study. In chapter 5, I present the multi-epoch νF_ν spectra for all the bright blazars, and, look for any intricacies in them. And finally, I conclude in Chapter 6 with how we can take this study forward with the upcoming GLAST mission.

I have conducted this research in collaboration with scientists from the Goddard Space Flight Center (GSFC), University of Maryland at Baltimore County, the Astrophysical Institute at Ohio University, Barnard College and Columbia University. Hence, I will refer to the first person in plural, in the rest of my thesis, to acknowledge this collaboration.

Chapter 2

Detectors and Data Analysis

2.1 EGRET Analysis

The Energetic Gamma Ray Experiment Telescope (EGRET) was one of the four detectors aboard the Compton Gamma Ray Observatory (CGRO), a satellite that was carried by the space shuttle Atlantis on April 5, 1991, and placed in a circular orbit of 450 Km altitude with an inclination angle of 28.5^o, and a period of approximately 90 minutes. Named after the Nobel Laureate, Dr. Arthur Holly Compton, the CGRO was the second (after the HUBBLE Space Telescope) of NASA's great observatories, providing an unprecedented coverage of the electromagnetic spectrum from 20 keV - 30 GeV. It contained four instruments: Burst And Transient Source Experiment (BATSE) operating at energies 20-600 keV, Oriented Scintillation Spectrometer Experiment (OSSE) that covered the energy range 50 keV - 100 MeV, the Compton Telescope (COMPTEL) with a 1-30 MeV coverage, and finally EGRET, which provided the highest gamma-ray window, 20 MeV- 30 GeV. EGRET began an all-sky survey on April 16, 1991, and stopped observing on March 28, 2000, a few weeks before CGRO was de orbited.

Figure 2.1: The Compton Gamma Ray Observatory

2.1.1 Instrument Description

EGRET was an imaging instrument that had a field of view of radius 30^o. Like its predecessors SAS-2 and COS-B, EGRET was a spark chamber telescope that detected high energy photons via the pair-creation process The instrument consisted of 4 main components as shown in Figure 2.2: A multilevel spark chamber, a triggering telescope, large Sodium Iodide (NaI) Total Absorption Shower Counter (TASC) and the Anti Coincidence Counter surrounding the spark chamber. The instrument description and the major scientific goals of the EGRET mission have been described in detail in the papers by Hughes et al. [40], Bertsch [41], Kniffen et al. [42], Kanbach et al. (1988 [43], 1989 [44]) and Hartman et al. [45]. The following sections briefly describe some of the important features of the EGRET instrument.

Pair Production

The detection of photons proceeds through the following steps. The incident gamma-ray enters the instrument without interacting in the anticoincidence counter and gets converted to an electron-positron $e^{\pm}$ pair (with a probability of about 35 % above 200 MeV) in the one of the tantalum (Ta) foils interleaved with 28 upper spark chamber modules. As this pair travels through the gas filled chambers, sparks are generated along the path, creating a trail of the pair in the process. The spark chamber is filled with a gas mixture of neon, argon, and ethane at 1.1 atmospheric pressure. Below the conversion chamber, a two-layer scintillator detector (separated by 60 cm), consisting of a 4 by 4 array of plastic scintillator tiles each, registers the passage of e^+e^- charged particles.

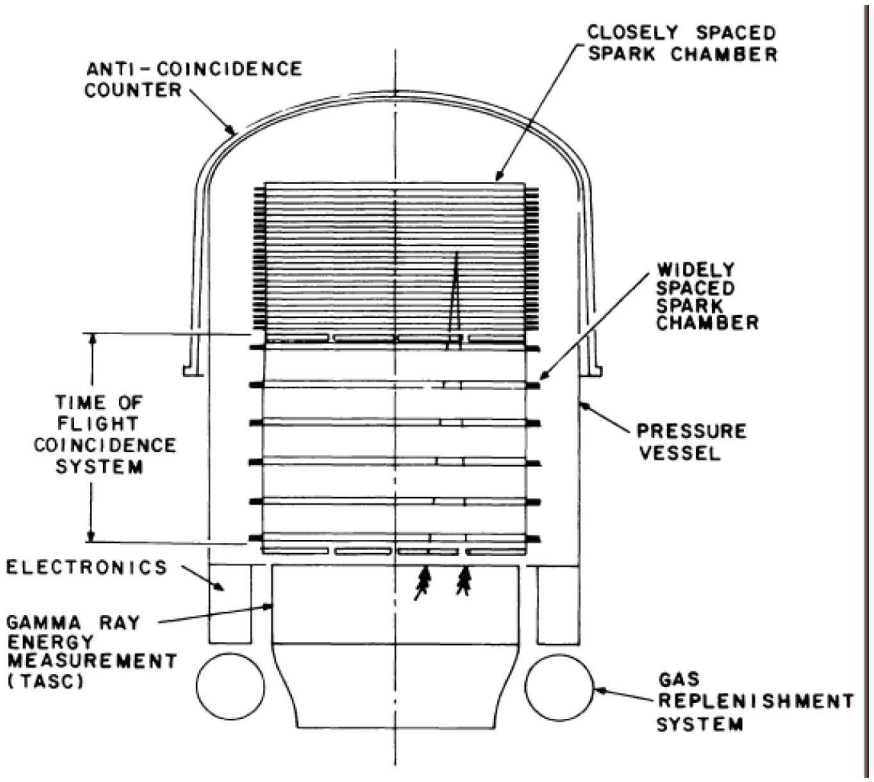

Figure 2.2: Schematic view of EGRET taken from

Direction Measurement

The direction of radiation is determined by the time of flight delayed coincidence method. If at least one particle of the pair is detected as a downward moving particle, and there is no signal in the large anti-coincidence dome, the track-imaging system is triggered. The electron-positron pair tracks are projected in two orthogonal views and the direction of the tracks are determined with respect to the detector axes in each view. The gamma-ray arrival direction is then estimated based on a weighted bisector of the angle between the two particle tracks.

TASC Energy Measurement and the Anti-coincidence Dome

One or both of particles ($e^{\pm}$) enters the Total Absorption Shower Counter (TASC), classified as class B and class A events respectively, and create(s) a particle shower

that is absorbed. The energy of the the incident gamma-ray is determined as a function of the energy deposited in TASC. This energy does not include the energy lost by the electron and positron before reaching the TASC, while traversing the Ta plates in the upper spark chamber, the steel scattering plates between the lower spark chambers, the plastic trigger scintillators, etc. Correction is made for the lost energy, which is proportional to the length of travel. An energy correction is also carried out for class B events (where one of the particles does not reach TASC) to account for the energy carried by the particle which missed the TASC. The energy resolution of the experiment is about 20% (Full Width Half Maximum) over the central part of the energy range. The resolution drops to about 25% in the GeV range due to incomplete absorption in the NaI calorimeter, and at energies below about 100 MeV where ionization losses in the spark chamber plates comprise an appreciable portion of the total energy.

The main purpose of the anti-coincidence dome is to veto events from background charged cosmic ray particles that are approximately 10^5 times more numerous than the gamma-rays. Sometimes the electromagnetic shower induced by a high energy gamma-ray (> 10 GeV) in the TASC causes some particles (mostly 100-1000 keV photons) to travel backward (termed *backsplash*) through the tracker to the anticoincidence dome and register a signal that causes the event to be misinterpreted as a charged cosmic ray particle. The event gets wrongly vetoed (termed as *self vetoing*). This problem was acute for EGRET at high energies and as a result the effective area dropped substantially beyond 10 GeV.

2.1.2 EGRET characteristics

EGRET had an effective area of 1000 cm^2 at 150 MeV, 1500 cm^2 between 500 MeV-1 GeV, decreasing gradually to about 700 cm^2 at 10 GeV. The off-axis sensitivity decreased as an approximate Gaussian with a full-width-half-maximum of $\sim 20^o$. The sensitivity beyond 30^o was less than 15% of the on-axis sensitivity.

The error in measuring the arrival direction of the incident photon is parametrized by the point spread function (PSF). The PSF is more compact at higher energies as shown in Figure 2.3 (Thompson *et. al.* 1993 [46]). An approximation to the angle which contains 68% of the events due to a point source is given by

$$\theta_{68} \leq 5.85^{\circ} \left(\frac{E_{\gamma}}{100MeV} \right)^{-0.534} \tag{2.1}$$

with E_{γ} in MeV.

2.1.3 EGRET analysis procedure

2.1.3.1 Data Products

Each EGRET observation, called a "Viewing Period", ranged from 3-20 days, but was typically a week in duration. Roughly one year's worth of observations were considered as one Cycle. There were nine Cycles of observations during the 9 year period. A region of sky was sometimes observed for two or more viewing periods consecutively either due to scheduling reasons, or if a source present in the field of view was undergoing a flare.

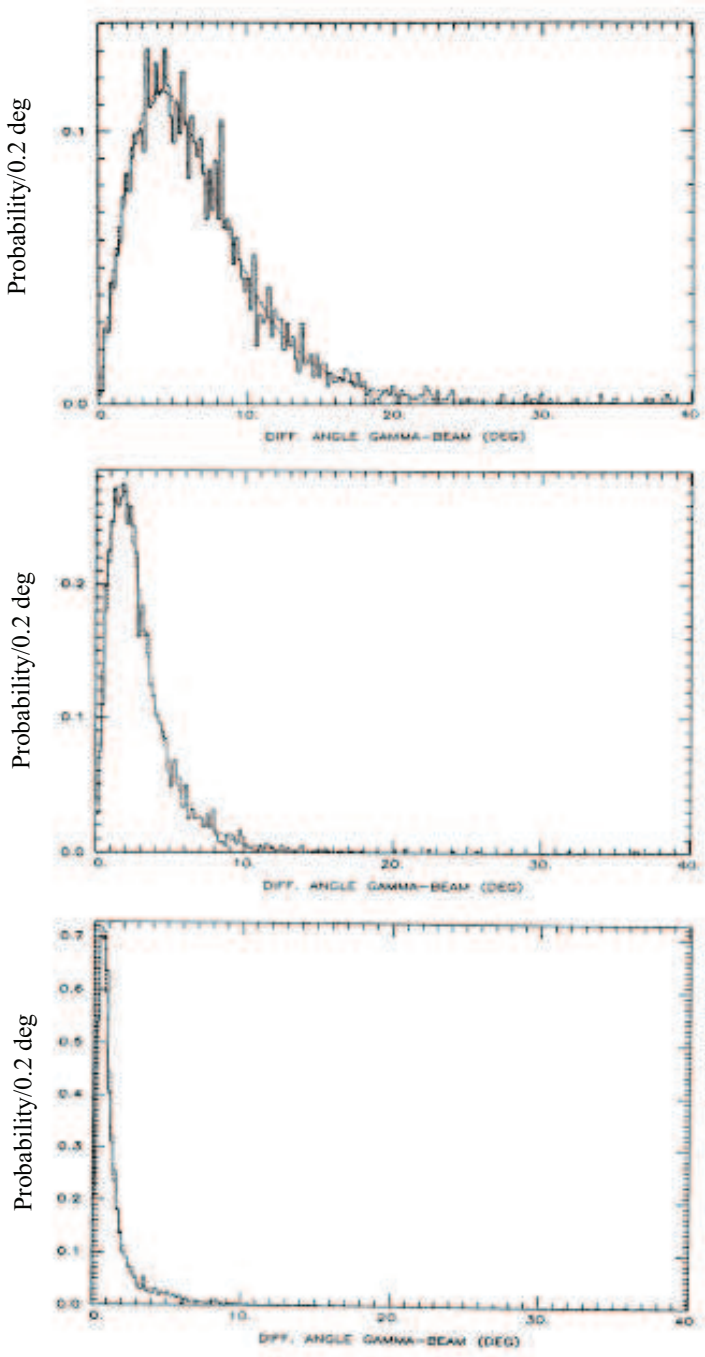

Figure 2.3: Energy dependence of the Point Spread Function (PSF) for EGRET, taken from Thompson *et al.* [46]. Starting from the top- PSF at 60 MeV, 200 MeV and 1000 MeV.

The standard products for EGRET data consist of count maps of regions of sky in $(1/2)^o \times (1/2)^o$ bins. Corresponding maps for the instrument exposure and

intensity (counts/exposure) are also available to start with. The maps are named *counts.vpXXXX.g00N*, where "XXXX" stands for the 4 digit viewing period that could range from 000.1 to 919.5. However, the viewing periods are referred to by their decimal equivalent which in cases above would be 0001 and 9195. Four different maps are available for each viewing period (represented by the value of 1-4 for "N"). Each map contains different energy intervals as listed in Table 2.1. Figure 2.4 shows a counts map for counts.vp5115.g002 for the range > 100 MeV.

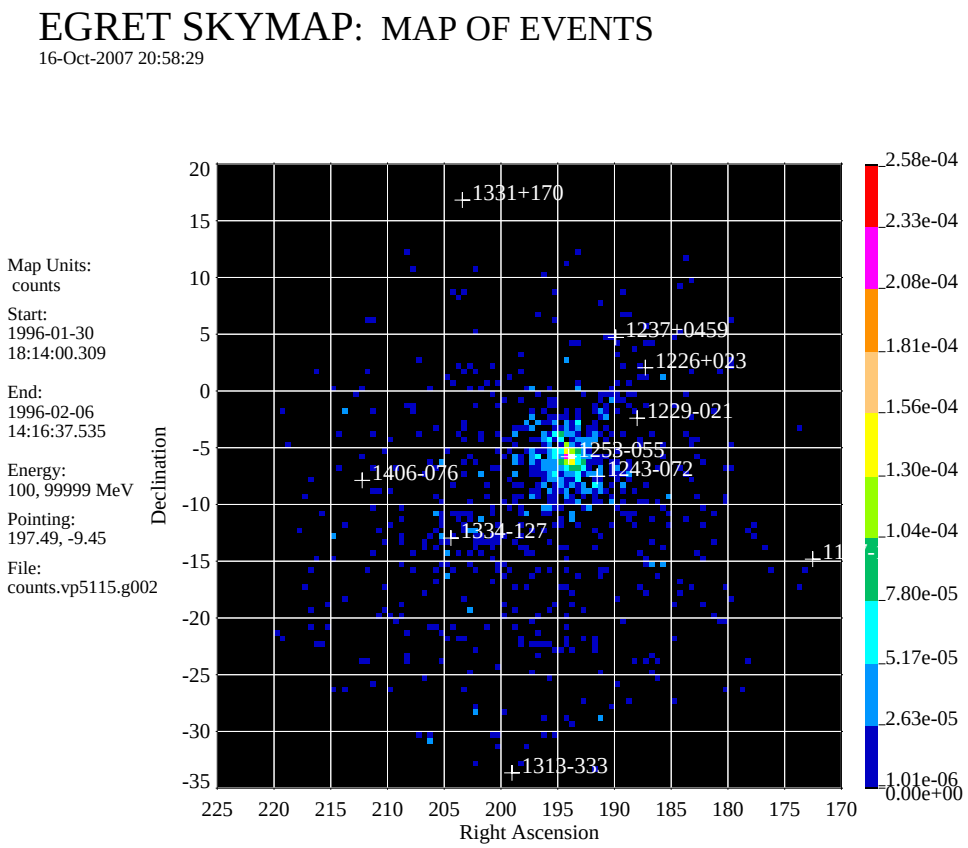

Figure 2.4: Counts map for the interval >100 MeV for Viewing period 511.5. The individual photons are seen in some pixels. Also shown are the different EGRET sources in the field of view.

Table 2.1: The EGRET high level data products

Map Extension	**Energy intervals in MeV**
counts.vpXXXX.g001	30-50, 50-70, 70-100, 100-150, 150-300, 300-500, 500-1000, 1000-2000, 2000-4000, 4000-10000
counts.vpXXXX.g002	30-100, 100-99999
counts.vpXXXX.g003	100-300, 300-99999
counts.vpXXXX.g004	300-1000, 1000-99999

2.1.3.2 Likelihood Analysis

The EGRET analysis program LIKE (Mattox *et al.* (1996)[47])uses the method of maximum likelihood to simultaneously determine the counts from all the sources in the field of view as an excess above the predicted diffuse gamma-ray flux, taking the point spread function of the detector into account. The diffuse background model (Hunter *et al.*, 1997 [48]) consists of two components; a diffuse galactic flux and a constant diffuse extragalactic flux. Using this model, the predicted counts in each pixel are modeled according to

$$\theta_{ij} = g_m G_{ij} + g_b E_{ij} + \sum_k c_k PSF(l_k, b_k, i, j) \tag{2.2}$$

where g_m is Gmult, the galactic multiplier, and g_b is Gbias, the extragalactic isotropic diffuse flux and c_k is the number of counts detected from the source in question at the coordinates l_k and b_k. E_{ij} is the exposure at each pixel (i,j) and G_{ij} is expected counts due to the galactic diffuse emission which is taken from the model. LIKE makes a simultaneous determination of g_m, g_b and c_k The strength of the detection is calculated by comparing the likelihood of detection determined with and without the source included in the model. The likelihood is the product of the pixel probabilities within a user defined radius, and can be written as L_θ=$\prod_{ij}$ p_{ij}, where the

pixel Poisson probabilities are given by

$$p_{ij} = \frac{\theta_{ij}^{n_{ij}} e^{-\theta_{ij}}}{n_{ij}!} \tag{2.3}$$

The Logarithm of the likelihood reduces to

$$Ln(L) = \sum_{ij} n_{ij} ln(\theta_{ij}) - \sum_{ij} \theta_{ij} \tag{2.4}$$

where n_{ij} is the observed number of counts in each bin. The significance of detection of a source is the square root of the "test statistic" determined using

$$TS = -2(lnL_o - lnL_1) \tag{2.5}$$

where L_1 and L_o are the likelihood values from the analysis with and without the source included.

For any viewing period, the analysis was started with the $>$ 100 MeV interval of the .g002 map. This subinterval of the map was used in conjunction with a list of all the EGRET sources (428 of them), and the counts and the significance of detection for all of them were found using the method mentioned above. All sources that were detected at a significance $<$ 2σ in the energy interval $>$100 MeV were eliminated from the list and the process was repeated again to determine the counts and fluxes (along with the associated errors) for the remaining sources. If the source of interest was detected at a significance > 4 σ in the energy interval $>$ 100 MeV, a four point spectrum was computed using counts recorded in the energy intervals

30-100, 100-300, 300-1000 & $>$ 1000 MeV. The points were fitted with a single power law of the form $F(E) = k(E/E_o)^{-\alpha}$ photons cm^{-2} s^{-1} MeV^{-1} where $F(E)$ is the flux, α the photon spectral index, E the photon energy, E_o the energy normalization factor and k a coefficient of normalization.

If the overall significance of detection of the source was greater than 6 σ, the energy intervals with a strong detection were further split up into smaller intervals (for which standard EGRET maps exist) to determine the spectral index. For the strongest sources, the standard 10 intervals 30-50, 50-70, 70-100, 100-150, 150-300, 300-500, 500-1000, 1000-2000, 2000-4000, 4000-10000 (all in MeV) were utilized. Most of the spectra after Cycle 5 had to be determined using 4-5 energy intervals (when a source was not undergoing a flare). Some sample spectra are shown in Figure 2.5.

2.1.3.3 Efficiency Degradation and Recalibration

The spark chamber gas deteriorated over time due to the break down of the organic component, ethane, which was used to suppress spurious sparking. EGRET had an on board gas replenishment system that could evacuate and refill the the spark chamber 5 times during the mission. The refills took place on 1991, December 2-3, the second one on 1992, December 3-4. The last complete gas fill was on Sept 9, 1995 with an additional partial refill on Dec 1, 1998. The efficiency of the detector dropped between these refills and did not completely recover with each succeeding refill. There was a failure of the spark chamber B readout in Nov. 1997, that also

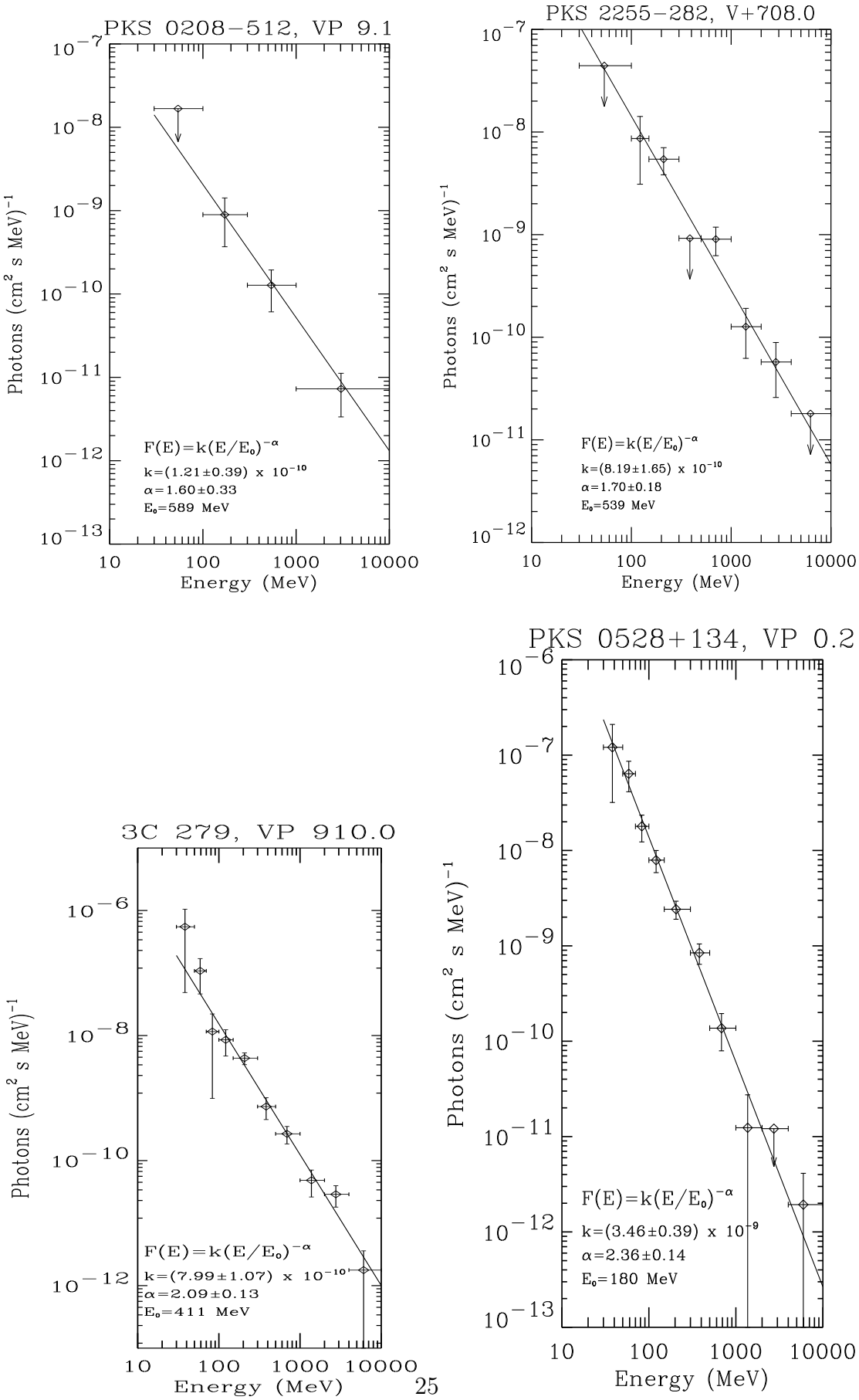

Figure 2.5: Sample EGRET spectra

affected the efficiency. EGRET's efficiency degradation was much more severe after the refill of 1995 and an energy dependent effect also was observed. The calibration method used to scale the efficiency factors (Esposito *et al.* (1999) [49] did not take this effect into account. A new method was developed (Bertsch et al. 2001 [51]) that included the energy dependence of the degradation. All the EGRET maps were regenerated after this recalibration. We analyzed all nine years of EGRET data for all the blazars using these new maps. Although the new method is more applicable for observations after Cycle 4, we found that the there were differences between our analysis and some of the previously published results for observations prior to Cycle 4. Some of these differences were notable. Mukherjee *et al.* (1996) reported a spectral hardening in PKS 0528+134 with increasing flux. A correlation of -0.85 between spectral index and flux using data from viewing periods 0.2-0.5 (combined), 1.0, and 213.0 was seen. The same combination of viewing periods using recalibrated data did not show any evidence of spectral hardening, as can be seen from Figure 2.6. Reanalysis of data from the giant flare in PKS 1622-297 (Mattox *et al.* 1997 [52]) also yielded different results for one of the four viewing periods.

2.2 RXTE Analysis

2.2.1 Proportional Collimator Array(PCA)

RXTE was launched on December 30, 1995 into low-Earth orbit at an altitude of 580 km corresponding to an orbital period of 90 min with an inclination of 23^o It contains three instruments on board, the Proportional Counter Array (PCA), the

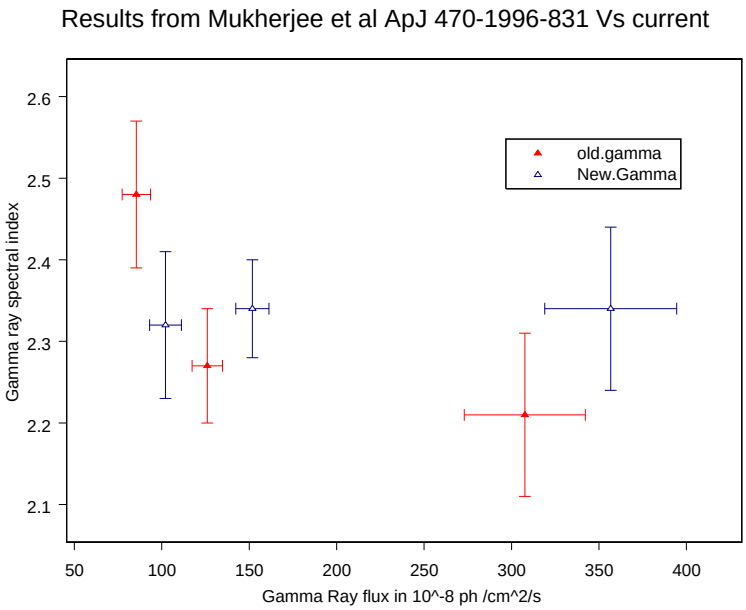

(a) PKS 0528+134: The new maps did not show any spectral hardening with increasing flux that was observed in Mukherjee *et al.* 1996[50]

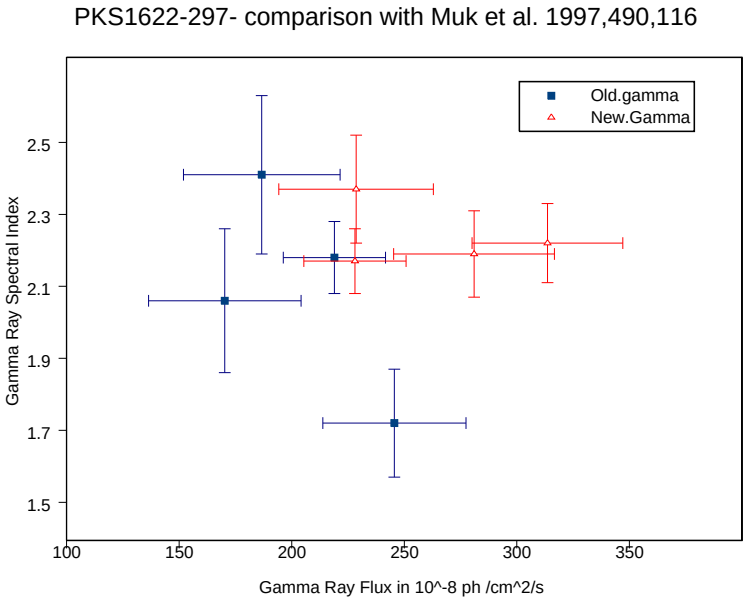

(b) PKS 1622-297: The spectral index value for VP 422.0 was substantially different.

Figure 2.6: Comparison of results from old and new maps.

High Energy X-Ray Timing Experiment (HEXTE) and the All Sky Monitor (ASM).

The PCA consists of five identical coalligned gas-filled proportional counter units (PCU) referred to by names PCU0 through PCU4. A schematic view of a PCU us shown in Figure 2.8. Each PCU is split into two volumes, the upper propane volume, the main xenon volume. Through these volumes run five layers of anode-wire grids: 1 propane veto layer, 3 Xenon layers, each split into two parts (left and right); 1 Xenon veto layer. The signal detection takes place in the three Xenon layers of which the top layer is the most sensitive since more X-ray events occur in the top layer (in detectors L1,R1) than in the bottom two (L2,R2,L3,R3). Anticoincidence techniques are used to veto events The instrument is sensitive in the energy range from 2-60 keV at a resolution of $< 18\%$ at 6keV and a total collective ares of 6500 cm^2. Details of the instrument, calibration and in flight performance can be found in Jahoda *et al.* 1996 [53] and Jahoda *et al* (2006) [54]. Each PCU is equipped with a collimator, and has approximately the same field of view with an FWHM of 1 degree. Unlike EGRET, which is an imaging instrument and can collect data from multiple sources at any instant of time, the PCA is a narrow field of view instrument.

Figure 2.7: The Rossi X-ray Timing Explorer (RXTE)

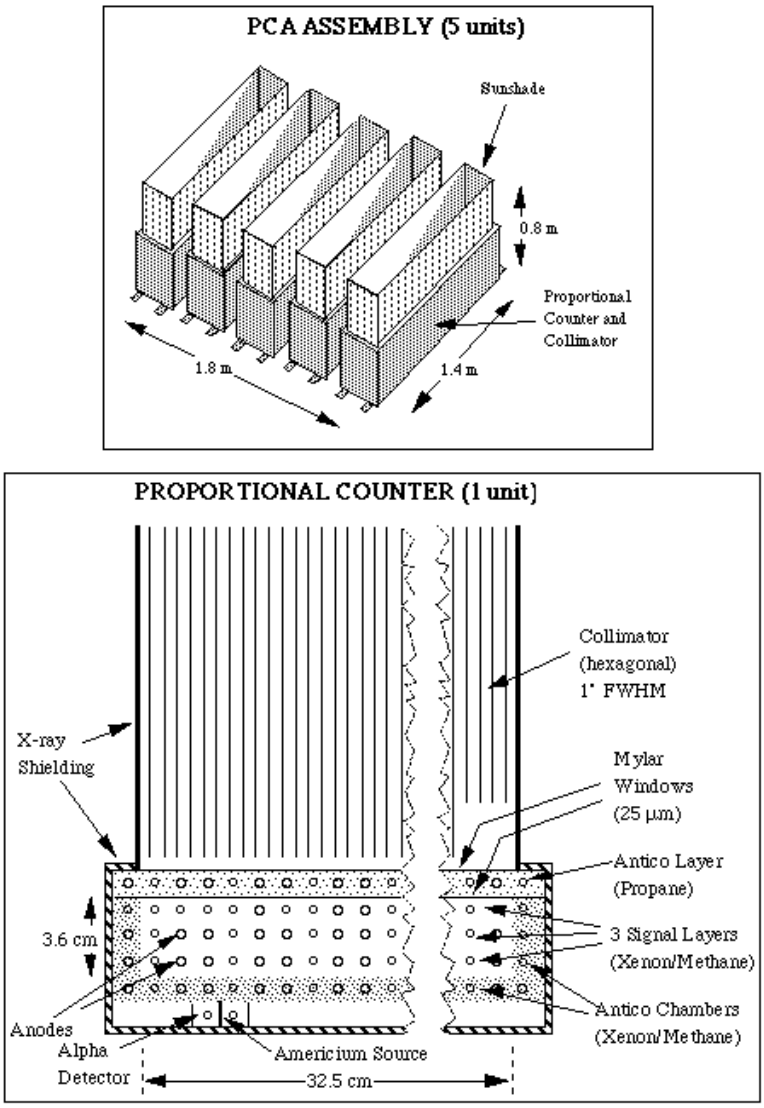

Figure 2.8: Schematic View of the Proportional Counter Array. Top figure: the five PCUs aligned with each other. Bottom Figure: Schematic view of a single PCU. The signal detection takes place in the three Xenon Layers. Figure taken from the heasarc website. http://heasarc.gsfc.nasa.gov

2.2.1.1 Analysis Procedure

The analysis procedure to get a spectrum and a light curve involves steps that clean the raw data through certain filter criteria that select the "good data". The raw data from each observation come binned in three different modes: generic

binned, standard 1 and standard 2. Standard 1 files contained data binned every 128 seconds, where as standard 2 files consist of 16 second bins and these were used for the current analysis. Although PCA has 5 PCUs, not all the PCUs were operational for the entire duration of the mission. PCUs 4 and 5 have been regularly rested to avoid breakdowns. PCU0 lost pressure in its propane layer, which plays a role in vetoing events, in May 2000. As a result of this, the the background rate was substantially higher for observations after that date. For the time frame relevant to our analysis, PCU 2 was "ON" the whole time. We used data just from the top layer of PCU 2 in order to standardize the analysis. The effective area (shown in Figure 2.9) is about 350 cm^2 at 3 keV, increasing gradually to a maximum of ∼1200 cm^2 at ∼7 keV and decreasing gradually to a value of ∼250 cm^2 at 20.0 keV

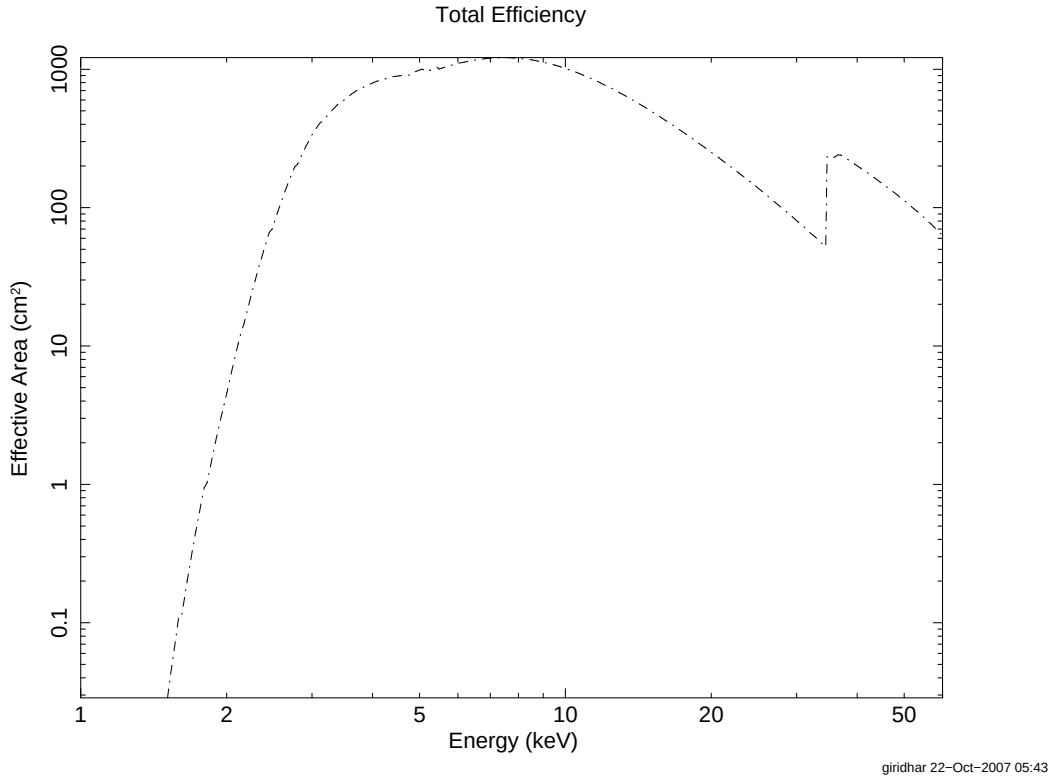

Figure 2.9: Effective area of the top layer of PCU2

In addition to selecting PCU2, the data-files were filtered using the FITS file manipulation package, *FTOOLS*, based on the following criteria.

Electron Contamination

This column of the raw data file parametrizes the contamination from electrons trapped in the earth's magnetosphere, or, from solar flare activity. Such electrons, measured by the coincidence of events between the PCU propane layer and either of the two anodes in the first layer, increase the background at low energies. Data with high electron contamination (ELECTRON2 >0.1) were neglected.

Influence of South Atlantic Anomaly

The South Atlantic Anomaly (SAA) is a dip in the geomagnetic field of the earth which allows cosmic rays to penetrate further than usual. Some the RXTE orbits pass through South Atlantic Anomaly (SAA) region, which is shown in Figure 2.10 in red. The background increases dramatically during 30 minutes of passing the peak emission of SAA resulting in a lower signal to noise. These data were discarded during the analysis for observations made prior to April 15th 1996. The background models after this date incorporate the effect of SAA passage into calculations and this screening criterion was not used.

Offset

It is the difference between the source position and the pointing of the satellite. Sometimes, however, the on-source data file will contain short stretches of data at the beginning or end of an observation that are too far away from the source. These were filtered out using a cutoff of 0.02^o.

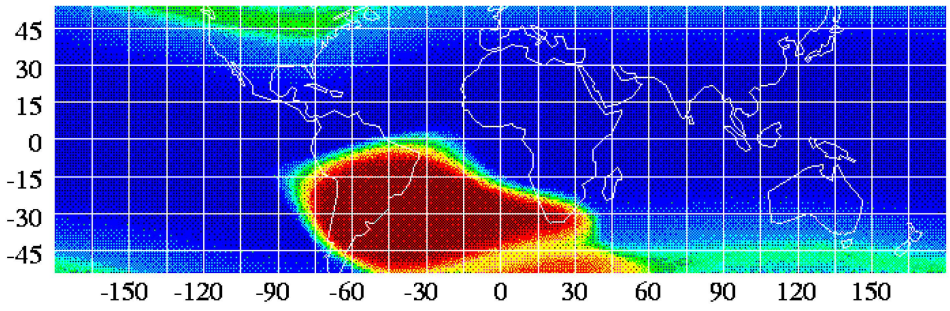

Figure 2.10: The South Atlantic Anomaly (SAA) is a dip in the geomagnetic field of the earth which allows cosmic rays to penetrate further than usual. Data collected during these times are usually excluded from the analysis due to the high particle background.

Elevation

The elevation is the instantaneous angle, in degrees, between the Earth's limb and the target subtended by the spacecraft. As the Earth's atmosphere absorbs X-rays, preferentially at low energies, the shape of the source spectrum is distorted when the elevation angle is low. Hence, data with elevation greater than 10 degrees were used for analysis.

Figure 2.11 shows a sample plot of the quantities mentioned above. Only one other PCU (# 1) has been shown, in addition to PCU 2, for comparison. PCU 2 was ON only for ~ 60 % of the time during this observations. The Electron2 column had data only for the time that PCU2 was on.

The spectrum was then generated from the filtered data by the ftool *saextrct*. This spectrum obtained from data, has contributions from the source and the background. The ftool *pcabackest*, uses the X-ray background data generated from blank sky observations (see Jahoda *et al* 2006 [54]for details) to produce the background data file. The background spectrum, generated from the corresponding background

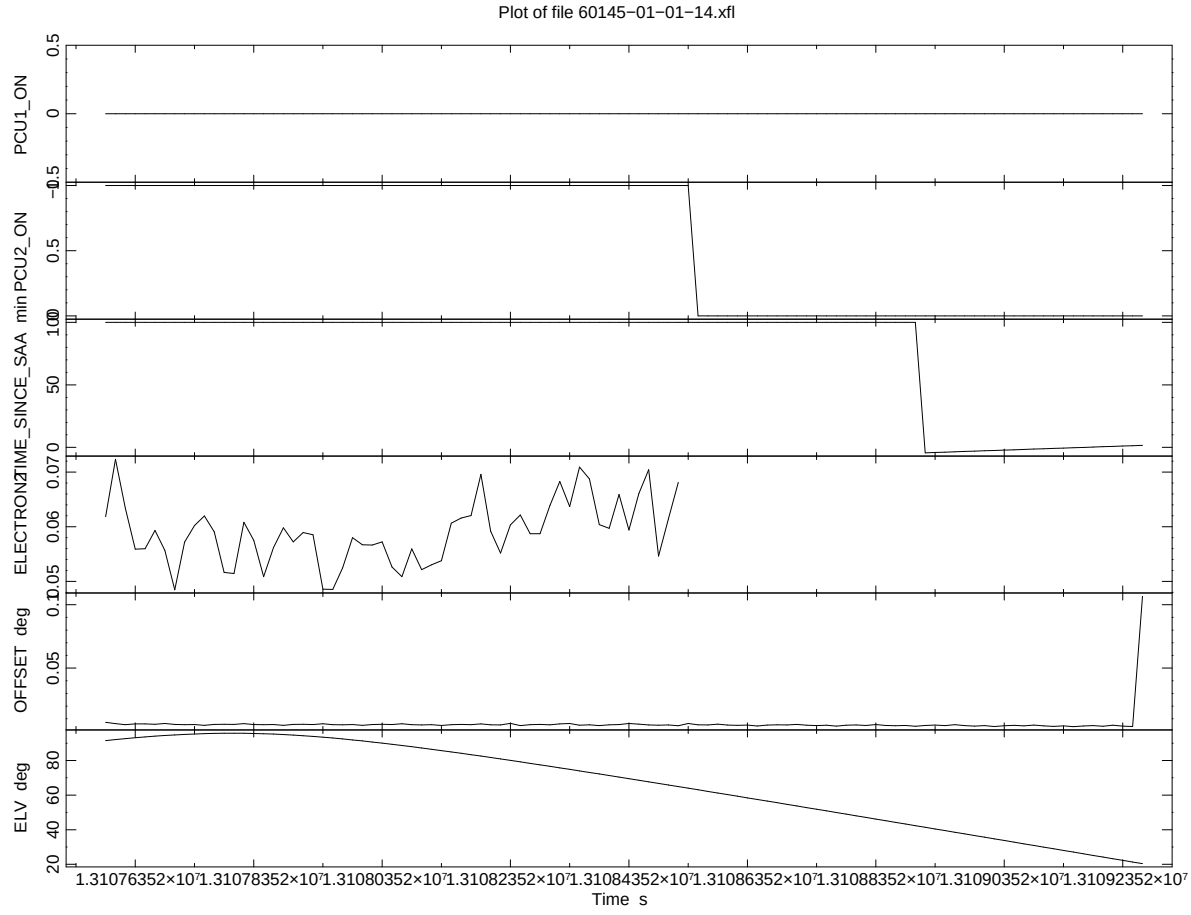

Figure 2.11: A plot of different filter criteria which are used to clean the data before getting the spectra and light curve.

file, is subtracted to get the spectrum from the source.

Figure 2.12 shows the comparison between the source and background spectrum during the brightest state recorded by the PCA instrument for Mrk 421 during the period 1996-2006. These observations were taken on April 21, 2004. The spectrum is almost equal to the background beyond 30 keV, a value that is higher than usual due source being in an extremely active state. Usually, the data beyond 20 keV did not have any significant excess above the background. On the lower side, data below 3 keV ($\sim$ channel 4) was rejected. We fit the spectrum with a simple

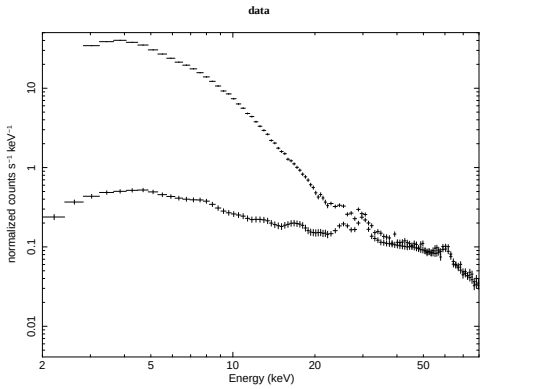

(a) Sample source and background spectra from PCA

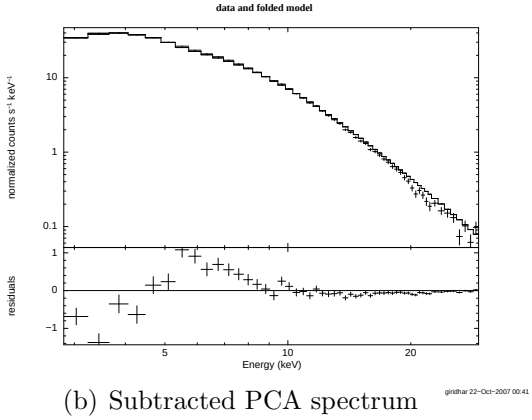

(b) Subtracted PCA spectrum

Figure 2.12: Sample

power law model convolved with the attenuation due to photoelectric absorption by intervening neutral hydrogen (Dickey & Lockman 1990 [55]). The absorption plays a greater role at soft X-ray energies (< 2 keV), and is not so severe at PCA energies. The observed flux is modeled by

$$F(E) = KE^{-\alpha}e^{-N_H\sigma(E)} \tag{2.6}$$

where , where $E_1 < E < E_2$, and K is the flux (in units of 10^{-12} erg cm^{-2} s^{-1}) recorded in energy interval, N_H is the galactic hydrogen column density, which was fixed at a value of 1.43×10^{20} atoms/cm^2, which is the average value at coordinates of the sources [1], and σ_E is the photoelectric cross section. The fits were performed using the X-ray spectral package XSPEC [2]. We obtained a power law index of 2.11 $\pm$ 0.004 for the PCA observations shown in Figure 2.12. Although the error on the spectral index is very low, mostly due to the high counts, a simple power law is clearly not a good fit, as confirmed by the residuals. Mrk 421 has its synchrotron

[1] http://heasarc.gsfc.nasa.gov/cgi-bin/Tools/w3nh/w3nh.pl
[2] http://xspec.gsfc.nasa.gov

peak in the X-ray region as a result of which the spectrum is curved.

2.2.2 HEXTE

The HEXTE, consists of two clusters of 4 NaI/CsI phoswich scintillation detectors, which are sensitive to X-rays from 15 to 250 keV. The two clusters are co-aligned with PCA and contain mutually orthogonal "rocking" mechanisms which can be moved independently to provide internal and cosmic x-ray background at 1.5^o or 3^o on either side of the source. However, the on source directions of PCA and HEXTE are closely co-aligned. The two clusters alternate between source and background for a time that could be selected from 16, 32, 64 or 128 seconds. Figure 2.13a shows the placement of HEXTE aboard RXTE, and Figure 2.13b shows one of the phoswich assemblies. Details of the HEXTE instrument can be found in Hink *et al.* (1992)[56], Rotschild *et al.*, 1989 [57] and the references therein. The effective open detector area of $1780cm^2$ ($890cm^2$ per cluster), but HEXTE has a considerable dead time (40%) which causes a reduction in effective area to $1086cm^2$ (356 per cluster). The one cluster area, which is the more significant one since there is only one cluster on source at any given time, is considerably less when compared with that of PCA.

Figure 2.14 shows the sample source, background and subtracted spectra for HEXTE observations of Mrk 421, taken on April 21, 2004 (simultaneous with PCA observations shown in Figure 2.12) obtained using the ftool *hxtlcurv*. Good data were available only from ∼13.0 keV-100 keV for this flare. The background data (as

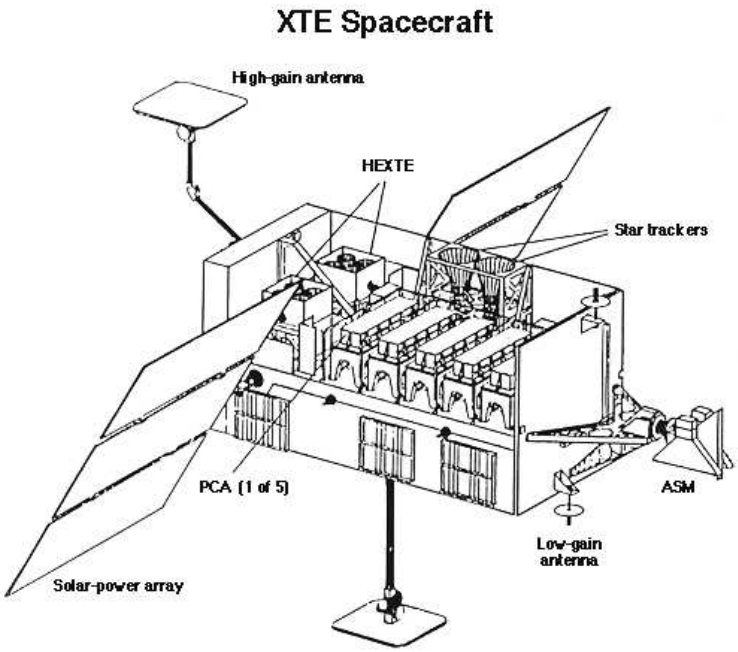

(a) Schematic view of RXTE

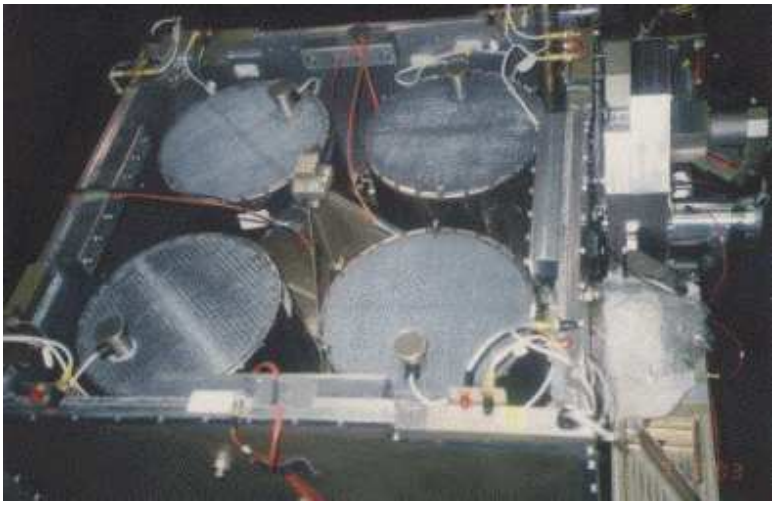

(b) Top view of HETE phoswich detectors

Figure 2.13: HEXTE instrument aboard RXTE

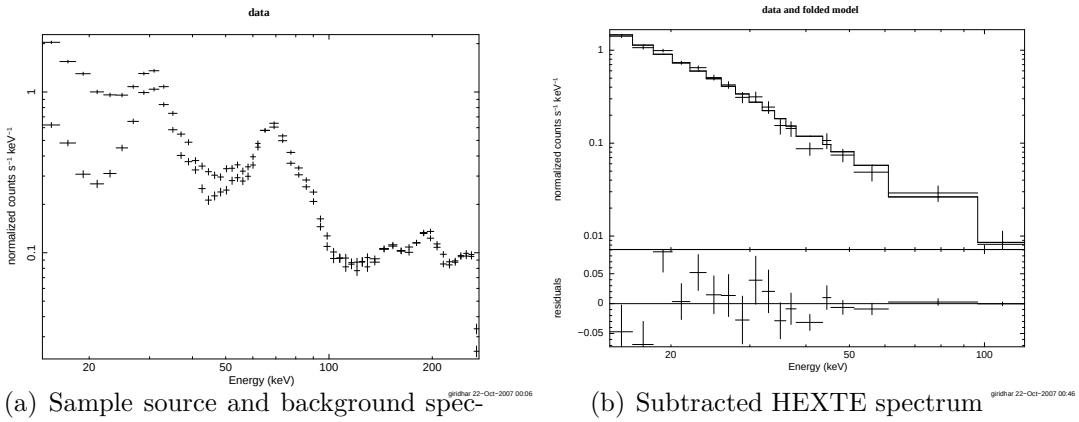

(a) Sample source and background spectra from HEXTE

(b) Subtracted HEXTE spectrum

Figure 2.14: Sample spectra from HEXTE

a fraction of source+background) in HEXTE data is much higher when compared to the background in the PCA data. The steep blazar spectrum for HBLs (indices of 2.2-2.6 in the HEXTE range) gives less photons in the HEXTE range. These two factors in addition to the reduced effective area of HEXTE, translate to longer integration times for achieving a significant detection in the HEXTE range.

Although HEXTE and PCA observations were simultaneous, data in the overlapping energy range (∼13-30 keV) yields different parameters for a power-law fit, primarily because of the difference in calibration, particularly of effective area. A simultaneous fit using the absorbed power law model in the energy range of 13-30 keV can give the relative normalization between the two instruments. Figure 2.15 shows the snapshot of an XSPEC fit. Choosing PCA as the preferred instrument for the fit, we obtained a power law index of 2.38±0.05 and a relative normalization of 0.78 for the HEXTE instrument (with PCA fixed at 1). This factor manifests itself in a νF_ν plot, as a gap between the two spectra, as shown in figure 2.16. Consequently, the HEXTE data can be scaled by a factor of 1.28 for the spectra to

overlap in the 13-30 keV interval.

```
#========================================================================
#Model constant<1>*wabs<2>*pegpwrlw<3> Source No.: 1   Active/On
#Model Model Component  Parameter  Unit     Value
# par  comp
#                          Data group: 1
#   1    1   constant   factor              1.00000      frozen
#   2    2   wabs       nH         10^22    1.43000E-02  frozen
#   3    3   pegpwrlw   PhoIndex            2.38194        6.32884E-02
#   4    3   pegpwrlw   eMin       keV      13.0000      frozen
#   5    3   pegpwrlw   eMax       keV      30.0000      frozen
#   6    3   pegpwrlw   norm               779.282        11.2383
#                          Data group: 2
#   7    1   constant   factor              0.783606       1.68023E-02
#   8    2   wabs       nH         10^22    1.43000E-02  = 1:wabs[2]:nH
#   9    3   pegpwrlw   PhoIndex            2.38194      =
1:pegpwrlw[3]:PhoIndex
#  10    3   pegpwrlw   eMin       keV      13.0000      frozen
#  11    3   pegpwrlw   eMax       keV      30.0000      frozen
#  12    3   pegpwrlw   norm               779.282      = 1:pegpwrlw[3]:norm
#------------------------------------------------------------------------
#
#
# Chi-Squared =          30.05 using 32 PHA bins.
# Reduced chi-squared =          1.036 for     29 degrees of freedom
```

Figure 2.15: A snapshot of the XSPEC output screen showing the relative normalization of 0.783 between PCA and HEXTE, determined from a simultaneous fit to the data over the energy range 13-30 keV.

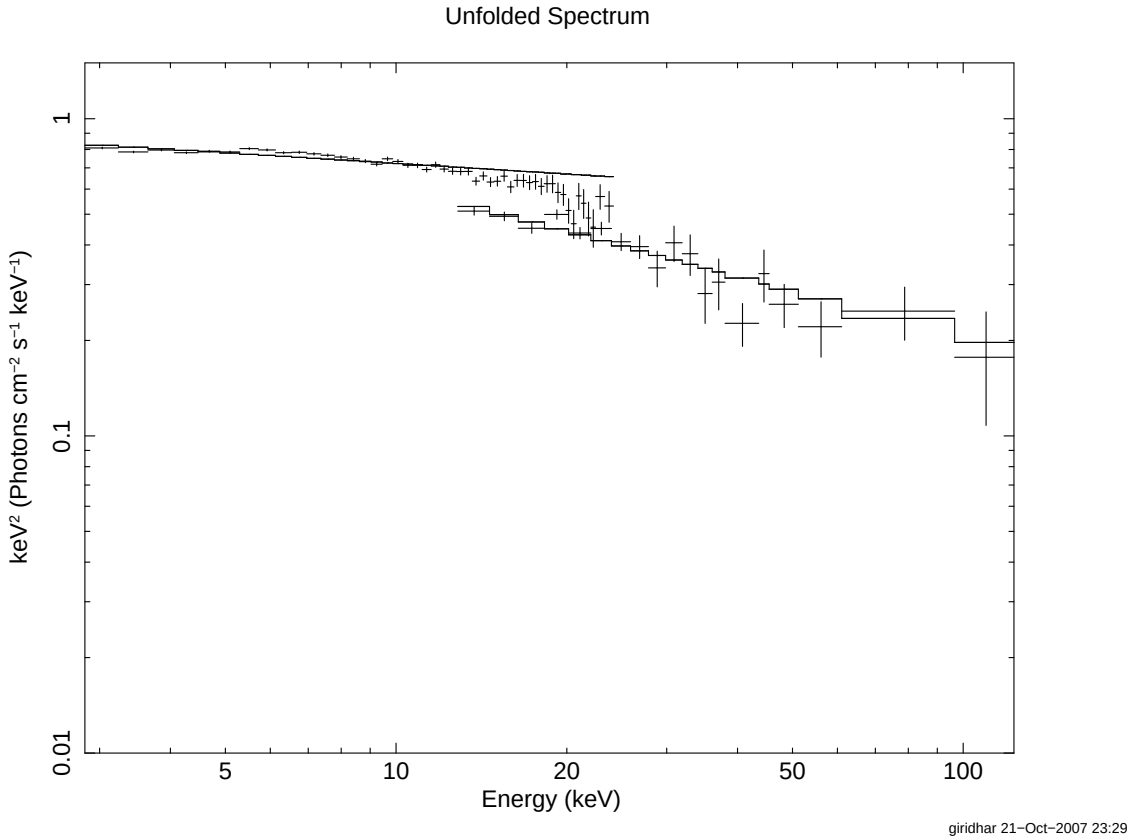

Figure 2.16: A νF_ν plot for PCA and HEXTE data during the observations for Mrk 421 on April 21, 2004. The shift in the spectra in the overlapping interval of 13-30 keV region is due to difference in the calibration.

Chapter 3

Does the Blazar Gamma-ray Spectrum Harden with Increasing Flux? - Analysis of Nine Years of EGRET Data

This work was done in collaboration with the following people-

Dr. Keith M. Jahoda, Dr. R. C. Hartman, and Dr. Jean H. Swank from the NASA-Goddard Space Flight Center, Greenbelt Maryland

Dr. P. Sreekumar, Indian Space Research Organization, Bangalore, India

Dr. R. Mukherjee, Barnard College & Columbia University, New York

Dr. Markus Böttcher, Astrophysical Institute, Ohio University, Athens, Ohio

and was published in "The Astrophysical Journal", Vol 657, 706.

3.1 Introduction

Blazars are a class of Active Galactic Nuclei (AGNs) characterized by highly luminous and rapidly variable continuum emission at all observed frequencies from radio to gamma-rays. VLBI structures of these sources reveal compact cores with jet-like features which often show evidence of superluminal motion [58]. The broadband spectral energy distribution (SED) of these sources shows two peaks. It has been widely accepted, in the scenario of leptonic models, that the lower-frequency peak is due to synchrotron emission from relativistic plasma moving along the jet away from the core of the AGN while the second peak is attributed to inverse-Compton

scattering of relativistic electrons by soft ambient photons, produced either internal or external to the jet. These "seed-photons" for inverse-Compton emission could come from synchrotron emission itself as postulated by synchrotron-self Compton (SSC) models [14, 15, 16, 17], or they could be entering the jet directly from the accretion disk as in the ECD (external Compton scattering of direct disk radiation) models [18, 19], or they could reach the jet after being re-scattered by surrounding broad-line-region (BLR) clouds as in the ECC (external Compton scattering from clouds) models [20, 21, 22]. In addition, the BLR could also reflect the synchrotron photons back into the jet to undergo inverse-Compton scattering (External-Reflection-Compton model; [23]). Finally, the seed photons could be produced by the infrared (IR) dust that surrounds the blazar nucleus (External Compton from infrared dust-ERC(IR); [24, 25]). The dust is more concentrated in a torus that lies in the equatorial plane of the blazar [26]. Quite often, a combination of these models is required to fit the broadband spectrum of a blazar through the entire range of frequencies from radio to gamma-rays.

Observationally, the class of blazars includes flat-spectrum radio quasars (FSRQs) and BL Lac objects. FSRQs have strong and broad optical emission lines while the lines are weak in BL Lac objects. The position of the peaks in a broadband SED allows a further division of BL Lac objects into two categories: low-frequency-peaked BL Lacs (LBLs) and high-frequency peaked BL Lacs (HBLs). The first peak is at infra-red/optical frequencies for *red blazars* which could be either the FSRQs or the Low-frequency-peaked blazars (LBLs) and at UV/X-rays for *blue blazars* or the High-frequency-peaked blazars (HBLs). The second peak is in the gamma-ray

range (MeV-GeV) for LBLs & FSRQs and in the TeV range for HBLs. HBLs are much lower in overall luminosity than FSRQs with LBLs somewhere between [12].

During its nine year lifetime, EGRET has detected GeV-range emission from more than 67 blazars and a number of them have been observed multiple times [8]. The EGRET energy range (30 MeV-10 GeV) lies near the maximum or on the falling portion of the inverse-Compton peak for FSRQs and on the rising portion of the peak in the case of HBLs and it lies somewhere in between for LBLs. A continuity in the observed spectral properties of BL Lacs and FSRQs has been postulated by [12] with the gamma-ray spectral index getting progressively harder from FSRQs to HBLs. While this trend is expected of the average spectral properties of these sources, previous studies have suggested a hardening of the gamma-ray spectral index in FSRQs with an increase in flux. This was reported for individual blazars in [59, 60, 61, 62] and was also observed in the combined data from 18 brightest blazars [63]. This feature, coupled with the fact that the average spectral index of 2.15 ± 0.04 measured for blazars [36] is quite close to the spectral index of 2.10 ± 0.03 [64] for diffuse gamma-ray background, is used to attribute the extragalactic gamma-ray background to emission from unresolved blazars [65].

With the EGRET's calibration finalized and its archive now complete, the behavior of gamma-ray spectral index can be studied in detail across different epochs and over a broad range of flux. This paper presents the results of such an effort and is organized as follows. We reanalyzed the entire blazar data from the EGRET mission for this project. Section 3.2 describes the data and § 3.3 discusses the analysis procedure. We examine the spectral properties of different source classes,

the long term and the short term spectral variability in § 3.4, discuss the implications of the results in § 3.5, and summarize in § 3.6.

3.2 Source Selection and Observations

CGRO was launched on April 5 1991 and it re-entered the earth's atmosphere on June 4, 2000. One of the four instruments on board was EGRET that was sensitive in the energy range 30 MeV-10 GeV. The Third EGRET Catalog [8] contains the basic results (flux and spectral indices) from analysis of all observations till the end of Cycle 4 (October 3 1995). [36] presented summary results for all blazars detected through the end of Cycle 4 and included the spectral indices for blazars that were detected at a significance greater than 6σ. Although there were very few new detections after Cycle 4 (e.g. PKS 2255-282, Mrk 501), 8 blazars were observed multiple times in Cycles 5-9. Spectral analysis results after Cycle 4 are available only for PKS 0528+134 [66], which contains results through the end of Cycle 6.

EGRET viewing periods (VP) ranged in duration from 3 to 20 days but they were usually a week long. Sometimes an object was observed during two or more contiguous viewing periods as a part of the observing schedule or because the object was in an extremely active state. EGRET was operated with a narrow field of view for most of the latter half of the mission (Cycle 5 onward) to conserve gas lifetime, thus limiting the number of accessible targets. The details (viewing period number, start and end dates, field of view mode- normal/narrow) of the viewing periods (after Cycle 4) are listed in columns 1-4 of Table 3.1. Columns 4 & 5 list the sources

that were in the field of view (FOV) during that time, and their off-axis viewing angle respectively. Information for viewing periods prior to Cycle 5 are listed in 3EG.

We have analyzed all nine years of data for all the blazars seen by EGRET, and these objects are listed in Table 3.2. The sample consists of 98 sources, 67 of which are confirmed identifications. The 31 "possible" identifications are marked by a "?" in column 2, and the more common names of the sources are listed in column 3. The distribution consists of 66 flat-spectrum radio quasars (FSRQ), 17 low-frequency peaked BL Lacs (LBL), 4 high-frequency peaked BL Lacs (HBL), 10 flat-spectrum radio sources (FSRS) and 1 radio galaxy. The classifications (listed in column 10 of Table 3.2) have been adopted from [67] and [27]. The 66 flat-spectrum radio quasars have been further classified into 19 high-polarization quasars (FSRQ(HP)), 15 low-polarization quasars (FSRQ(LP)). Polarization information could not be obtained for the remaining. Twenty-six of the 97 sources were observed multiple times and were bright enough during those observations to yield a spectral index. These sources are marked by a "Y"in column 9.

Table 3.1: Details of the Viewing Periods(after Cycle 4) included in the analysis and the sources that were analyzed

Viewing Period[a]	**Start Date**	**End Date**	**Sources**	**Viewing Angle**[b]
502.0	10/17/95	10/31/95	PKS 0528+134	0.86
511.0	01/16/96	01/30/96	1253-055(3C 279)	6.72
511.5	01/30/96	2/06/96	1253-055(3C 279)	5.01
			1226+023(3C 273)	15.36

Continued on Next Page...

Table – Continued

Viewing Period[a]	Start Date	End Date	Sources	Viewing Angle[b]
513.0	02/06/96	02/13/96	PKS 2155-304	0.16
515.0	02/20/96	03/05/96	1101+384(Mrk 421)	18.45
516.1	03/18/96	03/21/96	PKS 1622-297	10.91
516.5	03/21/96	04/03/96	PKS 1633+382(4C+38.41)	1.13
			PKS 1611+343(OS+319)	6.68
			Mrk 501	0.07
517.0	03/05/96	03/18/96	PKS 0208-512	2.25
518.5	04/03/96	04/23/96	S5 0716+714	0.00
519.0	04/23/96	05/07/96	PKS 1633+382(4C+38.41)	2.75
			PKS 1611+343(OS+319)	8.56
			Mrk 501	1.23
520.4	05/21/96	05/28/96	PKS 2155-304	0.00
526.0	07/30/96	08/13/96	PKS 0528+134	8.29
527.0	08/13/96	08/20/96	PKS 0528+134	9.27
528.0	08/20/96	08/27/96	PKS 0528+134	12.13
606.0	12/10/96	12/17/96	1226+023(3C 273)	11.34
			1253-055(3C 279)	1.00
607.0	12/17/96	12/23/96	1226+023(3C 273)	11.33
			1253-055(3C 279)	1.00
608.0	12/23/96	12/30/96	1226+023(3C 273)	11.24
			1253-055(3C 279)	1.01
609.0	12/30/96	01/07/97	1226+023(3C 273)	11.19
			1253-055(3C 279)	1.01
610.0	01/07/97	01/14/97	1226+023(3C 273)	11.19
			1253-055(3C 279)	1.01
610.5	01/14/97	01/21/97	1226+023(3C 273)	9.60
			1253-055(3C 279)	1.99
611.1	01/21/97	01/28/97	1226+023(3C 273)	11.16
			1253-055(3C 279)	1.01
616.1	02/18/97	03/18/97	PKS 0528+134	0.00
617.8	04/09/97	04/15/97	PKS 1633+382(4C+38.41)	6.71
			PKS 1611+343(0S+319)	12.57
			Mrk 501	2.99
621.5	06/17/97	06/24/97	1226+023(3C 273)	8.64
			1253-055(3C 279)	1.99
623.5	07/15/97	07/22/97	BL Lac	0.00
625.0	08/05/97	08/19/97	PKS 1622-297	17.68
615.1	08/19/97	08/26/97	PKS 1622-297	0.00
701.0	11/11/97	11/18/97	PKS 2155-304	4.92
708.0	12/30/97	01/06/98	PKS 2255-282	12.95

Continued on Next Page...

Table – Continued

Viewing Period[a]	**Start Date**	**End Date**	**Sources**	**Viewing Angle**[b]
709.1	01/06/98	01/13/98	PKS 2255-282	12.95
715.5	03/20/98	03/27/98	PKS 1156+295	2.00
716.5	03/27/98	04/02/98	PKS 1156+295	17.98
806.5	01/19/99	01/26/99	1253-055(3C 279)	6.30
806.7	01/26/99	02/02/99	1253-055(3C 279)	2.87
910.0	02/08/00	02/23/00	1253-055(3C 279)	4.00
911.1	02/23/00	03/01/00	1253-055(3C 279)	8.40

3.3 Analysis

EGRET was a spark chamber telescope with an effective area of 1000 cm^2 at 150 MeV, 1500 cm^2 between 500 MeV-1 GeV, decreasing gradually to about 700 cm^2 at 10 GeV. The off-axis sensitivity decreased as an approximate Gaussian with a full-width-half-maximum of $\sim 20^o$. The sensitivity beyond 30^o was less than 15% of the on-axis sensitivity. Details of the instrument and calibration can be found in [100, 99, 46]; and [49]. During its nine year lifetime, the spark chamber gas was refilled multiple times [51], and for most of the latter half of the mission (Cycle 5 onward), EGRET was operated with a narrow field of view (18^o useful radius) to conserve gas lifetime. The detection efficiency of EGRET varied throughout the mission (see section 2.1 for details. We used the EGRET maps that were regenerated to include the changes in performance (as descrived in [51]) for our analysis.

One of the standard EGRET data products for any viewing period is a pair of maps showing gamma-ray arrival directions from the observed sky-region in the energy intervals 30-100 MeV and 100-10000 MeV. For the work presented here, these maps were used in conjunction with a list of all the known EGRET-sources,

[a]EGRET was operated in the reduced field of view mode during all the viewing periods to conserve gas.

[b]Viewing angle is in degrees

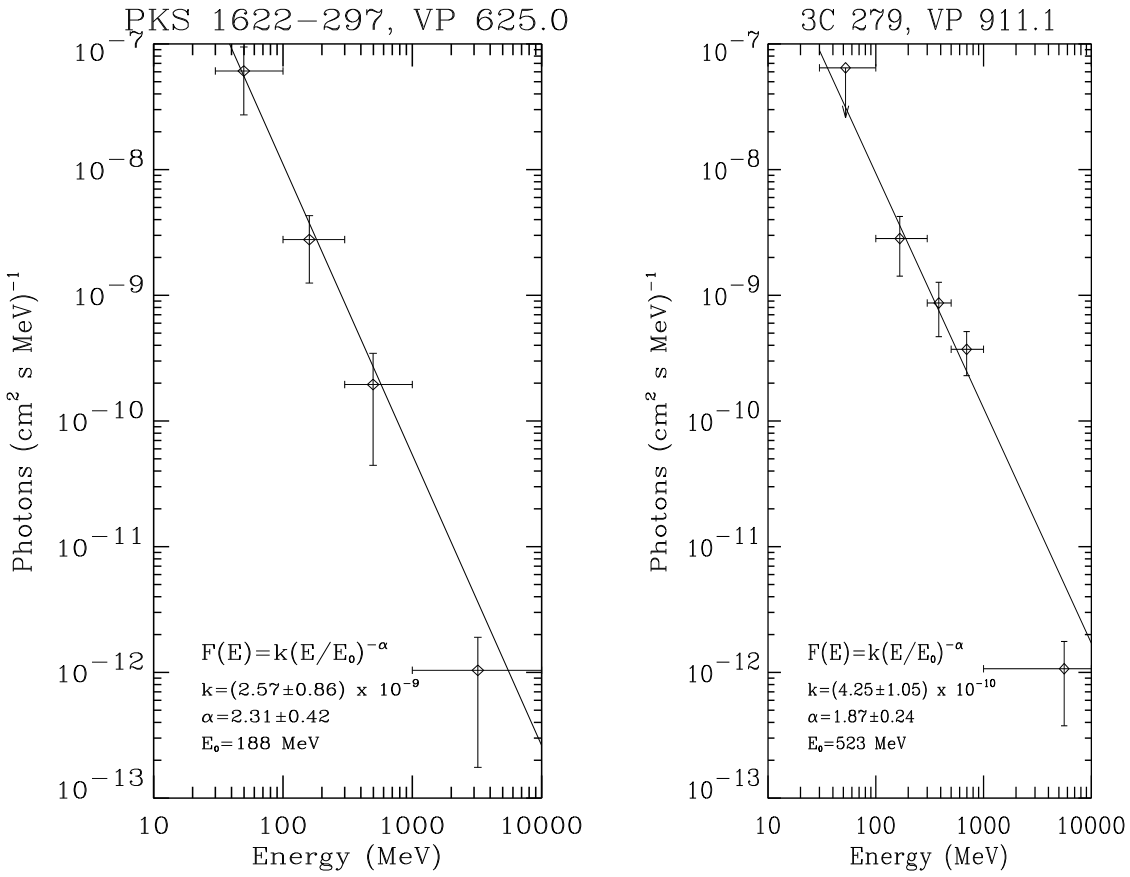

(a) 4 point spectrum for PKS 1622-297 from VP 625.0, August 1997

(b) PKS 0528+134 Spectrum from VP 0.2

Figure 3.1: EGRET spectra for PKS 1622-297 and 3C 279. The straight line is a power law fit to the data. The fit parameters (discussed in section 3.3) are included in the figure.

to determine simultaneously the counts from all sources in the field of view and their significance of detection in the two energy-intervals through a method of maximum likelihood. All sources that were detected at a significance $< 2\sigma$ in the energy interval 100-10000 MeV were eliminated from the list and the process was repeated again to determine the counts and fluxes (along with the associated errors) for the remaining sources.

If the source of interest was detected at a significance $> 4\sigma$ in the energy interval 100 MeV-10000 MeV, then a four point spectrum was determined using counts recorded in the energy intervals (in MeV) 30-100, 100-300, 300-1000 & 1000-10000. The points were fitted with a single power law of the form $F(E) = k(E/E_o)^{-\alpha}$ photons cm^{-2} s^{-1} MeV^{-1} where $F(E)$ is the flux, α the photon spectral index, E the photon energy, E_o the energy normalization factor and k a coefficient of normalization.

If the overall significance of detection of the source was greater than 6σ, the energy intervals with a strong detection were further split up into smaller intervals (for which standard EGRET maps exist) to determine the spectral index. For the strongest sources, the standard 10 intervals 30-50, 50-70, 70-100, 100-150, 150-300, 300-500, 500-1000, 1000-2000, 2000-4000, 4000-10000 (all in MeV) were utilized. Most of the spectra after Cycle 5 had to be determined using 4-5 energy intervals (when a source was not undergoing a flare). Figure 3.1 shows sample four-point spectra from PKS 1622-297 and a 5-point spectrum from 3C 279. Analysis using the new maps has constrained the spectral indices better (lower errors) for a majority of the sources. Previous EGRET spectral analyses required a minimum of 6-sigma significance of source detection and used 10 energy bins to calculate the spectrum. We have used a slightly different approach, lowering the cutoff to 4 sigma. This does not affect the quality of the spectral analysis since we are using only 4-5 energy intervals for computing the spectral indices for faint sources, giving us better statis-

tics in each bin, and lowering the errors. In addition, we found that the spectral index was within the error bars of the index calculated using 10 energy bins.

Some of the blazars considered here were part of extended campaigns. If the source was not very bright during such times, adjacent viewing periods were combined. The analysis process was then repeated with the combined data, and an attempt was made to extract the spectrum. The longest period for which a source was in EGRET's field of view continuously was 49 days (7 viewing periods), for 3C 273 and 3C 279. Sometimes, all the observations during a cycle had to be combined to obtain a reliable detection and spectrum.

We have done a complete spectral analysis for all the blazars detected by EGRET using the recalibrated data products. Table 3.2 (column 6) shows their average photon spectral indices. For the bright blazars that were observed multiple times, we used the sample mean and standard deviation (of mean) as the spectral index. For the rest, we used the spectral index from all the data available unless a source was bright during one of the observations and was almost inactive during the rest of the viewing periods. Column 7 lists the mean flux (> 100 MeV) recorded for these sources in units of 10^{-8} photons cm^{-2} sec^{-1}. Table 3.3 lists the results of spectral analyses for sources which yielded more than one spectral index value. Columns 5, 6 & 7 list the spectral index, flux and the detection significance, respectively. The viewing periods that were combined to get the spectra are listed in column 3 while their corresponding starting dates are listed in column 2 in the same order. For identification purposes, each of these observations is labeled in the spectral index vs. flux plot shown in Figure 3.3, with the labels listed in column 4 of Table 3.3.

3.4 Results

3.4.1 Gamma-ray spectral distribution

Since a classification of blazars was based on the location of the synchrotron peak, we searched the literature for multiwavelength fits to data from all the blazars detected by EGRET, in order to determine the frequency of their synchrotron peaks and to examine its dependence on the gamma-ray spectral index. Multiwavelength fits to the broadband spectrum ($log(\nu F_\nu)$ vs $log(\nu)$) from simultaneous data are available for more than one epoch for: 3C 279 [38, 68], BL Lac [69], 3C 273 [70], PKS 2155-304 [71, 72], Mrk 421 [73, 74, 75], Mrk 501 [76, 77, 78, 79], PKS 0528+134 [66]. For the rest of the blazars, we used values from [27] & [37] that are compilations of multiwavelength data (simultaneous and non-simultaneous) from literature and corresponding broadband model-fits. In cases where there is more than one fit available, or when a clear determination of the peak was not possible, the peak frequency was fixed at the average value and the error was calculated from one of the extremes. The logarithm of synchrotron peak frequency values have been listed in column 8 of Table 3.2. The plot of gamma ray spectral index vs log synchrotron peak frequency for the blazars in our sample is shown in Figure 3.2. The sample of sources shown in the plot consists of 37 FSRQs, 10 LBLs and 3 HBLs. Since FSRQs have the lowest synchrotron-peak frequency and the EGRET energy range lies on the decreasing portion of their inverse Compton peak (in a plot of the broadband spectral energy distribution), they are expected to have soft spectral indices. HBLs have the highest synchrotron peak frequency and the EGRET-range lies on the rising portion of their inverse Compton peak. Consequently, they are expected to have hard spectral indices. LBLs lie somewhere in between. Under this unified-blazar paradigm, a plot of gamma-ray spectral indices vs. synchrotron peak frequencies should have a smooth variation from FSRQs to LBLs to HBLs [12]. A plot similar

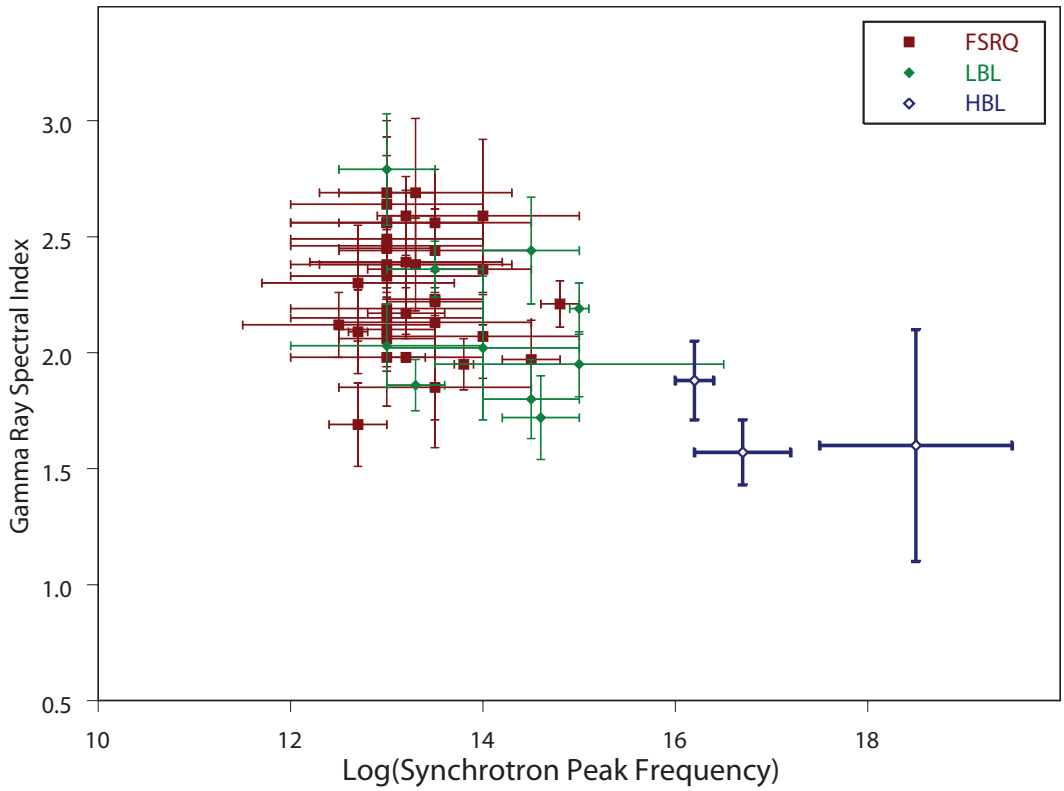

Figure 3.2: Spectral index vs Log(Synchrotron Peak Frequency) of blazars. Classifications are based on [27] and [67]. The sample of sources shown in the plot consists of 37 FSRQs, 10 LBLs and 3 HBLs. The data for the plot comes from Table 3.2

to that shown in Figure 3.2 was made in the past for 27 blazars using data through Cycle 4 [80]. A comparison of our data with this work shows that some of the spectral indices obtained by us are different, due to the availability of more data and the recalibration of the raw data products, as described earlier (see section 3). We obtained a mean spectral index of 2.26±0.03 for the 66 FSRQs, 2.14±0.08 for the 17 LBLs, 1.68±0.09 for the 3 HBLs and 2.48±0.1 for the 10 other flat spectrum radio sources (FSRS). The spectral index for FSRQs with high polarization (HP) and low polarization (LP) was 2.19±0.06 and 2.32±0.06 respectively. The spectral index increases across HBLs, LBLs, FSRQs(HP) and FSRQs(LP). This is consistent with the prediction that the spectral properties of blazars form a well defined sequence from HBLs to LBLs to FSRQs (HP,LP) [27, 12].

Table 3.2: Photon Spectral index (30 MeV -10 GeV), average flux (> 100 MeV) and Log(synchrotron peak frequency) of blazars detected by EGRET

Source	**"?"**	**Other names**	**RA** [a]	**DEC** [a]	**Spectral index** [b]	**Flux >100 Mev** [c]	**Log(ν_{sync})** [d]	**Mult. Obs**	**Class**[f]
0119+041	?	PKS, OC+033	19.60	2.81	2.24±0.34	12.6±4.3		N	FSRQ(HP)
0130-171	?	PKS	22.70	-17.97	2.37±0.29	12.4±3.8		N	FSRQ
0202+149		PKS	31.11	14.97	1.98±0.21	23.0±5.5	13±1	N	FSRQ(HP)
0208-512		PKS	32.58	-50.93	1.95±0.11	88.6±4.2	13.8±0.1	Y	FSRQ(HP)
0219+428		3C 66A	35.70	42.9	1.95±0.14	17.7±2.8	15.0±1.5	Y	LBL
0234+285	?	4C+28.07	39.99	28.26	2.56±0.23	12.7±2.9	13.5±1	N	FSRQ(HP)
0235+164		PKS, OD 160	39.36	16.59	1.86±0.11	25.4±3.6	13.3±0.3	N	LBL
0336-019		CTA 026	55.04	-2.02	1.87±0.22	15.5±3.5		N	FSRQ(HP)
0414-189			63.14	-18.88	1.96±0.45	44.2±15.5		N	FSRQ
0415+379	?	3C111	64.04	36.84	2.55±0.24	12.2±2.6		N	FSRQ
0420-014		PKS	65.65	-1.04	2.59±0.17	15.0±3.0	13.2±0.3	N	FSRQ(HP)
0430+2859	?		68.40	29.14	1.97±0.10	21.30±2.8	···	Y	LBL
0440-003		PKS, NRAO 190	70.55	-0.55	2.23±0.12	11.6±2.7	13.5±0.5	N	FSRQ(HP)
0446+112		PKS	72.61	11.09	2.19±0.15	14.0±2.0	13±1	N	FSRQ
0454-234		PKS	74.24	-23.64	2.27±0.32	7.5±2.5		N	LBL
0454-463		PKS	74.57	-46.60	2.56±0.37	7.8±2.1	13±1	N	FSRQ(LP)
0458-020	?	PKS	75.10	-1.99	2.45±0.22	10.2±2.2		N	FSRQ(HP)
0459+060	?		74.93	5.75	2.06±0.36	9.7±3.1		N	FSRQ
0506-612	?	PKS	78.15	-61.84	2.37±0.29	5.7±1.8		N	FSRQ
0521-365	?	PKS	82.54	-36.44	2.36±0.24	19.3±3.5	14.0±0.5	N	FSRQ(HP)
0528+134		PKS	82.74	13.38	2.36±0.03	95.8±3.7	13.0±0.2	Y	FSRQ(LP)

Continued on Next Page...

Table 3.2 Continued

Source	**"?"**	**Other names**	**RA** [a]	**DEC** [a]	**Spectral index** [b]	**Flux >100 Mev**[c]	**Log(ν_{sync})** [d]	**Mult. Obs**	**Class**[f]
0537-286	?	PKS, OG-263	82.91	-29.68	2.23±0.50	32.6±11.5		N	FSRQ
0537-441		PKS	85.02	-44.05	2.36±0.12	24.3±3.0	13.5±0.5	Y	LBL
0539-057	?	PKS	85.57	-6.93	1.88±0.34	65.0±19.8		N	FSRQ
0616-116			95.58	-11.66	2.74±0.31	17.8±4.7		N	FSRS
0716+714		S5	110.43	71.35	2.19±0.11	18.4±2.1	15.0±0.1	Y	LBL
0735+178			114.47	17.35	2.44±0.23	14.8±3.1	14.5±0.5	N	LBL
0738+5451			115.83	54.80	2.00±0.19	11.1±2.1		N	FSRS
0803+5126	?		122.15	51.24	2.78±0.27	9.4±2.4		N	FSRQ
0805-077	?		123.14	-6.78	2.39±0.31	24.6±5.5	13.2±1	N	FSRQ
0804+499	?		122.18	48.75	2.13±0.42	9.9±2.4	13.5±1	N	FSRQ(HP)
OR 0809+483									
0827+243		OJ 248	127.49	24.22	2.38±0.2	25.4±3.9	13.3±1	Y	FSRQ(LP)
0829+046		OJ+049	127.03	5.14	2.42±0.42	16.1±4.9		N	LBL
0836+710		4C +71.07	131.46	70.83	2.69±0.16	9.7±1.7	13±0.5	N	FSRQ(LP)
0847-120			133.16	-12.27	1.48±0.26	44.4±11.8		N	FSRQ
0851+202		PKS, OJ 287	133.42	19.68	1.91±0.28	10.4±3.0		N	LBL
0917+449	?		139.33	44.45	2.06±0.14	14.1±2.1	13.0±0.5	Y	FSRQ(LP)
0954+556		4C 55.17	148.01	55.02	2.07±0.18	9.5±1.6	14.0±1.0	Y	FSRQ(HP)
0954+658		S4	149.62	65.56	2.03±0.18	6±1.6	13±1	N	LBL
1011+496	?		152.29	48.93	1.85±0.32	4.7±1.4		N	LBL
1055+567	?		163.21	57.31	2.15±0.37	9.0±2.4		N	LBL
1101+384		Mrk 421	166.10	38.15	1.57±0.14	13.6±1.8	16.7±0.5	Y	HBL
1127-145	?	PKS	173.66	-15.50	2.30±0.25	37.8±8.2	12.7±1	N	FSRQ(LP)
1156+295		PKS	180.12	28.80	1.97±0.17	8.7±1.8	14.5±0.3	Y	FSRQ(HP)

Continued on Next Page...

Table 3.2 Continued

Source	**"?"**	**Other names**	**RA** [a]	**DEC** [a]	**Spectral index** [b]	**Flux >100 Mev**[c]	**Log(ν_{sync})** [d]	**Mult. Obs**	**Class**[f]
1219+285		PKS, W Comae, ON 231	185.75	28.70	1.80±0.17	11.5±1.5	14.5±0.5	Y	LBL
1222+216		4C 21.35	186.11	21.31	2.33±0.1	15.1±1.8	13±1	Y	FSRQ(LP)
1226+023		3C 273	185.25	2.17	2.56±0.07	19.5±1.7	13±1	Y	FSRQ(LP)
1229-021		PKS, 4C-02.55, ON-049	187.65	-2.79	2.64±0.36	5.5±1.5	13±1	N	FSRQ(LP)
1237+0459	?		188.91	4.97	2.78±0.32	4.8±1.5		N	FSRS
1243-072		PKS, ON-073	191.75	-6.86	2.75±0.17	8.4±1.9		N	FSRQ
1253-055		3C 279	193.98	-5.82	1.98±0.02	81.8±2.5	13.2±0.2	Y	FSRQ(HP)
1313-333	?	PKS, OP-322	198.51	-34.52	2.09±0.18	35.5±3.3	12.7±0.1	N	FSRQ
1322-428	?	PKS, Cen. A	201.15	-43.25	2.54±0.23	13.5±2.5		N	Radio Gal.
1324+224	?		200.80	22.01	1.62±0.24	17.9±4.1		N	FSRQ
1331+170		OP 151	202.39	17.14	2.38±0.38	7.6±2.6		N	FSRQ
1334-127		PKS	204.84	-14.32	1.92±0.25	11.9±3.3		N	FSRQ(HP)
1406-076		PKS	212.42	-7.75	2.21±0.10	31.3±3.0	14.8±0.2	Y	FSRQ(LP)
1424-418		PKS	217.39	-42.30	2.10±0.16	11.0±2.6	13.0±0.5	N	FSRQ(HP)
1504-166	?	PKS	226.20	-15.63	1.79±0.34	32.1±10.1		N	FSRQ
1510-089		PKS	228.17	-8.83	2.45±0.21	18.1±3.7	13.0±0.5	N	FSRQ(HP)
1514-241	?	PKS	229.34	-25.65	2.67±0.41	26.6±8.1		N	LBL
1604+159		4C+15.54	241.30	15.89	2.02±0.31	11.0±3.9	14±1	N	LBL
1606+106		4C 10.45	242.12	10.93	2.44±0.18	25.4±4.5	13.5±1	N	FSRQ(LP)
1611+343		OS+319	243.54	34.40	2.35±0.15	27.6±4.0		Y	FSRQ
1622-253		PKS	246.50	-25.32	2.12±0.14	24.2±3.5	12.5±1	Y	FSRQ(LP)
1622-297		PKS	246.36	-29.92	2.17±0.11	47.7±3.5	13.2±0.4	Y	FSRQ(LP)
1633+382		4C+38.41	248.92	38.22	2.15±0.08	59.±5.2	13±1	Y	FSRQ(LP)

Continued on Next Page...

Table 3.2 Continued

Source	**"?"**	**Other names**	**RA** [a]	**DEC** [a]	**Spectral index** [b]	**Flux >100 Mev**[c]	**Log(ν_{sync})** [d]	**Mult. Obs**	**Class**[f]
1652+398		Mrk 501	253.47	39.76	1.48±0.44	10.1±4.1	18.5±1.0	N	HBL
1716-771	?		260.22	-78.34	2.08±0.47	19.8±6.9		N	FSRS
1725+044		PKS	261.97	4.50	2.63±0.26	16.2±3.9		N	FSRQ
1730-130		NRAO 530	263.46	-13.23	2.38±0.08	35.0 ± 3.3	13±1	Y	FSRQ
1739+522		4C+51.37	264.64	52.05	2.49±0.21	21.0 ±3.9	13±1	N	FSRQ
1741-038		PKS	266.02	-3.18	2.59±0.33	18.4 ±5.2	14±1	N	FSRQ(HP)
1759-396			270.22	-39.93	2.96±0.26	10.3±2.8		N	FSRS
1804-502	?	J1808-5011	271.55	-50.10	2.86±0.34	6.2±2.7		N	FSRS
1830-210			278.10	-21.18	2.62±0.13	26.6±3.6		Y	FSRQ
1908-201			287.93	-20.00	2.31±0.18	16.0±2.6		N	FSRS
1920-211	?		290.50	-20.26	2.37±0.48	28.3±8.0		N	FSRS
1933-400		PKS	293.98	-40.38	2.69±0.32	8.3±2.6	13.3±1	N	FSRQ
1936-155		PKS	294.47	-15.49	2.32±0.42	55.4±18.7		N	FSRQ
2002-233		TXS	301.54	-23.35	2.35±0.27	16.7±4.2		N	FSRS
2005-489	?	PKS	302.35	-48.83	···	11.0±4.4		N	HBL
2022-077			306.36	-7.75	2.32±0.17	20.0±3.5		N	FSRQ
2032+107		PKS	309.18	11.54	2.79±0.24	14.4±3.1	13.0±0.5	N	LBL
2052-474		PKS	313.80	-47.28	1.85±0.26	21.4±5.8	13.5±1	N	FSRQ(LP)
2105+598	?		315.18	60.21	2.07±0.24	19.4±4.1		N	FSRQ
2155-304		PKS	329.68	-30.40	1.88±0.17	18.8±2.9	16.2±0.2	Y	HBL
2200+420		BL Lac	330.60	42.29	1.72±0.18	20.3±3.2	14.6±0.4	Y	LBL
2206+650	?		331.60	66.05	2.37±0.25	25.9±5.2		N	FSRS
2209+236		PKS	332.41	24.03	2.31±0.32	13.3±4.2		N	FSRQ
2230+114		CTA 102	338.11	11.80	2.46±0.13	19.0±2.8	13±1	Y	FSRQ(HP)
2250+1926	?		343.99	19.73	1.87±0.43	62.2±22.2		N	FSRQ

Continued on Next Page...

Table 3.2 Continued

Source	**"?"**	**Other names**	**RA** [a]	**DEC** [a]	**Spectral index** [b]	**Flux >100 Mev**[c]	**Log(ν_{sync})** [d]	**Mult. Obs**	**Class**[f]
2251+158		3C 454.3	343.51	16.02	2.22±0.06	56.5±4.0	13.5±0.5	Y	FSRQ(HP)
2255-282		PKS	344.52	-27.97	1.69±0.18[e]	12.8±2.8	12.7±0.3	N	FSRQ(HP)
2320-035		PKS	350.41	-3.48	2.17±0.45	30.5±9.6		N	FSRQ
2346+385	?		358.10	37.88	2.70±0.33	35.5±10.2		N	FSRQ
2351+456			359.57	46.07	2.57±0.35	13.7±3.6		N	FSRQ
2356+196		OZ+193	359.99	20.70	2.24±0.33	8.5±2.8		N	FSRQ

[a]These are EGRET positions from the 3rd EGRET catalog [8]

[b]Photon index measured in the 30 MeV - 10 GeV energy range

[c]Flux is in units of 10^{-8} photons cm^{-2} s^{-1}

[d]$Log(\nu_{sync})$-Logarithm of the f0requency (in Hz) of the synchrotron peak. These have been obtained from the literature cited in §3.4.1

[e]Spectral index is during a flare. This was the only spectral index that could be calculated. The quoted flux is the average flux observed.

[f]Possible EGRET identification

[g]FSRQ: Flat spectrum Radio Quasar; LBL: Low frequency-peaked BL Lac object; HBL: High frequency-peaked BL Lac object; HP: High polarization; LP: Low polarization; FSRS: Flat spectrum Radio Source. Classifications are based on [67] and [27]

Table 3.3: Gamma-ray photon spectral index (30 MeV - 10 GeV) and flux (>100MeV) of blazars that were bright and were observed multiple times by EGRET. The corresponding plots of spectral index vs. flux are shown in Fig. 3.3.

Source	**Start Dates**	**Viewing Periods Pooled**	**Graph label** [a]	**Spectral Index**	Flux> 100 MeV	**Det.** σ
0208-512	09/05/91	9.1	9.1	1.49±0.30	39.4±13.4	4.2
	09/19/91	10.0	10.0	1.91±0.06	111.8±8.2	21.5
	05/08/93, 06/03/93	220.0, 224.0	2	2.13±0.21	57.4±10.8	7.8
	05/31/94, 07/12/94, 07/25/94	329.0, 335.0, 335.5	3	2.04±0.12	98.6±12.0	6.7
	01/10/95, 09/07/95	409.0, 428.0	4	2.32±0.13	75.0±9.8	4.6
	03/05/96	517.0	517.0	1.82±0.08	139.8±12.4	18.3
0219+428 (3C 66A)	11/28/91, 08/11/92, 08/12/92,	15.0, 36.0, 36.5,	12	1.88±0.21	14.7±3.5	4.9
	09/01/92, 02/25/93	39.0, 211.0				
	04/26/94	325.0	3	1.66±0.23	22.9±5.7	5.1
0430+2859	04/22/91, 04/28/91, 05/01/91,	0.2, 0.3, 0.4,	1	1.85±0.16	15.4±3.3	5.2
	05/04/91, 05/16/91, 06/08/91,	0.5, 1.0, 2.1,				
	11/28/91, 06/11/92, 08/11/92,	15.0, 31.0, 36.0,				
	08/12/92, 09/01/92	36.5, 39.0				
	12/01/93, 02/08/94, 02/15/94,	310.0, 321.1, 321.5,	3	1.65±0.26	25.8 ± 8.0	4.1
	04/26/94	325.0				
	02/28/95, 03/07/95, 05/23/95,	412.0, 413.0, 420.0,	4	2.44±0.22	37.6 ±7.8	5.8
	08/08/95, 08/22/95	426.0, 427.0				
0528+134	04/22/91	0.2	0.2	2.36±0.13	121.0±15.1	10.4
	04/28/91	0.3	0.3	2.41±0.14	173.8±21.3	11.0

Continued on Next Page...

Table 3.2 Continued

Source	**Start Dates**	**Viewing Periods Pooled**	**Graph label** [a]	**Spectral Index**	Flux> 100 MeV	**Det.** σ
	05/01/91	0.4	0.4	2.06±0.12	186.5±21.6	12.0
	05/04/91	0.5	0.5	2.46±0.13	132.0±20.1	8.5
	05/16/91	1.0	1.0	2.31±0.09	102.1±9.1	14.5
	06/08/91	2.1	2.1	2.36±0.25	68.7±13.1	6.2
	03/23/93	213.0	213.0	2.30±0.10	356.7±37.7	14.0
	12/01/93, 02/08/94, 02/15/94, 08/09/94	310.0, 321.1, 321.5, 337.0	3	2.48±0.18	44.0±7.4	6.3
	02/28/95, 03/07/95, 04/04/95, 05/09/95,	412.0, 413.0, 419.1, 419.5, 420.0, 426.0	4	2.44±0.07	100.4±7.4	17.3
	10/17/95, 07/30/96, 08/13/96, 08/20/96, 02/18/97	502.0, 526.0, 527.0, 528.0, 616.1	56	2.28±0.12	68.1±6.9	11.7
0537-441	07/26/91, 08/22/91, 12/27/91, 05/14/92	6.0,8.0,17.0, 29.0	1	2.64±0.23	18.0±4.3	5.1
	05/31/94, 07/12/94, 07/25/94	329.0, 335.0, 335.5	3	2.59±0.27	16.4±4.5	4.5
	01/10/95, 04/11/95	409.0, 415.0	4	2.16±0.17	57.3±9.1	9.3
0716+714	05/07/91, 01/10/92, 03/05/92, 06/11/92	0.6, 18.0, 22.0, 31.0	1	2.31±0.20	22.4±3.9	7.3
	04/06/93, 04/06/93, 07/13/93	216.0, 227.0, 228.0	2	2.07±0.23	13.8±3.4	5.0
	03/01/94, 02/21/95	411.1, 411.5	4	2.47±0.28	26.7±6.4	5.4
	04/03/96, 09/06/96	518.5, 530.0	5	1.81±0.26	25.4±5.2	6.2
0827+343 (OJ 248)	09/17/92	40.0	1	2.13±0.28	22.0±5.4	5.2
	11/09/94	403.5	4	2.22±0.25	70.6±14.7	7.1
0917+449	05/07/91, 06/28/91, 01/10/92, 09/17/92	0.6, 4.0, 18.0, 40.0	1	1.97±0.25	14.0±3.2	5.5

Continued on Next Page...

Table 3.2 Continued

Source	**Start Dates**	**Viewing Periods Pooled**	**Graph label** [a]	**Spectral Index**	Flux> 100 MeV	**Det.** σ
	04/06/93, 04/20/93, 05/24/93, 06/29/93, 07/13/93	216.0, 218.0, 222.0, 227.0, 228.0	2	1.98±0.36	11.2±3.40	4.1
	04/05/94, 05/10/94	322.0, 326.0	3	2.19±0.24	20.8±5.1	5.5
0954+556 (4C 55.17)	05/07/91, 06/28/91, 01/10/92, 09/17/92	0.6, 4.0, 18.0, 40.0	1	2.32±0.37	6.50±2.5	3.1
	04/06/93, 04/20/93, 05/24/93, 06/29/93, 07/13/93	216.0, 218.0, 222.0, 227.0, 228.0	2	1.87±0.29	8.4±2.4	4.1
	03/01/94, 03/15/94, 04/05/94 05/10/94	319.0, 319.5, 322.0, 326.0	3	1.75±0.28	18.3±5.0	4.8
1101+384 (Mrk 421)	05/07/91, 06/28/91, 09/17/92	0.6, 4.0, 40.0	1	1.67±0.2	17.7±3.2	7.2
	04/20/93, 05/24/93, 06/29/93, 07/13/93	218.0, 222.0, 227.0, 228.0	2	1.83±0.29	12.4±3.5	4.6
	05/10/94	326.0	326.0	1.51±0.26	24.5±6.7	5.3
1156+295	01/05/93	206.0	206.0	1.98±0.41	166.9±41.4	6.8
	11/09/93, 11/16/93	307.0,308.0	v+307[b]	1.67±0.35	44.7±14.4	4.1
	04/25/95	418.0	418.0	1.78±0.24	45.4±10.8	6.3
	03/20/98	715.5	715.5	2.44±0.43	76.0±22.9	5.1
1219+285 (ON 231)	06/15/91, 06/28/91, 10/03/91, 12/22/92, 12/29/92, 01/05/93, 04/20/93, 05/24/93	3.0, 4.0, 11.0, 204.0, 205.0, 206.0, 218.0, 222.0	12	1.18±0.35	5.7±2.2	3.0
	10/19/93, 10/25/93, 11/02/93, 11/09/93, 11/16/93, 11/23/93,	304.0, 305.0, 306.0, 307.0, 308.0, 308.6,	3	2.2±0.21	17.2±3.5	6.1

Continued on Next Page...

Table 3.2 Continued

Source	**Start Dates**	**Viewing Periods Pooled**	**Graph label** [a]	**Spectral Index**	Flux> 100 MeV	**Det.** σ
	12/13/93, 12/17/93, 12/20/93, 12/27/93, 04/05/94, 05/10/94	311.0, 311.6, 312.0, 313.0, 322.0, 326.0				
	12/13/94, 04/25/95	406.0, 418.0	4	1.76±0.29	35.0±9.4	4.9
1222+216 (4C 21.35)	12/22/92, 12/29/92, 01/05/93,	204.0, 205.0, 206.0,	2	2.54±0.24	26.5±6.0	5.7
	04/20/93, 05/24/93	218.0, 222.0				
	10/19/93, 10/25/93, 11/02/93, 11/09/93, 11/16/93, 11/23/93, 12/13/93, 12/17/93, 12/20/93, 12/27/93, 04/05/94, 05/10/94	304.0, 305.0, 306.0, 307.0, 308.0, 308.6, 311.0, 311.6, 312.0, 313.0, 322.0, 326.0	3	1.94±0.16	14.9±2.8	6.8
1226+023 (3C 273)	06/15/91, 10/03/91	3.0, 11.0	1	2.45±0.25	11.2±3.0	4.3
	10/19/93, 10/25/93, 11/02/93, 11/09/93, 11/16/93, 11/23/93, 12/13/93, 12/17/93, 12/20/93, 12/27/93, 04/05/94, 05/10/94	304.0, 305.0, 306.0, 307.0, 308.0, 308.6, 311.0, 311.6, 312.0, 313.0, 322.0, 326.0	3	2.62±0.12	29.7±3.7	10.6
	11/29/94, 12/13/94, 12/20/94 01/03/95	405.0, 406.0, 407.0, 408.0	4	2.73±0.2	13.4±4.0	4.0
	01/16/96	511.0	511.0	2.24±0.26	32.8±7.5	5.8
	12/30/96, 01/07/97	609.0, 610.0	6a	2.60±0.19	127.1±20.7	9.2
	12/10/96, 12/17/96, 12/23/96, 01/14/97, 01/21/97	606.0, 607.0, 608.0, 610.5, 611.1	6b	2.66±0.23	50.2±10.2	6.60
1253-055 (3C 279)	06/15/91	3.0	3.0	1.78±0.04	249.5±10.7	37.1
	10/03/91	11.0	11.0	1.88±0.08	81.5±7.6	15.2

Continued on Next Page...

Table 3.2 Continued

Source	**Start Dates**	**Viewing Periods Pooled**	**Graph label** [a]	**Spectral Index**	Flux> 100 MeV	**Det.** σ
	10/19/93, 10/25/93, 11/02/93,	304.0, 305.0, 306.0,	3	2.34±0.10	46.9±5.10	12.5
	11/09/93, 11/16/93, 11/23/93,	307.0, 308.0, 308.6,				
	12/13/93, 12/17/93, 12/20/93,	311.0, 311.6, 312.0,				
	12/27/93, 04/05/94, 05/10/94	313.0, 322.0, 326.0				
	11/29/94, 12/13/94, 12/20/94	405.0, 406.0, 407.0	4	2.19±0.12	27.6±3.8	9.2
	01/16/96	511.0	511.0	1.89±0.11	125.7±15.6	10.4
	01/30/96	511.5	511.5	1.92±0.06	558.6±34.5	27.6
	12/10/96, 12/17/96, 12/23/96,	606.0, 607.0, 608.0,	6	1.88±0.22	18.3±4.1	5.1
	12/30/96, 01/07/97, 01/14/97	609.0, 610.0, 610.5				
	01/21/97, 06/17/97	611.0, 621.5				
	01/19/99	806.5	806.5	1.76±0.21	189.2±24.8	9.6
	02/08/00	910.0	910.0	2.09±0.13	169.2±22.10	11.8
	02/23/00	911.1	911.1	1.87±0.24	134.7±29.2	7.0
1406-076	04/09/92	24.5	24.5	1.98±0.28	95.4±23.8	5.5
	12/22/92	204.0	204.0	2.13±0.29	69.7±17.8	5.5
	12/29/92	205.0	205.0	1.76±0.17	134.7±24.3	8.5
	01/05/93	206.0	206.0	1.86±0.27	95.1±23.1	6.1
	01/12/93	207.0	207.0	2.15±0.17	115.1±14.7	11.5
1611+343 (OS +319)	11/17/92, 11/24/92	201.0, 202.0	2	2.28±0.18	45.4±8.1	7.7
	11/01/94	403.0	4	2.12±0.23	73.5±16.6	6.3
	03/21/96, 04/23/96, 04/09/97	516.5, 519.0, 617.8	56	2.10±0.29	19.1±5.3	4.6
1622-253	07/12/91, 12/12/91, 04/28/92,	5.0, 16.0, 27.0	1	2.03±0.18	21.2±5.3	4.4
	09/09/93, 03/22/94, 04/19/94,	302.3, 323.0, 324.0,	3	2.07±0.26	39.5±8.9	4.5
	07/18/94, 08/04/94, 09/20/94	334.0, 336.5, 339.0				

Continued on Next Page...

Table 3.2 Continued

Source	**Start Dates**	**Viewing Periods Pooled**	**Graph label** [a]	**Spectral Index**	Flux> 100 MeV	**Det.** σ
	06/06/95, 06/13/95, 06/20/95, 06/30/95	421.0, 422.0, 423.0, 423.5	4	2.26±0.18	67.10±11.10	7.9
1622-297	06/06/95	421.0	421.0	2.42±0.15	228.6±34.30	9.3
	06/13/95	422.0	422.0	2.22±0.11	313.6±33.50	14.3
	06/20/95	423.0	423.0	2.18±0.12	281.0±35.7	11.2
	06/30/95	423.5	423.5	2.17±0.09	228.1±22.7	14.9
	03/18/96	516.1	516.1	1.51±0.27	184.2±50.2	5.3
	08/27/96	529.5	529.5	2.41±0.27	123.6±30.6	5.3
	08/05/97	625.0	625.0	2.31±0.42	81.8±33.1	3.3
1633+382 (4C +38.41)	09/12/91	9.2	1	2.02±0.08	109.1±9.5	17.8
	11/17/92, 11/24/92	201.0, 202.0	2	2.39±0.25	34.4±7.1	6.4
	03/21/96, 04/23/96, 04/09/97	516.5, 519.0, 617.8	56	2.36±0.8	18.9±4.9	4.7
1730-130 (NRAO 530)	07/12/91, 08/15/91, 10/31/91	5.0, 7.2, 13.1	1	2.27±0.32	19.40±4.9	4.4
	12/12/91, 02/06/92,	16.0, 20.0				
	02/22/93, 03/29/93, 05/05/93	210.0, 214.0, 219.0	2	2.58±0.32	35.0±8.6	4.6
	05/31/93, 06/19/93, 08/03/93	223.0, 226.0, 231.0				
	08/10/93, 08/12/93, 08/24/93	229.0, 229.5, 232.0				
	09/09/93, 03/22/94, 04/19/94	302.3, 323.0, 324.0	3	2.53±0.18	35.1±5.9	6.8
	06/10/94, 06/18/94, 07/18/94	330.0, 332.0, 334.0				
	06/06/95, 06/13/95, 06/20/95	421.0, 422.0, 423.0	4	2.33±0.22	34.1±3.3	6.0
	06/30/95, 09/20/95	423.5, 429.0				
1830-210	07/12/91, 08/15/91, 10/31/91, 12/12/91, 02/06/92	5.0, 7.2, 13.1, 16.0, 20.0	1	2.52±0.26	24.2±5.6	4.6

Continued on Next Page...

Table 3.2 Continued

Source	**Start Dates**	**Viewing Periods Pooled**	**Graph label** [a]	**Spectral Index**	Flux> 100 MeV	**Det.** σ
	02/22/93, 03/29/93,	210.0, 214.0,	2	2.33±0.33	39.2±10.2	4.3
	05/31/93, 06/19/93, 08/03/93	223.0, 226.0, 231.0				
	08/10/93, 08/12/93, 08/24/93	229.0, 229.5, 232.0				
	09/09/93, 03/22/94, 04/19/94	302.3, 323.0, 324.0	3	2.44±0.22	24.3±5.8	4.6
	06/10/94, 06/18/94, 07/18/94	330.0, 332.0, 334.0				
2155-304	11/15/94	404.0	404.0	1.82±0.23	30.5±7.8	5.9
	02/06/96, 05/21/96	513.0, 520.4	56	1.61±0.41	18.9±6.0	4.1
	11/11/97, 11/18/97	701.0,702.0	v+701.0 [b]	2.27±0.38	67.7.0±19.7	4.9
2200+420	01/24/95	410.0	410.0	2.35±0.34	32.2±10.10	4.0
(BL Lac)						
	07/15/97	623.5	623.5	1.76±0.15	148.4±21.7	10.2
2230+114	01/23/92, 04/23/92, 05/07/92,	19.0, 26.0, 28.0,	1	2.30±0.17	27.60±4.60	7.9
(CTA 102)						
	08/20/92	37.0				
	03/08/94, 05/17/94, 08/01/94	320.0, 327.0, 336.0	3	2.73±0.29	16.8±5.5	3.3
2251+158	01/23/92	19.0	19.0	2.20±0.10	83.1±8.9	13.5
(3C 454.3)						
	08/20/92	37.0	37.0	2.19±0.15	125.1±19.0	10.0
	03/08/94, 05/17/94, 08/01/94	320.0, 327.0, 336.0	3	2.26±0.19	32.1±6.8	5.9
	01/24/95	410.0	4	2.19±0.12	51.2±6.8	10.9

Table 3.4: Spectral Variability results. Columns 3, 4 & 5 are results from the χ^2 test and column 5 lists the correlation coefficient between gamma-ray spectral index and Flux ($> 100\ MeV$). The coefficient is negative when the spectral index (positive) hardens with increasing flux.

Source	**Mean ± Stdev** $(\Gamma_\mu \pm \sigma)$	χ^2_{red}	**DOF**[b]	**Conf.(%) lev.**[a]	**Pearson's Corr. Coeff**[b]
0208-512	1.95±0.28	2.93	5	99	+0.10
0219+428 (3C 66A)	1.77±0.16	0.50	1	52	[a]
0430+2859	1.98±0.41	3.32	2	97	+0.62
0528+134	2.36±0.12	1.10	9	62	-0.34
0537-441	2.46±0.26	2.04	2	87	-0.99
0716+714	2.17±0.29	1.25	3	71	+0.21
0827+243 (OJ 248)	2.17±0.06	0.06	1	19	[a]
0917+499	2.05±0.12	0.24	2	21	+0.95
0954+556 (4C 55.17)	1.98±0.3	0.83	2	56	-0.77
1101+384 (Mrk 421)	1.67±0.16	0.34	2	28	-0.99
1156+295	1.97±0.34	0.85	3	53	+0.28
1219+285 (ON 231)	1.71±0.51	3.86	2	98	+0.46
1222+216 (4C 21.35)	2.24±0.42	5.07	1	98	[a]
1226+023 (3C 273)	2.55±0.17	0.60	5	31	+0.11
1253-055 (3C 279)	1.98±0.18	3.9	9	100	-0.32
1406-076	1.98±0.17	0.79	4	46	-0.54
1611+343 (OS+319)	2.16±0.10	0.24	2	22	+0.08
1622-253	2.12±0.12	0.44	2	36	+0.97
1622-297	2.17±0.31	1.63	6	87	-0.07
1633+382 (4C+38.41)	2.25±0.20	4.59	2	99	-0.97

Continued on Next Page...

Table 3.2 Continued

Source	**Mean ± Stdev** $(\Gamma_\mu \pm \sigma)$	χ^2_{red}	**DOF**[b]	**Conf.(%) lev.**[a]	**Pearson's Corr. Coeff**[b]
1730-130 (NRAO 530)	2.42±0.16	0.47	4	24	-0.05
1830-210	2.43±0.10	0.1	2	10	-0.91
2155-304	1.88±0.30	0.78	2	54	+0.99
2200+420 (BL Lac)	1.94±0.25	1.75	1	81	
2230+114 (CTA 102)	2.51±0.30	2.15	1	86	
2251+158 (3C 454.3)	2.22±0.03	0.04	3	1	-0.69

[a]Correlation coefficient was not determined since the sample size was less than 3

[b]The DOF (degrees of freedom) is for the χ^2 test of variability and is one less than the sample size.

3.4.2 Spectral variability with Flux

3.4.2.1 Long term spectral variability

We searched for variability in the spectral index of all the blazars (for which two or more spectral indices could be calculated) using the χ^2 test and the results are listed in Table 3.4. Column 2 contains the sample mean (Γ_μ) and the standard deviation of the mean (σ) for each blazar. The χ^2_{red} value obtained from fitting the sample of spectral indices with a line of constant mean Γ_μ is listed in column 3. Column 4 lists the degrees of freedom (DOF) (which is one less than the sample size), while column 5 contains the confidence level for the presence of spectral variability. We do not detect any statistical evidence for spectral variability in 16 of the 26 blazars. The confidence levels for the presence of spectral variability are low ($<$ 80%), mostly due to the large error bars on the spectral indices.

We looked for spectral variability correlated with flux using the Pearson's correlation coefficient. The correlation coefficient is listed in column 5 of Table 3.4. The coefficient, which could be calculated only in cases where there were three or more observations, is negative when the spectral index (positive) hardens with increasing flux. The dependence of spectral index on flux is not uniform across all the blazars. The index hardens with increasing flux in some cases, softens in others, and in the rest does not vary with flux. Using a cutoff of 0.8 for the correlation coefficient, we found the spectral index to be correlated with flux in 10 of the 26 blazars (including those with two observations where there was visual evidence). The spectrum hardened with increasing flux in 6 of them while the spectrum softened in the remaining 4. Only five sources satisfied both the spectral variability and the index-flux correlation criteria: PKS 0537-441, 1222+216 (4C 21.35), PKS 1633+382 (4C+38.41), 2200+420 (BL Lac) and 2230+114. We discuss some individual sources below.

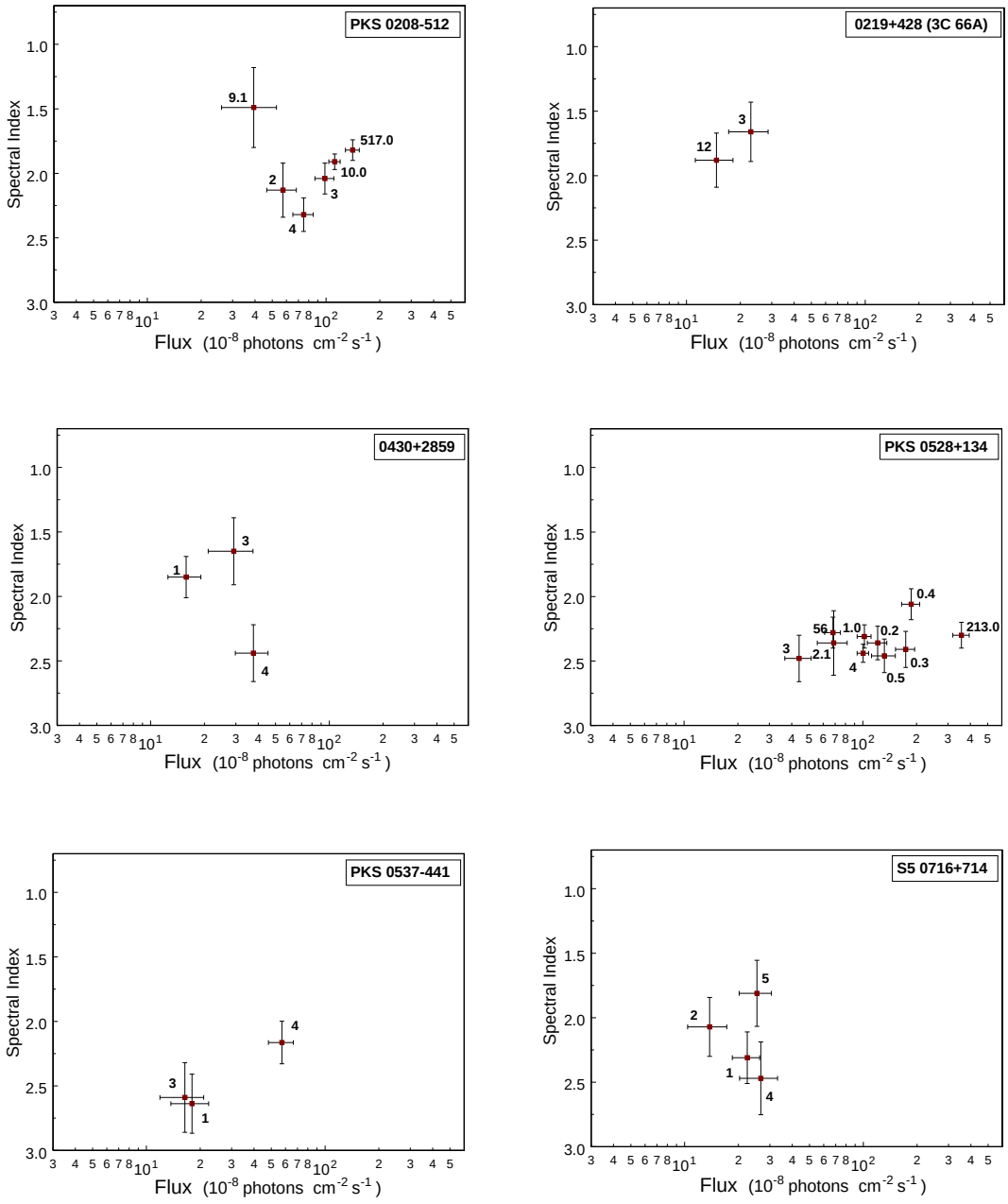

Figure 3.3: Variation of photon spectral index in the 30 MeV-10 GeV energy range with gamma-ray flux (>100 MeV) in units of 10^{-8} photons cm^{-2} s^{-1}. The spectral index is obtained from observations that are either one viewing period long (labeled by decimal numbers), or a combination of the viewing periods during one or more Cycle of observations (labeled by integers that show the Cycle(s) being combined). The details of the viewing periods/Cycles used in the analysis are given in Table 3.3.

1253-055 (3C 279): This object shows spectral variability at a confidence level of 99.99% and shows marginal evidence for hardening with increase in flux. The spectral states at a flux $> 70 \times 10^{-8}$ photons cm^{-2} s^{-1} span more than 85% of the range of fluxes observed. These states do not show any overall trend in the spectral index vs. flux space (correlation coefficient of 0.05) and do not show any significant evidence for spectral variability (confidence level of 58%). The quiescent states from Cycles 3 and 4 have a softer spectral index when compared with the average value of 1.96 while the quiescent state from Cycle 6 has a harder spectral index.

PKS 0208-512: We do not see any overall trend for this source, in spite of a strong evidence for spectral variability (confidence of 98%). However, the spectral index does show evidence of hardening with increasing flux (correlation coefficient of -0.95) at fluxes higher than 60×10^{-8} photons cm^{-2} s^{-1}. A similar trend was also observed in this source by [62] who combined simultaneous data from the Compton Telescope (COMPTEL; 0.75-30 MeV) and EGRET. They obtained a correlation coefficient of -0.78 between the spectral index in the 0.75 MeV - 10 GeV range and the flux (>100 MeV) recorded in the EGRET energy range.

We observe a softening in the spectral index (coefficient of +0.95) as the flux increases, at fluxes lower than 80×10^{-8} units. There is an indication of this effect at lower fluxes in [62, see Figure 4], but the large error bars do not justify a separate fit. Moreover, PKS 0208-512 has been categorized as an "MeV-blazar" and the spectrum from these sources shows a break between 1-20 MeV [24, 81, 82, 83]. Hence, a single power law does not adequately describe the entire energy range form 0.75 MeV-10 GeV. Flux anti-correlations between COMPTEL and EGRET could also be expected for MeV-blazars (observed in case of PKS 0528+134, also a possible MeV blazar; [83]). But a reanalysis of the 1993 COMPTEL data by [62] lowered the significance of the only detection of this source in the MeV energy range, with no detections in its many subsequent observations. Consequently, the association

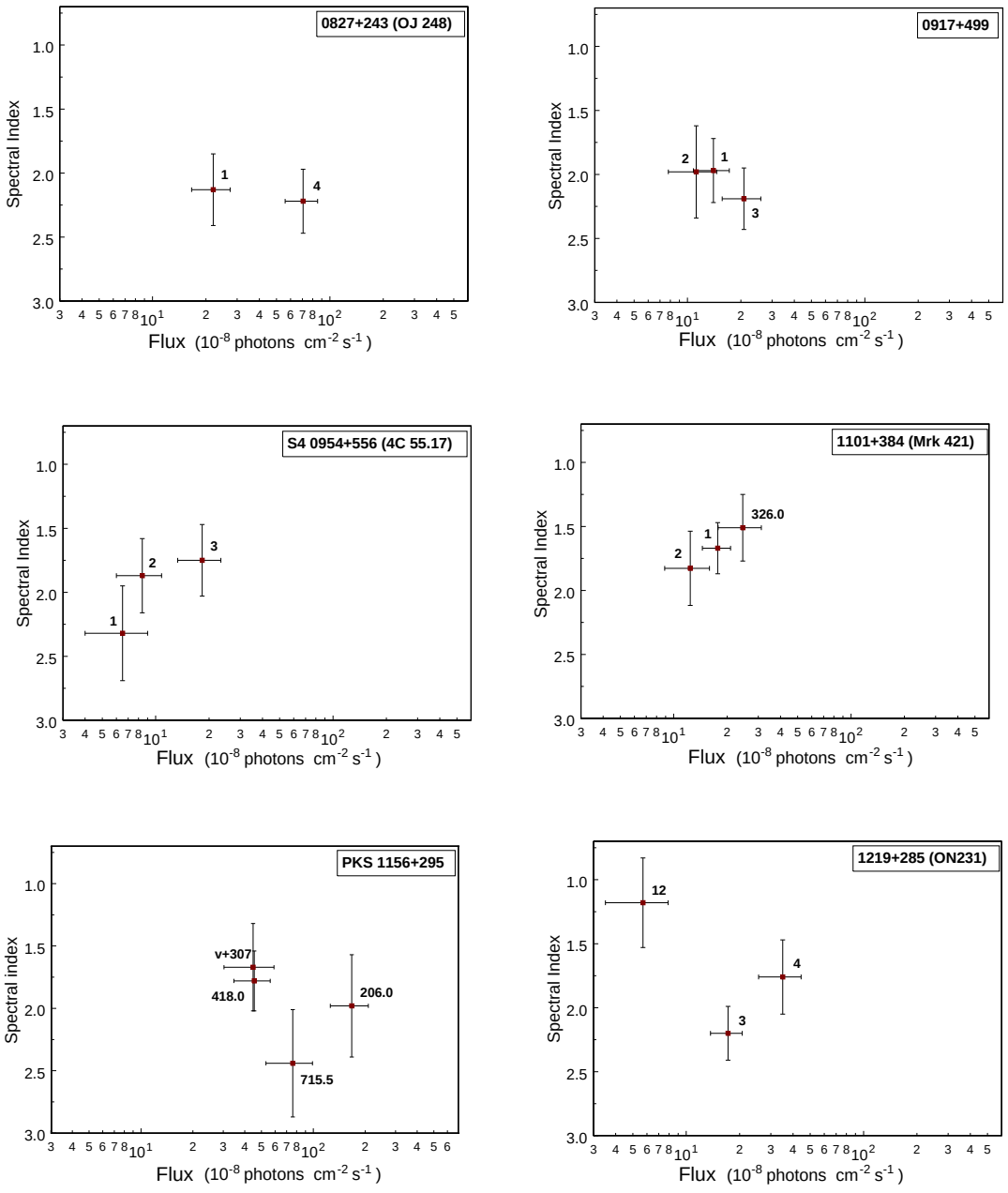

Figure 3.4: *Spectral index Vs Flux Continued*

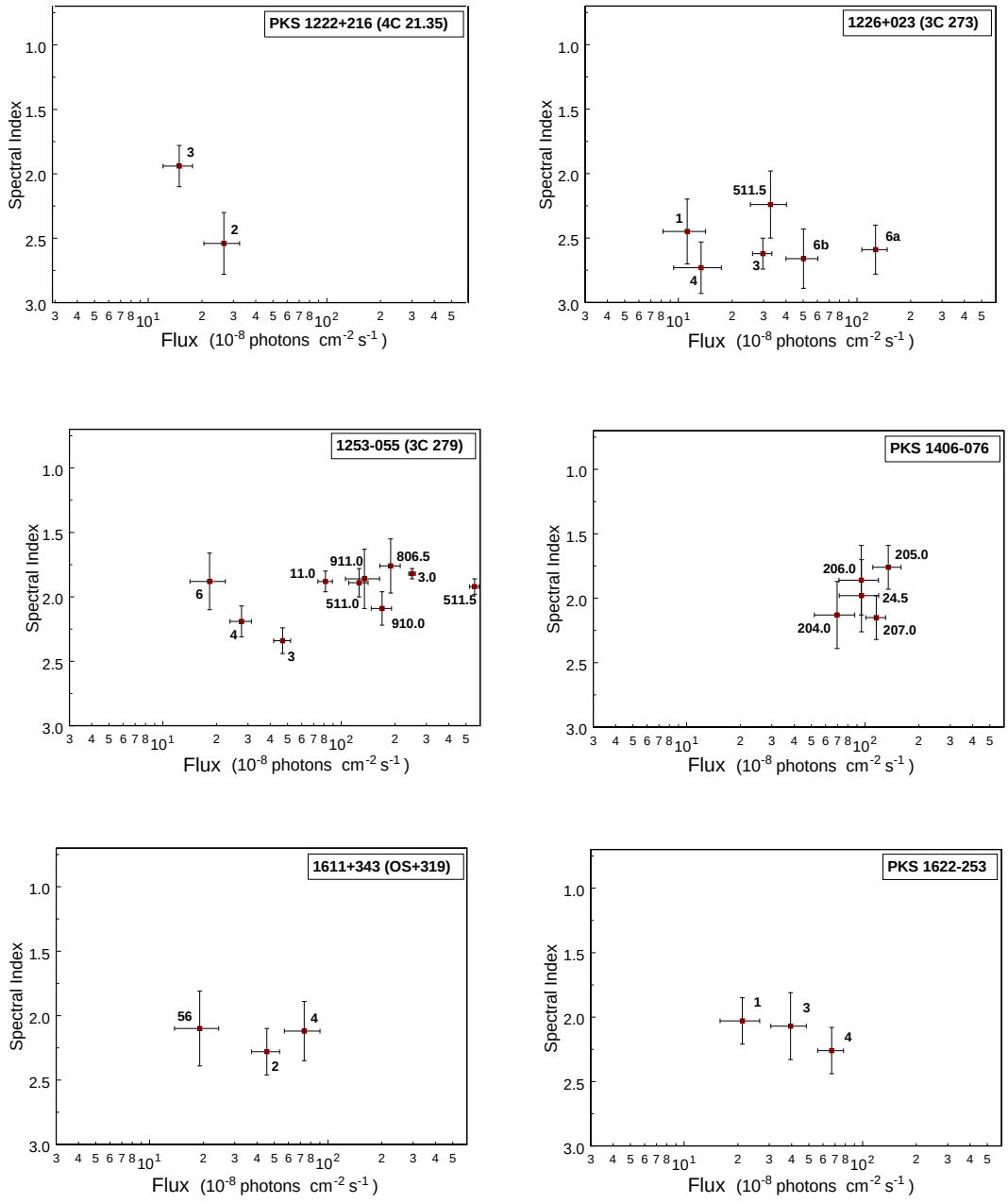

Figure 3.5: *Spectral index Vs Flux Continued*

of PKS 0208-512 with MeV-blazars is questionable. But the unique nature of the spectral dependence on flux (initial softening and subsequent hardening) in the EGRET energy range, makes this strong gamma-ray source an interesting candidate for future observations.

PKS 0528+134: Previously published results for this object [50] showed a correlation of -0.85 between spectral index and flux using data from viewing periods 0.2-0.5 (combined), 1.0, and 213.0. The same combination of viewing periods using recalibrated data did not show any evidence of spectral hardening. Inclusion of data through viewing period 420.0 decreased the correlation to -0.5 [66]. We obtained a correlation coefficient -0.5 for the complete data which included observations from Cycles 5 and 6. The large error bars yield a low confidence of spectral variability of 67% despite a spread in the values.

PKS 0537-441, PKS 1633+382 (4C+38.41): Spectral indices for these objects harden with increasing flux (correlation coefficients of -0.97 & 0.99) and show spectral variability at a confidence of 87% and 98% respectively.

2200+420 (BL Lac) & 2230+114 (CTA 102): The spectrum hardens with increasing flux in these sources. The correlation coefficient was not calculated in these cases as there were only two observations.

Some of the FSRQs and LBLs show spectra that appear to soften with increasing flux. This can be seen in PKS 1222+216 (4C 21.35), PKS 1219+285 (ON 231), and, also in PKS 0208-512 and S5 0716+714 at low fluxes.

HBLS; 1101+384 (Mrk 421) & PKS 2155-304: The spectral index for Mrk 421 hardens as flux increases with a coefficient of -0.997. PKS 2155-304, however, shows a softening in spectral index with increasing flux (correlation coefficient of +0.99). This seems to be in contradiction to standard scenario wherein the gamma-ray emission from HBLs is from SSC mechanism [84, 85]. HBLs are not very bright

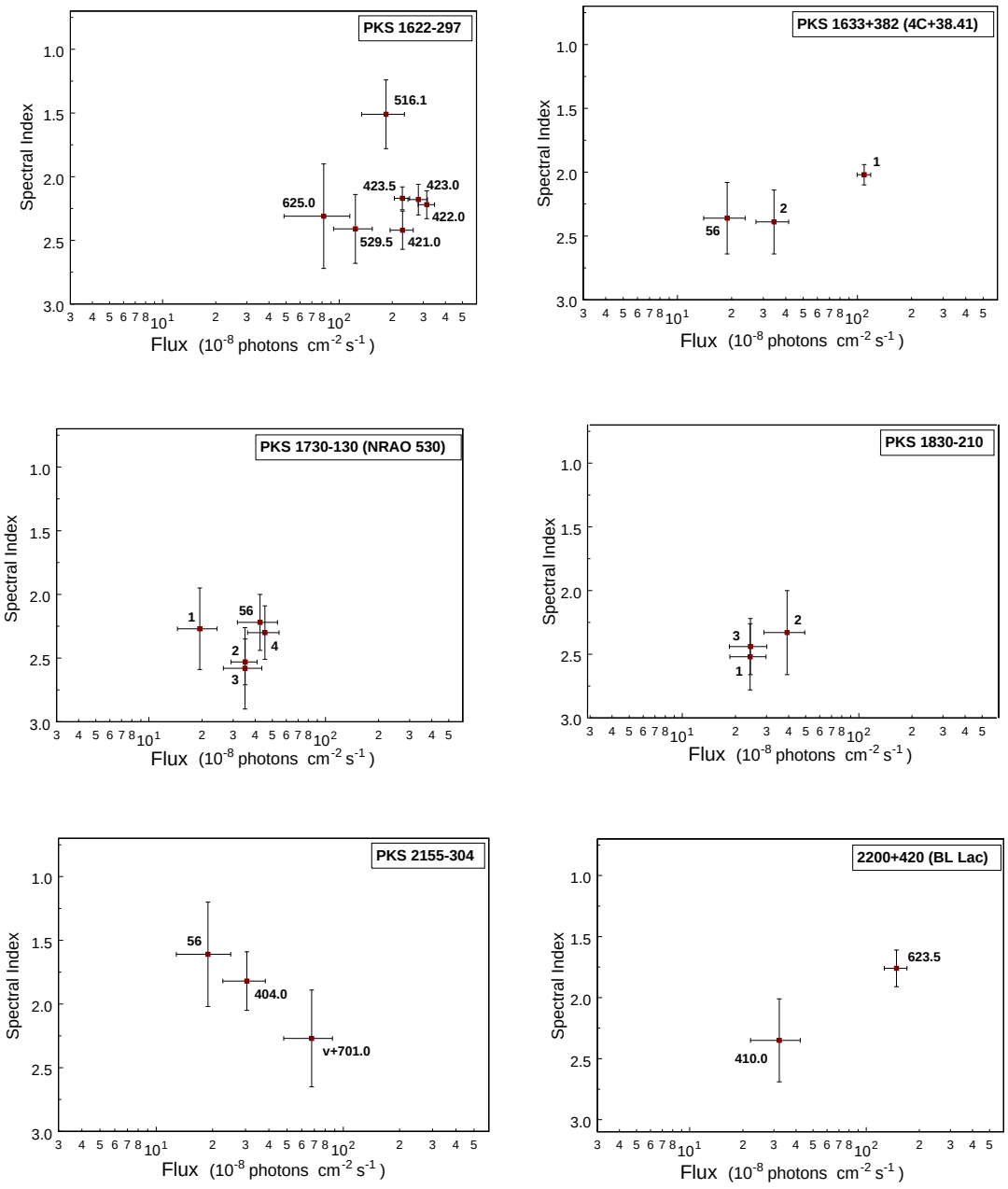

Figure 3.6: *Spectral index Vs Flux Continued*

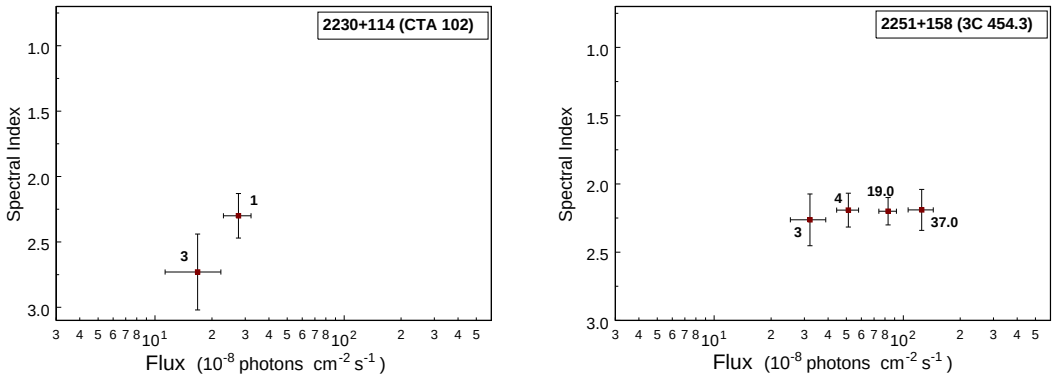

Figure 3.7: *Spectral index Vs Flux Continued*

at EGRET energies and some of the spectral states show deviations from a simple power-law fit. Consequently, the error bars on the spectral indices are large and the confidence level of spectral variability from the χ^2 test is low.

3.4.2.2 Short term spectral variability: *Spectral hysteresis during a flare*

Blazars vary on multiple timescales. The smallest timescale of resolution (based on the light curves) for a gamma-ray flares is about $\sim 3-8$ hours [52, 86]. A study of spectral hysteresis (in relation to flux) during flares provides crucial insights into factors related to the comoving electron dynamics (electron acceleration and cooling) [87, 85, 84]. Since we have extracted spectral indices from data accumulated over a complete viewing period (usually 7 days long), we cannot track spectral changes during a flare. Some of the sources, however, were observed for more than 2 consecutive viewing periods when they were flaring, either because the observations were planned a priori, or because the schedule was changed to track the flare. The flux history in such cases could show an event occurring at larger timescales. Figure 3.8 shows the light curve and spectral index vs. flux plots of the flare for the three sources for which we had data from four contiguous viewing periods. We discuss

the individual sources below.

PKS 1622-297: This source was observed from June 6, 1995 (VP 421.0) until July 7, 1995 (VP 423.5) for 4 consecutive viewing periods when it underwent a large flare. [52] split the observations into 10 unequal intervals with the size of the intervals ranging from 1 day to 10 days, A plot between flux in the two intervals- 100 MeV-300 MeV (x) and $>$ 300 MeV (y) showed a clockwise progression in time. Previously published spectral index values [36] for the four viewing periods during this flare show evidence for spectral variability at a confidence level of 97% (χ^2 of 9.81 with 3 degrees of freedom) but a large fraction (68%) of χ^2 was due to the hard spectral index of 1.72$\pm$0.15 during viewing period 422.0, which recorded the largest flux. We obtained a spectral index of 2.22$\pm$0.11 for this viewing period with the recalibrated maps. A χ^2 test yielded confidence level of 51%, with most of the contribution from viewing period 421.0. The spectral indices trace out a counterclockwise loop (as time progresses) in the spectral index-flux space. PKS 1406-076: Four out of the five points for this object are from 4 consecutive viewing periods from December 22, 1992 (VP 204.0) till February 2, 1993 (VP 207.0). While the light curve shows two successive flares, the large error bars on the spectral indices reduce the variability in spectral index to a confidence of 62%. The spectral indices show a counterclockwise progression during the period.

PKS 0528+134: Observations of this object in April-May 1991 spanned 36 days. The source was observed from April 4, 1991 to May 4, 1991 and then for 2 weeks from May 16, 1991, and a week from June 6, 1991. These points are marked with their viewing-periods number (0.2-0.5, 1.0 & 2.1) in Figure 3.3. The χ^2 test shows spectral variability at a confidence level of 73%, which is the largest among the three sources. The light curve in Figure 3.8 shows the contiguous viewing periods 0.2-0.5 to be a part of a single event and the spectral index traces out an intertwined loop in counterclockwise direction as in the other cases.

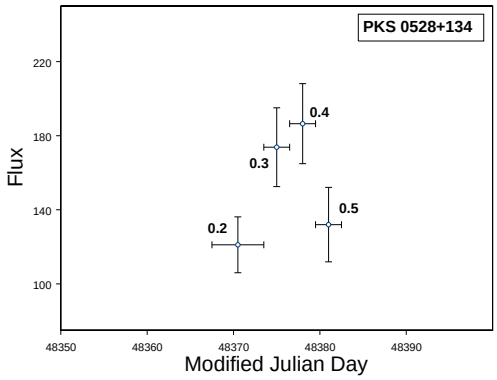

(a) Light Curve- Slow rise and fast decay

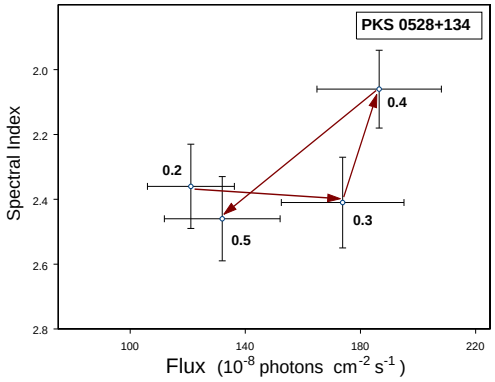

(b) Hysteresis Plot

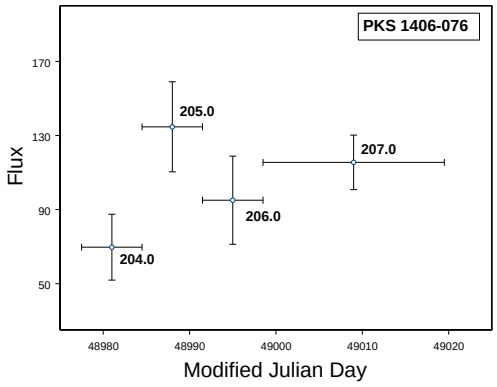

(c) Light Curve- Uniform Rise and Uniform Decay

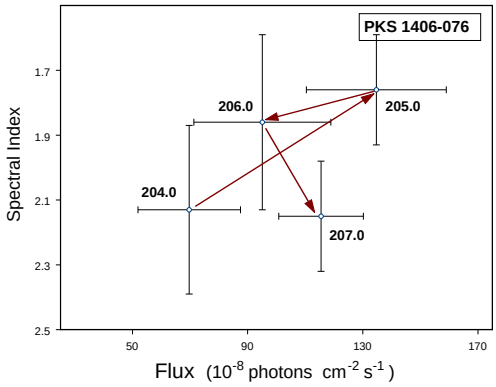

(d) Hysteresis Plot

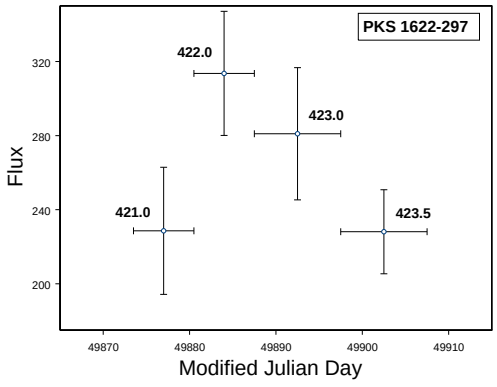

(e) Light Curve- Fast Rise and Slow Decay

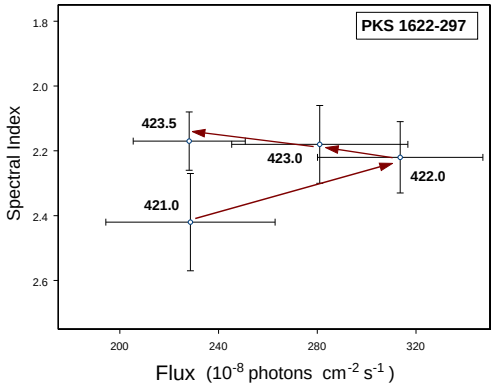

(f) Hysteresis Plot

Figure 3.8: Spectral hysteresis during blazar flares that lasted 3∼4 weeks. Graphs on the left show the variability of flux $> 100MeV$ in units of 10^{-8} photons cm^{-2} sec^{-1} with time (in MJD). The ranges for the time-axis and the flux axis are set to 50 days and 150 units respectively. The graphs on the right show hysteresis in the photon spectral index vs. flux space. The arrows show a chronological progression.

Spectral hysteresis is a commonly observed phenomenon in HBLs at X-ray wavelengths. It has been reported at multiple timescales ranging from hours [88, 89, 90] to seconds [91] indicating the presence of scale invariance in the spectral evolution at X-ray wavelengths. We have observed hysteresis at weekly timescales in all the three FSRQs for which data from at least 4 contiguous viewing periods was available. This effect has previously never been observed in FSRQs in gamma-rays at these timescales. The light curve in Figure 3.8 shows completely different flare profiles for the 3 blazars. The flare in PKS 0528+134 is a combination of a slow rising phase accompanied by a faster decaying phase while the profile in PKS 1622-297 is exactly the opposite with a fast rise and a comparatively slower decay. The light curve in the case of PKS 1406-076 shows multiple events- a flare consisting of a uniform rise and decay, and a second flare that was partially captured. Although the flux profiles are quite different, all the three sources show a counterclockwise rotation in the spectral index vs. flux space as time progresses.

3.5 Discussion

Under a leptonic jet paradigm, the broadband spectral energy distribution of blazars is modeled by considering synchrotron and inverse Compton emission from a blob of e^+e^- plasma moving relativistically along the jet axis. The seed photons for the inverse Compton process could come from the jet (SSC), the accretion disk (ECD), the broad line region clouds (ECC) or the infra-red dust in the surrounding torus ERC(IR) (see §3.1 for the references for various emission mechanisms).

3.5.1 Spectral variability in FSRQs and LBLs

External-Compton process appears to play an important role in FSRQs and LBLs [27]. In a broadband spectral energy distribution, the peak emission frequency

for ERC(IR), ECD and ECC processes increases in that order. The latter two have their peak frequency in the EGRET energy range and affect spectral variations in a more direct way. However, not all FSRQs have a strong infra-red component since it depends on the size of the torus and the density of the circum-nuclear dust. The inverse Compton component due to SSC emission does not have a pronounced peak. The plateau of the SSC emission extends from hard X-rays (few hundred keV) to the GeV gamma-ray region.

When the source is in a low-intermediate state, emission from the SSC process is at least as important as that from the three ERC processes, and the photon spectrum could be hard or soft, based on relative fraction of flux from these processes. Model fits to the broadband spectrum from 3C 279 by [38] & [68] and PKS 0528+134 by [66] show that moderate-large flares require a greater contribution from the ERC processes and have a higher bulk Lorentz factor Γ for the particles.

As the source undergoes a flare, the energy density of the IR field and the broad line field (BEL), both of which are proportional to Γ^2 [24] as measured in the comoving frame of the plasma, also increase. The flares might also be related to the injection of energetic particles near the base of the jet, where the external radiation fields have a higher density than further out. Consequently, the contribution of external Compton process increases. Although emission from all processes increases, the ECD and ECC processes affect the EGRET energy range more. However, the extent of contribution from the ERC(IR) process, whose peak lies below the EGRET energy range [25], could be one of the factors that determines how soft the EGRET spectrum is during the low-intermediate states as it affects the lower energies of the EGRET range. Broadband fits for 3C 279 from various epochs in [38, fig. 2] show the low-intermediate states (Cycle 3, 4 & 6 in our Figure 3.3) to have comparable fluxes from SSC, ECD, and ECC processes, with the EGRET data lying on the falling portion of the SSC emission plateau. The 0.3-30 MeV region, which is just

below EGRET energy-range, shows a significant excess (in the broadband fits for Cycles 3 and 4) that could be caused by the ERC(IR) process (not included in the model). Hence the resultant EGRET spectra are soft. The enhanced MeV emission could also explain the softening in the spectral index seen from low to intermediate fluxes in PKS 0208-512, which has been categorized as an "MeV-blazar" [81, 82] and more recently questioned by [62]. The existence of MeV-blazars as a separate class has been disputed due of the dearth of sources. However the Swift Burst Alert Telescope has recently detected bright emission, and rapid variability at short timescales (down to 1-2 ks) from the optically faint quasar J0746 in the 15-195 keV range leading to the inclusion of this blazar in the MeV-blazar class [92].

While the ERC(IR) process could play an important role during the low-intermediate states, there is a substantial increase in emission from the ECD and ECC process during large flares, as shown in the case of 3C 279 by [38]. The EGRET spectrum during these flares is hard or soft based on the relative contribution from these two processes. Since the IR emitting region is very large and far away, the ERC(IR) process does not vary over timescales as short as those of the other two process and does not play a significant role in the spectral variations seen at short time scales during flares that typically last a few days.

SPECTRAL HYSTERESIS: The three sources (PKS 1622-297, PKS 0528+134, PKS 1406-076) that were observed for an extended time during flares, show evidence of counterclockwise spectral hysteresis. A possible explanation for this may be the emergence of an external Compton component near the onset of the flare, where an ERC component at MeV-GeV energies might be dominant. As the flare evolves and the emission region moves out, the intrinsically harder SSC radiation might take over (as it takes time $\sim$ R/c for the internal radiation field to build up), leading to hardening of the spectrum as the flux is already decreasing. This would work in situations in which the acceleration time scale is shorter than the cooling time scale,

and the cooling time scale is of the order of the dynamical time scale, R/c.

3.5.2 Spectral variability in HBLs- a possible external component?

Inverse Compton emission in the case of HBLs is usually attributed to the SSC mechanism. The EGRET energy range lies on the rising portion the inverse Compton bump for Mrk 421. As the source undergoes a flare, the maximum flux at the peak increases, leading to increased contribution at higher frequencies on the low energy tail of the inverse Compton bump causing the spectra to harden. In PKS 2155-304, however, we observed the opposite trend of spectrum softening with increasing flux. This is in contradiction with the standard SSC interpretation [87, 85, 84]. The soft spectral index (2.22±0.46) is from the flare in November 1997 (viewing period 701.0 in Figure 3.3). In a broadband distribution (plot of νF_ν vs ν), a photon spectral index of 2 is a horizontal line. The rising portion of inverse-Compton peak has a spectral index less than 2 while the decreasing portion of the synchrotron peak would have a photon spectral index of greater than 2. If the frequency range of observations is close to the frequency where these two branches meet, it is possible for the synchrotron branch to move in to the observed energy range during flares leading to a spectral index that is higher than 2.0. But the EGRET energy range is quite far from where the two branches meet in case of PKS 2155-304 [72, see fig. 7]. Extending the synchrotron emission up to EGRET energies would come close to the theoretical limit for synchrotron emission from leptons for Doppler factors usually seen in such sources. The observed trend in PKS 2155-304 could be an indication for a quasi- external Compton component expected from a decelerating-jet model [93], where synchrotron emission from a previous, slower component may provide an additional target photon field for Compton scattering. Alternatively, this could be a signature of proton synchrotron emission in a hybrid leptonic/hadronic model [30] since one would expect that there might be a non-negligible proton fraction present

in the jet.

While the varying dominance of ERC components (or an absence thereof) can explain some of the gamma-ray spectral variability observed so far, it is just one of the many possible scenarios. Gamma-ray spectral variability could arise out of a combination of factors that are both internal and external to the plasma. The internal factors affect the two energy cutoffs of the particle injection spectrum, the injection spectral index, the injection energy, the magnetic field, the bulk Lorentz factor of plasma and the particle density. The external factors are: the energy density of the infra-red field due to the dusty torus, the energy density of the broad emission line region, and the level of accretion disk activity. The current gamma-ray data, however, do not allow us to effectively explore the large parameter space as the error bars on the spectral indices are usually high. This is due to the limitations of EGRET's sensitivity. The Gamma-ray Large Area Space telescope (GLAST)[a] with a higher sensitivity and greater duty cycle of coverage for individual sources should be able to determine spectral indices more accurately. In addition to the large number of parameters that go into the jet models, the long integration times of EGRET imply that we are averaging over substantial and completely arbitrary sections of individual outbursts, or adding contributions from multiple smaller outbursts. A study of spectral hysteresis during individual flares could indicate if we are dealing with global, structural changes (including, e.g., a change of the bulk Lorentz factor), or with factors related to the co-moving electron dynamics (electron acceleration/cooling) [87, 85, 84]. The EGRET data do not allow us to study spectral evolution during a flare. This would be an area of study ideal for GLAST.

[a] http://glast.gsfc.nasa.gov

3.5.3 Blazars as a source of extragalactic gamma-ray background

Stecker *et al.* [65] postulated that the *entire* diffuse extragalactic gamma-ray background (EGRB) can be attributed to emission from unresolved blazars, based on two factors: (1) The spectral index for diffuse gamma-ray background is 2.10 ± 0.03 [64], which is quite close to the previously published value of the average spectral index (2.15 ± 0.04) for all observed blazars [36] and (2) The preliminary concave shape of the extragalactic gamma-ray background, determined prior to 1995, could be well fitted by the diffuse emission calculated from the blazar luminosity function [65, Figure 3]. However, the EGRB spectrum published in [64] shows deviations from a power law index of 2.1±0.03 at low and high energies. The curvature is less prominent but it cannot be ruled out. In addition, the flare-state spectra had to be harder than the quiescent state spectra for a good fit[65, Figure 3] .

We obtained a value of 2.25±0.03 (2.22±0.03 for FSRQ+LBL+HBL) for the average spectral index of all the blazars observed by EGRET and a median value of 2.25. 64 of the blazars have spectral indices ≥2.1 while 33 of them have spectral indices that were lower.

A more current background spectrum generated using the finalized EGRET data from Cycles 1-4, based on a model different than that used in [64], was published by [94] and is shown in Figure 3.9. The broadband spectrum from 30 MeV -50 GeV shows a clear break at 2 GeV. The spectrum is steeper than the spectrum in [64] at energies below 2 GeV. The spectrum has a concave curvature due to the break and the rise beyond 10 GeV. Although the whole range from 30 MeV -50 GeV shows substantial deviations from a power law fit, we find that the points below 2 GeV can be fitted well with a power law of slope 2.24±0.01 and a correlation coefficient of 0.99. The slope is very close to our value for the average blazar spectral index of 2.25±0.03 (superposed in Figure 3.9).

As we noted earlier, if the EGRB has to be entirely due to blazars, then

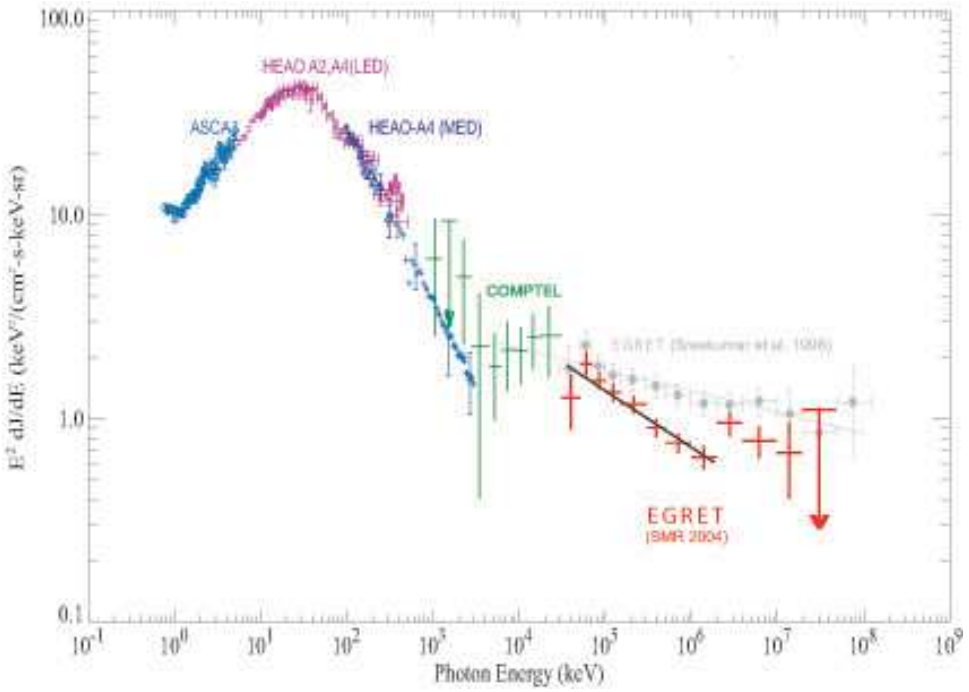

Figure 3.9: The X-ray and Gamma-ray background broadband spectrum. The data are taken from [94]. The extragalactic gamma-ray background (EGRB) calculated from the recalibrated EGRET data by [94] (labeled SMR 2004) shows a break at 2 GeV and is steeper than the spectrum calculated by [64] in the energy range 30 Mev - 2 GeV. We were able to fit the points below 2 GeV with a power law of index 2.24±0.01, which is very close to the average blazar spectral index of 2.25±0.03 obtained with the recalibrated EGRET data.

the flare-state spectra must be harder than the quiescent state spectra to produce concave shape in the diffuse background spectrum [65]. We did not observe any strong evidence for the flaring states to have a harder spectrum in case of the well-observed blazars. The spectrum hardened with increasing flux in some of them while it softened in some others. For some blazars, both trends were observed. Consequently, any discussion of blazars as sole contributors to diffuse extragalactic background depends on the similarity of the blazar spectrum to that of the EGRB. The proximity of two indices below 2 GeV certainly makes blazars a prime candidate for contributing to the diffuse background.

The current blazar data shows some deviations from power law during flares in some cases, but at energies below 2 GeV. However the data do not have enough

statistics to attempt a detailed analysis using broken power law models. Although the blazar spectrum cannot be measured accurately above 2 GeV due to EGRET's limited sensitivity there is no a priori reason to expect a sharp break in the blazar spectrum at 2 GeV along with an increasing contribution at energies higher. This suggests the necessity of an increased contribution by other sources to the extra-galactic gamma-ray background at higher energies. The current estimates for blazar contribution to the diffuse background emission range from nearly 100% [65] to 25% [95, 96]. GLAST, with its higher sensitivity and larger energy range (up to 100 GeV) would be able to measure the diffuse background more accurately and help narrow down the class of sources contributing to it.

3.6 Conclusions

We analyzed all nine years of EGRET data for blazars and noted the following.

1. The sample contained 98 sources: 66 FSRQs, 17 LBLs, 4 HBLs, 10 FSR sources and 1 radio galaxy. We obtained a mean spectral index of 2.26±0.03 for FSRQs, 2.14±0.08 for LBLs, 1.68±0.09 for HBLs (spectral index could not be calculated for one of them), and 2.48± 0.1 for flat spectrum radio sources. The gamma-ray spectral index shows a transition from FRSQs to LBLs to HBLs with FSRQs having the softest spectral index and HBLs having the hardest.

2. We did not observe any clear correlation between the gamma-ray spectral index and flux. A majority of blazars did not show any overall trend. The spectra hardened with increasing flux in some, while it softened in some energy intervals for few others. For those blazars where the spectra varied and did not show an overall trend, the sample consisted of a mixture of hard and soft states.

3. We observed a previously unreported counterclockwise hysteresis at weekly timescales in the spectral index vs. flux space. The effect was consistently seen in the flare data from all the 3 FSRQs which were observed for at least 4 contiguous viewing periods during the flare. The flux profiles of these sources were very different from each other.

4. It is difficult to understand clearly and categorize the observed gamma-ray spectral variability (or a lack thereof) in blazars due to the large error bars on spectral indices and the long integration times needed to get the spectral information.

5. Gamma-ray spectral variability can arise out of a combination of several physical parameters that are both internal and external to the jet. The current data do not have the required energy and time resolution to narrow down the parameter-space used in the models due to EGRET's limitations. GLAST should be able to provide more accurate spectral information on shorter timescales.

6. It is reasonable to expect that there might be deviations from power law behavior in the gamma-ray photon spectrum, given the many possible types of emission mechanisms in blazars. There is some evidence of this in the EGRET data during large flares but insufficient statistics prevent a detailed analysis using broken power law models. This would be an ideal area for GLAST to study.

7. HBLs are faint at EGRET energies. This results in a low confidence of spectral variability even when there is a strong correlation between spectral index and flux. With the enhanced energy resolution and sensitivity of GLAST, as well as the new atmospheric Cherenkov telescopes (e.g. H.E.S.S., VERITAS, MAGIC

and CANGAROO), it should be possible to detect more HBLs at gamma-ray energies and determine their spectral indices more accurately.

8. We obtained a value of 2.25±0.03 for the average spectral index of all the blazars observed by EGRET. This is very close to the spectral index of 2.24±0.01 for the extragalactic gamma-ray background observed below 2 GeV which make blazars as one of the significant contributors to the EGRB. But the break in the broadband background spectrum at 2 GeV and a subsequent increase (>10 GeV) suggests the necessity of an increased contribution by other sources at higher energies.

We would like to thank Olaf Reimer and Andrew Strong for their inputs on the extragalactic gamma ray background and providing us with the data for Figure 3.9. G.N. would like to thank the Leon Herreid Foundation whose fellowship made a part of this research possible. G.N. would also like to thank Sangeeta Parashar for editing the manuscript.

Chapter 4

An Intriguing Convex Break in the EGRET SED of Mrk 421

This work was done in collaboration with the following people-

Dr. Keith M. Jahoda, Dr. R. C. Hartman, and Dr. Jean H. Swank from the NASA-Goddard Space Flight Center, Greenbelt Maryland

Dr. M. Georganopoulos, University of Maryland at Baltimore County, Baltimore

Dr. R. Mukherjee, Barnard College & Columbia University, New York

and has been submitted to the "The Astrophysical Journal".

4.1 Introduction

The broadband spectral energy distribution (SED) from high-frequency peaked BL Lac objects (HBLs) shows two bumps [13]. The peak at lower frequencies is in the X-ray region, and is widely believed to be due to synchrotron emission from relativistic electrons in the blobs of radiating plasma moving along the jet, away from the core of the active galactic nucleus (AGN). Under the scenario of "leptonic models", wherein the radiating plasma mainly consists of electron and positrons, the second bump is attributed to inverse-Compton (IC) scattering of photons that are generated from the synchrotron process itself as postulated by the synchrotron Self-Compton (SSC) models [15, 16, 17]. These models have had success in fitting simultaneous X-ray and TeV data in many states of activity [102]. However, model fits for HBLs published in the literature so far have had extremely sparse to almost no coverage in the EGRET energy range, which lies on the rising part of the inverse Compton bump that peaks at TeV energies. HBLs are faint at EGRET energies and individual observations are very often not statistically significant. It is expected

that the EGRET HBL spectrum is hard, with a photon index < 2.

However, in our studies, we find that *not all the available EGRET data for HBLs has been accounted for* in the different multiwavelength fits attempted so far in the literature. We have done a comprehensive analysis of the entire data set from the two HBLs, Mrk 421 and PKS 2155-304, that were observed by EGRET multiple times during its nine-year mission. We find that the results contradict the current assumptions about these sources. We describe the analysis in §4.2, and discuss possible scenarios that explain the intriguing HBL spectrum in Section §4.3.

4.2 Analysis and Results

Following the standard EGRET analysis method (e.g. [8] and [103]), we extracted the flux at energies >100 MeV, and determined the significance of detection (e.g. as defined in [47]) for the HBLs studied in this work. Table 4.1 presents our results for the different viewing periods (VPs) during which the sources Mrk 421 and PKS 2155-304 were detected. In some cases, temporally close VPs were combined: e.g. V+322.0 (322.0+326.0), V+227.0 (227.0+228.0) to get a stronger significance. Column 5 in Table 1 gives the power-law photon spectral index obtained over the energy range 30 MeV-10 GeV, determined over four to ten energy intervals depending upon the strength of the detection.

Figure 4.1 shows the light curve for the entire EGRET mission and the νF_ν spectra for Mrk 421. Immediately apparent is the wide difference in the spectral states, also quantified by the range of spectral indices observed (Table 4.1). The photon index ranges from a hard value of 1.2±0.27 (during V+322.0) to a soft value of 2.68±0.39 (V+227.0). The former shows a rising spectrum (Fig.4.1-A4) which is consistent with what is believed about these sources so far. However, the falling trend in the latter spectrum (Fig.4.1-A3) is unexpected for HBLs.

Even more interesting is the difference between the spectra of VP 4.0 (Fig.4.1-

Table 4.1. Details of HBL observations by EGRET.

Source VP[a]	(RA, Dec) MJD Range	Flux[b]	$\sqrt{(TS)}$[c]	Gamma[d]
Mrk 421	(166.10, 38.15)			
0.6	48383.7-386.8	19.7±11.3	2.2	···
4.0	48435.8-449.7	15.6±3.8	5.4	2.07±0.28
40.0	48882.7-903.6	21.6±6.9	4.0	2.01±0.34
V+218.0	49097.6-138.6	11.2±4.5	3.0	···
218.0+	49097.6-112.6			
222.0	49131.7-138.6			
V+227.0	49167.6-195.5	15.1±5.9	3.4	2.68±0.39
322.0	49447.6-461.6	8.6±3.6	3.0	
326.0	49482.7-489.6	24.4±6.7	5.3	1.47±0.29
V+322.0	49447.6-489.6	13.7±3.3	5.5	1.20±0.27
PKS 2155-304	(329.68, -30.40)			
209.0	49027.8-040.7	15.1±6.9	2.8	···
404.0	49671.7-685.6	30.6±7.7	5.9	1.83±0.23
V+513.0	50119.6-231.6	18.3±6	4.0	1.51±0.40
513.0	50119.6-126.6			
520.4	50224.6-231.6			
V+701.0	50763.6-777.6	67.7±19.9	4.9	2.35±0.35
V+708.0	50812.6-826.6	30.7±30.7	2.9	1.73±0.49

[a]Viewing periods. V+ indicates a combination of two temporally close viewing periods within the range of dates mentioned. See [8] and [103] for details.

[b]Flux > 100 MeV, in units of 10^{-8} ph cm^{-2} sec^{-1}

[c]Significance of detection (See [47] for definition)

[d]Photon Spectral Index (30 MeV-10 GeV)

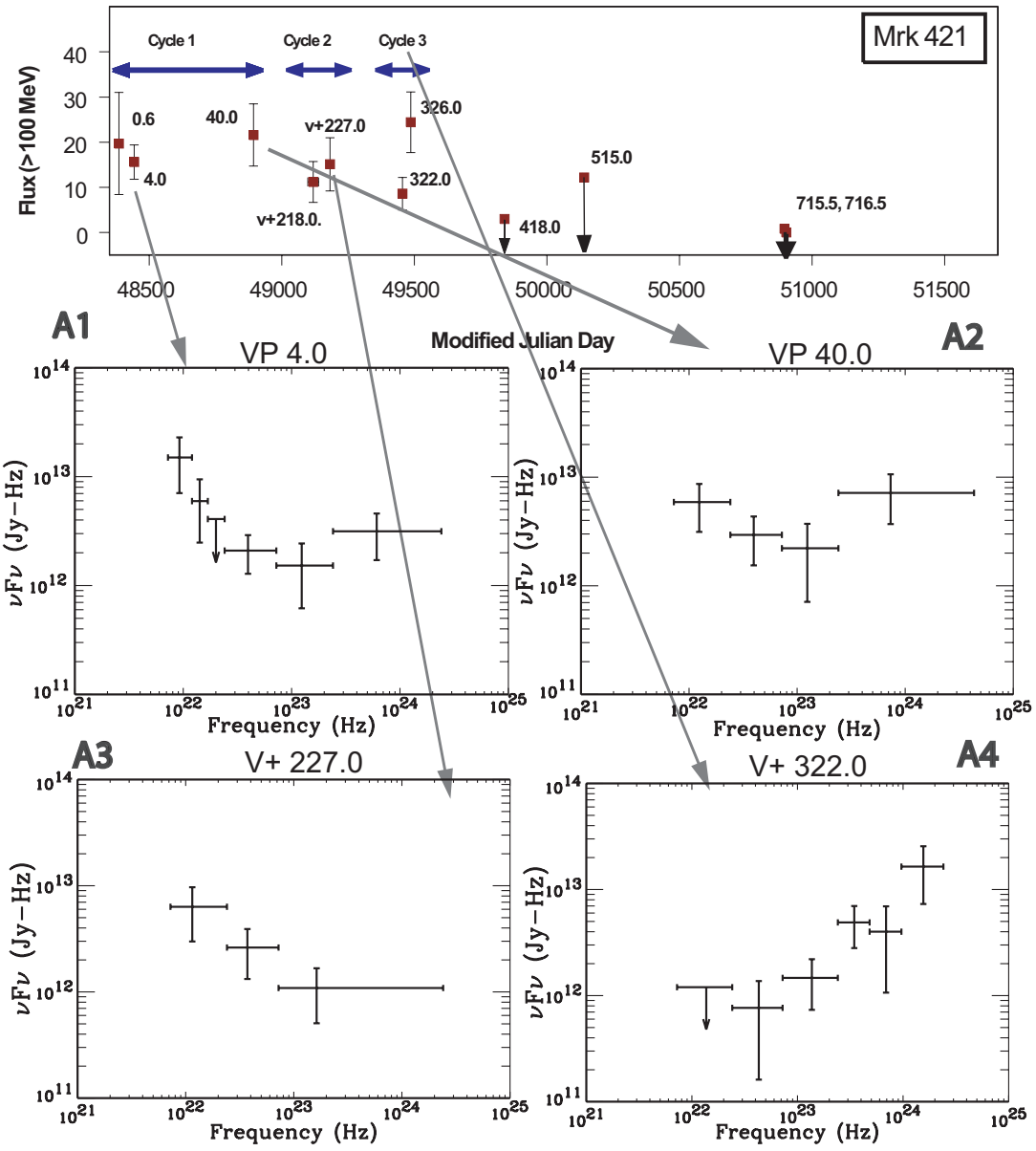

Figure 4.1: EGRET light curve (top figure) and individual spectra for Mrk 421. A wide range of spectral indices can be observed.

A1) and V+322.0 (A4). The fluxes recorded during these two sets of observations, both $\sim 5.4\sigma$ detections (see Table 4.1), are similar within the error bars, but the νF_ν spectra look very different. In order to get a statistical perspective on how different these spectra are, we performed a series of fits by varying the two free parameters, power-law normalization and spectral index, and plotted the chi-squared values of the fit. The substantial regions of non-overlap in the chi-squared confidence contours (for 1, 2 and 3 σ levels) in Figure 4.4 illustrate that these spectra are indeed different in spite of the fairly large error bars on the data points. The fitted values lie just outside the 99% contours of each other. Although the best fit value (2.07 ± 0.28) for VP 4.0 is very close to 2.0, a horizontal line in a νF_ν spectrum, the first five points seem to have a significantly steeper spectrum. The asymmetric shape of the contours around the fitted values also confirmed the preference for softer spectra. We performed a spectral fit for the first five points and obtained a spectral index of 3.18 ± 0.45 and the chi-squared contours for this fit have a very small overlap with those for observations during V+322.0. The curvature introduced in the spectrum by the last data point in Fig.4.1-A1 suggests the possibility of a convex break, which is a realistic possibility, if a "completely" soft (V+227.0 in A3) and a completely hard (V+322.0 in A4) spectrum coexist in the same energy range. We fit the entire spectrum with a broken power-law by fixing the break energy at the best fit value of 243 MeV, and obtained an F-test probability of 96% for the broken power law being a better fit than the single power law. The indices before and after the convex break were 3.5 and 1.46 respectively.

The spectrum observed during VP 40.0 (Fig. 4.1-A2) is also consistent with this picture. However, the best fit is a horizontal line with spectral index of 2.01 ± 0.34, and the small number of points does not warrant a broken power law fit. The combined spectrum for Mrk 421 in Cycle 1, detected at a significance of 7.2 σ, makes a stronger case for a convex break, and is shown in Fig. 4.3. We fit the spectrum

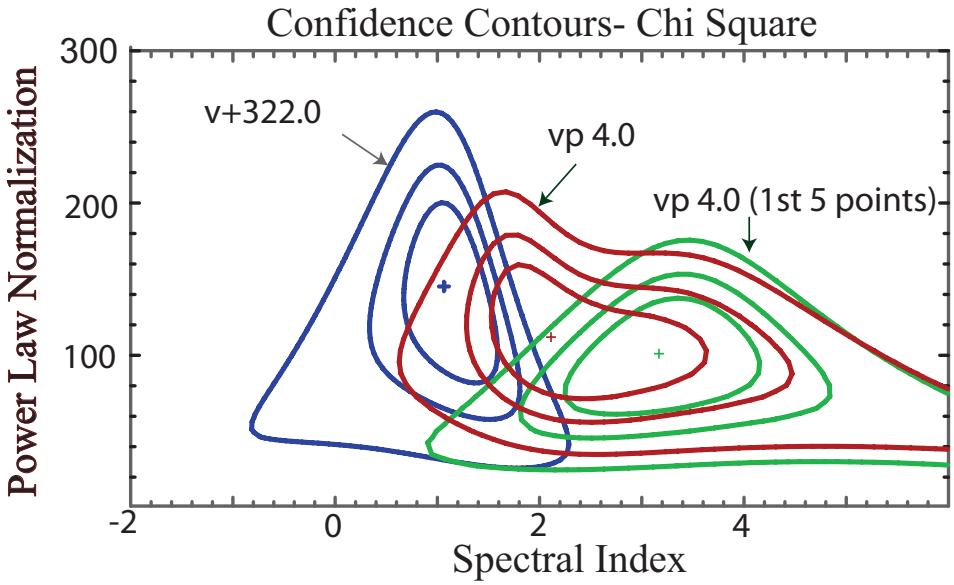

Figure 4.2: 1, 2 and 3 σ Chi-squared confidence contours for power-law fits to spectrum from a hard state (V+322.0) and a soft state (VP 4.0). First 5 points in VP 4.0 are better fit with a steeper index.

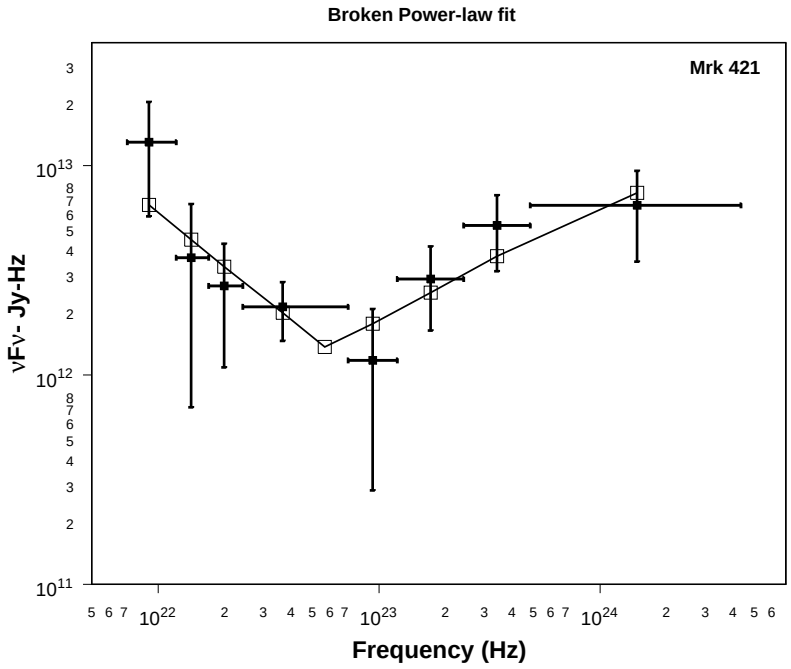

Figure 4.3: A broken power law fit to the convex spectrum during Cycle 1 (a 7.2 σ detection). The indices before and after the break energy (fixed) of 235 MeV are 2.89± 0.43 and 1.46±0.18 respectively.

with a broken power-law with the break energy fixed at its best value of 235 MeV, and obtained values of 2.89± 0.43 and 1.46±0.18 for the spectral indices below and above the break energy. The F-test probability for the presence of a convex break is 96.7%.

4.2.1 The Multiwavelength Picture

Figure 4.5 shows the broadband SED for Mrk 421 for the EGRET data from Cycle 1, for the hardest (V+322.0), and for the softest (VP 4.0) spectral states. The Whipple data (100 GeV-10 TeV) are taken from [102] while the STACEE data (130 GeV- 1 TeV) are from [104]. We obtained the BEPPOSAX X-ray data from the mission website: http://www.asdc.asi.it, and the INTEGRAL spectrum has been taken from the active state of Mrk 421 shown in [105]. We also analyzed all the available data from the PCA instrument on the Rossi X-ray Timing Explorer (RXTE), and extracted the spectra (3-20 keV) from the highest and the lowest states recorded during the period 1996-2005. As the X-ray flux increases from the lowest state, the spectral index hardens and the synchrotron peak moves to higher energies. The spectrum from the HEXTE instrument (also on RXTE), extending up to 100 keV during the highest PCA state is also shown. However, the HEXTE data points are slightly below those of PCA in the overlapping energy interval due to a difference in the relative normalizations. This increases the perceived curvature at higher energies. The spectra from the All Sky Monitor (ASM; 2-10 keV, on board RXTE) shown in the figure are from the peak state of a day scale light curve labeled as "ASM-day". The "ASM-ind" denote the spectra from individual dwells corresponding to the peak-flux (which has large error bars) and the individual dwell with the highest significance during the same day. The highest ASM state shows an increasing trend, albeit with large error bars on the lowest two points.

The hard EGRET state (V+322.0) shown in the figure is consistent with the

EGRET data lying on the increasing phase of the inverse-Compton bump. However, in order to connect the spectrum from the soft state during VP 4.0 to any of the TeV states shown, one would need a convex break at higher EGRET energies. Similarly, the rising part (at higher EGRET energies) of the convex spectrum from Cycle 1 connects smoothly to the TeV data, but the soft spectrum at lower energies is unexpected for HBLs and challenges our current understanding of these sources.

The scenario in case of PKS 2155-304 is a little different. There is no direct evidence of a convex break in the spectrum. The two states VP 404.0 and V+ 701.0, detected at $\sim$5 σ and above, had one hard and one soft (compared to a value of 2.0) spectral index respectively (see Table 4.1). The latter was from a flare in Nov. 1997, the *SED from which was never published*. We combined all the EGRET data from PKS 2155-304 to see if the anomalous contribution (from the point of view of current models) of the flare disappears. The resultant detection has a significance of 8.0 σ and the spectrum has a power law index of 2.07$\pm$0.15. However, the spectrum (in Figure 4.6) is not a power-law, but instead shows a convex curvature (similar to but not as prominent as the Cycle 1 spectrum of Mrk 421). The TeV data are from the Cerenkov telescope H.E.S.S. [106].

In order to verify that this convex spectrum is not an artifact of the analysis or characteristic of all gamma-ray blazars, we also looked at the aggregated spectra for 48 other sources that were detected at a significance $>$ 3.0 σ. The only source (of the 48) that showed a convex curvature was PKS 2005-489 (detected at 3.0 σ), also an HBL like Mrk421 and PKS 2155-304.

4.3 Discussion and Conclusions

Mrk 421 definitely shows a convex break in the Cycle 1 time-averaged spectrum and has indications of the same during several different individual epochs. The spectrum has statistically different hard and soft states during its multiple detec-

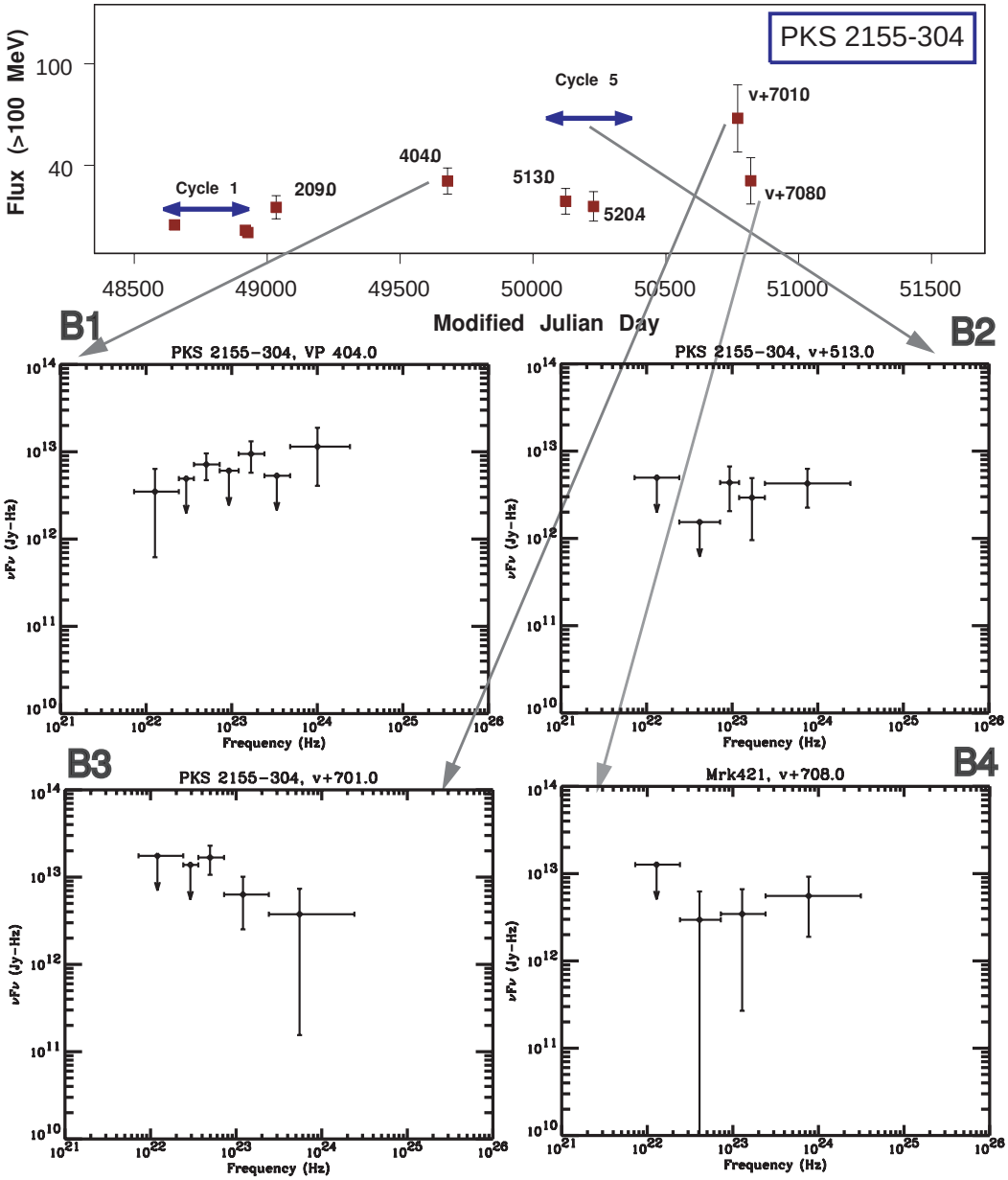

Figure 4.4: EGRET mission light curve for PKS 2155-304 and broadband spectra

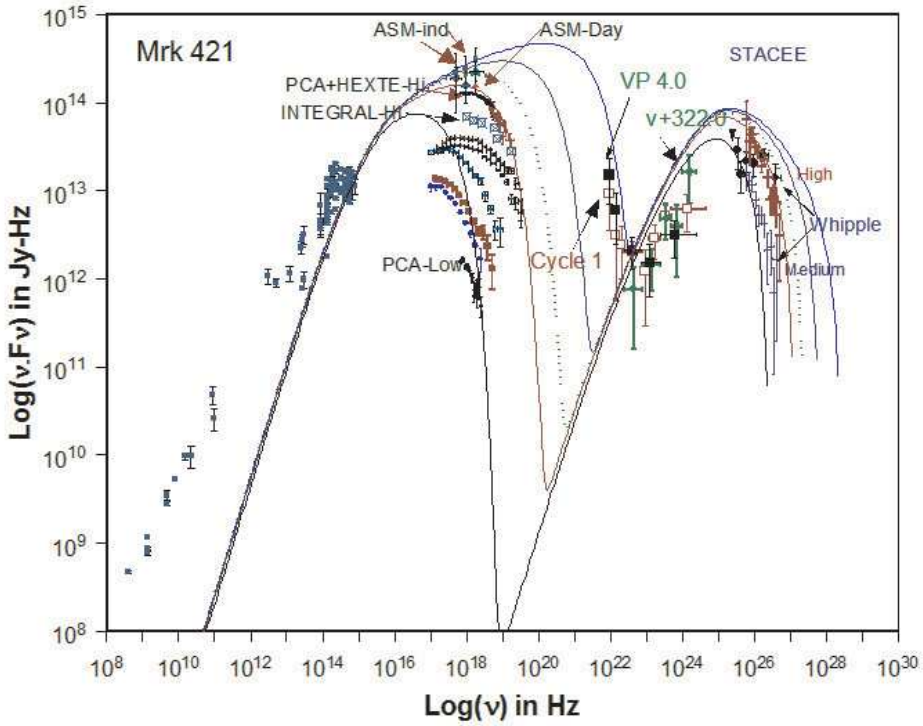

Figure 4.5: Multiwavelength SED for Mrk421. Solid curves for Mrk 421, depict model SEDs of increasing values of $\eta = 3.4 \times 10^5,\ 1.4 \times 10^4,\ 3.4 \times 10^3,\ 5.4 \times 10^2,\ 34$, for a homogeneous source of radius $R = 10^{16}$ cm and $\delta = 10$, permeated by a magnetic field $B = 0.5$ G.

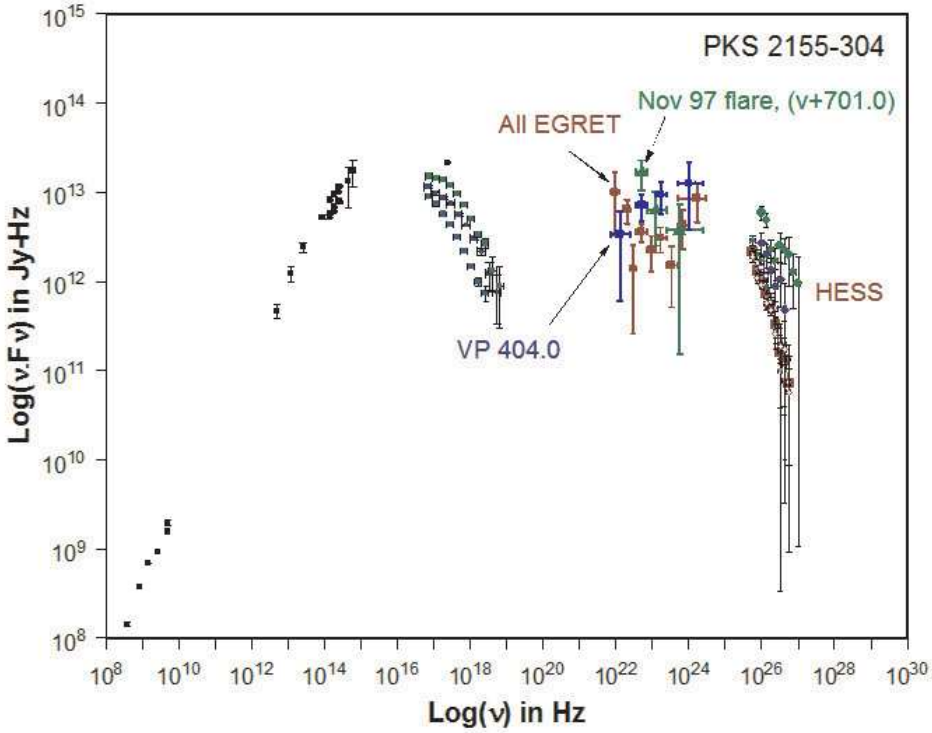

Figure 4.6: Multiwavelength SED for PKS 2155-304.

tions. PKS 2155-304 also shows a convex curvature in a nine-year combined EGRET spectrum. This is certainly perplexing from the point of view of leptonic models.

A possible way to explain the convex SED of Mrk 421 is through a third spectral component that would peak at $\nu \sim 10^{21-22}$ Hz ($\epsilon \sim 10 - 100$, where $\epsilon = h\nu/m_e c^2$ is the dimensionless photon energy), and decrease by approximately an order of magnitude by $\nu \sim 10^{23}$ Hz ($\epsilon \sim 10^3$). Such a component could be due to IC scattering of an external photon field. The requirement that the bulk of such a component is confined to $\epsilon \lesssim 10^3$ constrains the seed photon field to energies $\epsilon_{seed} \gtrsim 1/\epsilon \sim 10^{-3}$, due to Klein-Nishina cross-section considerations [107]. Neither the broad line region ($\epsilon_{seed} \sim 10^{-5}$) nor the putative molecular torus ($\epsilon_{seed} \sim 10^{-6} - 10^{-7}$) photon fields [25] satisfy this constraint. So we, therefore, disfavor this possibility.

Another possibility is that the convex feature is still SSC emission resulting from structure in the electron energy distribution (EED). This would require that

the EED is convex at $\gamma \sim 10^3$,with a power-law form at higher energies that produces the $\nu \gtrsim 10^{23}$ Hz SSC SED. The resulting SSC convex point would be at $\epsilon \sim (\epsilon_{s,peak}/\delta)\gamma^2\delta \sim 10^3$, where $\epsilon_{s,peak} \sim 10^{-3}$ corresponds to the peak synchrotron energy, while δ and γ are the Doppler factor of the jet and the Lorentz factor of the electrons, respectively. A problem with this interpretation is that no convex point is observed in the synchrotron SED at $\nu \sim 10^{12}$ Hz (for $\gamma = 10^3,\ \delta = 10$, magnetic field $B \sim 0.1$ G). This may be attributed to the possibility that the synchrotron SED at that frequency is dominated by emission at larger ($\sim$ pc instead of $\sim 10^{-2}$ pc) spatial scales. Another problem this mechanism faces is that when the low energy EED varies, one expects that the EED at $\gamma \gtrsim 10^3$ varies as well. Variations, therefore, of the steep low energy EGRET emission should be accompanied by variations of the hard high energy EGRET emission. This, however, is not observed, as can be seen in Figure 1, where during Cycle 3 the soft low energy EGRET SED has disappeared, while the hard high energy EGRET component is very pronounced.

We examine now the possibility that the low energy EGRET emission is the high energy tail of the synchrotron component. During high X-ray states of TeV blazars, the X-ray spectrum becomes harder, and several instances have been observed of sources that exhibit flat or even rising SEDs up to ~ 100 keV, the maximum energy reachable by X-ray telescopes (e.g. Mrk 501, 1ES 1426+428, 1ES 2344+514; [108]). This behavior, expected from episodic particle acceleration [109], also characterizes Mrk 421, as can be seen in Figure 4. The upper limit (e.g. [110]) of the frequency of synchrotron radiation produced via diffusive shock acceleration can be obtained by equating the acceleration rate $t_{acc}^{-1} = c/\eta R_L$, where $R_L = m_e c\gamma/eB$ is the Larmor radius of an electron with Lorentz factor γ in a magnetic field B and $\eta \geq 1$, to the radiative loss rate $t_{rad}^{-1} = \sigma_\tau \gamma B^2(1 + (L_c/L_s))/(6\pi m_e c)$, where L_s and L_c are the synchrotron and inverse Compton luminosities of the source. This results to: $h\nu_s = 9\delta m_e c^2/4\eta\alpha(1 + L_c/L_s) \approx 150\delta/(\eta(1 + L_c/L_s))$ MeV, where $\alpha \approx 1/137$

is the fine structure constant, and the upper limit is obtained for $\eta = 1$. Extreme synchrotron acceleration has been observed in the case of the Crab nebula (e.g. [111]), in which the synchrotron SED peaks at the optical, beyond which it extends as a power-law up to ~ 30 MeV, suggesting $\eta \sim 1$ for this synchrotron dominated source. The possibility of extreme acceleration in blazars has been discussed by [112], who suggested that the so-called blazar sequence [12] may extend to powers significantly lower than those of the TeV blazars, producing strongly synchrotron dominated sources with synchrotron SEDs peaking up to ~ 200 MeV.

It is possible, however, that Mrk 421 is the first identified extreme extragalactic accelerator and one does not have to stretch the blazar sequence to look for such sources. An extragalactic extreme accelerator does not need to produce a synchrotron SED that peaks at MeV energies. An equally valid, and physically more plausible picture is the one exhibited by Crab, namely that, although the peak of the synchrotron component is at lower energies, the synchrotron SED extends to MeV energies, and is produced by electrons that after being accelerated, cool radiatively before they escape from the source [113]. As Figure 4.5 indicates, in the case of Mrk 421, as the X-ray flux increases the X-ray spectrum becomes harder, and it is possible that at the highest X-ray states the synchrotron spectrum extends and joins smoothly with the lower energy portion of the EGRET spectrum. This is demonstrated with the solid curves in Figure 4.5 that depict model SEDs for increasing values of η. In this scenario, the steep synchrotron emission can dominate over the hard SSC spectrum in the lower EGRET energies during the brightest X-ray states. This steep $\nu \lesssim 10^{23}$ Hz emission will be more variable and will not correlate well with the $\nu \gtrsim 10^{23}$ Hz SSC variations that are expected to be slower and of smaller amplitude. A hint of this behavior can already be seen in Figure 1. Note that from all the X-ray states depicted in Figure 4, only the highest ones seem to have the potential of connecting smoothly to the steep EGRET SED. This raises the issue of

duty cycle that can be addressed through simultaneous GLAST and X-ray observations of Mrk 421 and other TeV blazars. Such observations will help us evaluate our suggestion that TeV blazars are extragalactic transient extreme accelerators.

Chapter 5

Intricacies in the EGRET SED of Blazars

5.1 Introduction

The Energetic Gamma Ray Experiment Telescope detected 98 blazars (67 of which are confirmed) during its 9-year lifetime ([8] and [103]). A majority (67%) of these sources are flat spectrum radio quasars (FSRQs). 17 % of them are low-frequency peaked BL Lac objects (LBLs), 4% of them are high-frequency-peaked BL Lac objects (HBLs), and the rest are flat spectrum radio sources. The large bias towards FSRQs is due to the fact that the gamma-ray emission from these sources peaks at EGRET energies (30 MeV-10 GeV). The broadband spectral energy distribution (SED) of blazars, which are a class of active galactic nuclei, shows two broad peaks. The first peak is at infra-red/optical frequencies for *red blazars* which could be either the FSRQs or the LBLs and at UV/X-rays for *blue blazars* or the HBLs. The second peak is in the gamma-ray range (MeV-GeV) for LBLs & FSRQs and in the TeV range for HBLs. Although LBLs and FSRQs are grouped in one category, the peak frequencies for FSRQs are at lower frequemcies. However, the bolometric luminosity of the sources decreases from FSRQs to LBLs to HBLs. Consequently, LBLs were very often below EGRET's detection threshold in spite of having their peak frequency in or around the EGRET energy range.

A continuity in the observed spectral properties of BL Lacs and FSRQs has been postulated by [12, 27] with the gamma-ray spectral index getting progressively harder from FSRQs to HBLs based on the location of the EGRET energy range on the gamma-ray peak of these sources. For FSRQs, the EGRET energy range lies on the decreasing portion of their gamma-ray peak (in a broadband SED plot), they are

expected to have soft spectral indices. HBLs have the highest peak frequencies and the EGRET-range lies on the rising portion of the gamma-ray peak. Consequently, they are expected to have hard spectral indices. LBLs lie somewhere in between. Moreover, the spectral index is expected to harden smoothly (even within each category, viz. FSRQs, LBLs, HBLs) as the luminosity of the source decreases. This phenomenological picture in gamma-rays (described in [12]), obtained from from spectral averages constructed by binning 49 sources over five luminosity intervals was based on two pieces of information: a single spectral index for each source; and a monochromatic flux at 100 MeV, which was calculated from the standard EGRET flux (100 MeV-100 GeV) and the power-law index. The spectral indices used were from data that were mostly from the 2nd EGRET catalog [123, 124] which included the first two observation Cycles (1991 - Aug.1993), except for a few sources for which information from Cycle 3 and Cycle 4 were included.

Fossati *et al.* [12] and Ghisellini *et al.* [27] played an instrumental role in building a unified blazar paradigm. However, they did not take into account any intrinsic spectral variations for individual blazars and the dependence of spectral index on flux, more so, because it was too early in the EGRET mission (from the point of view of published results) for this information to be available. The comprehensive study of the entire EGRET data (1991-2000) from all 98 blazars ([103],henceforth N07, discussed in chapter 3) addressed the topic of gamma-ray spectral variability extensively. While there was a distinct difference between the average spectral index (2.26 ± 0.03) of the 66 FSRQs and the mean index (1.68 ± 0.09) of the 3 HBLs, the difference between FSRQs and LBLs (17 sources with a mean spectral index of 2.14 ± 0.08) was not that prominent. The quoted errors are the standard deviation of the mean, and do not take into account the spectral variations of individual blazars. For blazars observed multiple times, the average spectral index of all observations was used for computing the global mean for the whole class viz.

FSRQs, LBLs, HBLs.

It is also not clear if the predicted smooth trend of spectral hardening with decreasing luminosity would be obeyed within the FSRQ-LBL category, if the spectral variations of individual blazars are taken into account. For the sample of 26 blazars that we analyzed in chapter 3, we did not observe any clear correlation between the gamma-ray spectral index and flux (which could be translated into luminosity). Moreover, the two HBLs for which data was available, showed opposite trends (Figure 3.3). In all the discussions about EGRET data so far in the literature, it has been assumed that the blazar spectrum can be adequately represented by a power law. We found this not always to be in true based on the shape of the νF_ν spectra. The HBLs Mrk 421 and PKS 2155-304 showed a convex break in the νF_ν spectra (Figure 4.5 & Figure 4.6) [118, 121], which is perplexing from the point of view of the current theoretical models. We observed deviations from power-law behavior in FSRQs also. This is to be expected since the gamma-ray emission in these sources could come from various physical mechanisms that are not essentially correlated. In the scenario of leptonic models, it is well known that the first peak in the broadband SED of blazars is due synchrotron emission from relativistic plasma moving along the jet away from the core of the active galactic nucleus; the second peak is attributed to inverse-Compton scattering of relativistic electrons by soft ambient photons, that could originate from: synchrotron emission itself, the accretion disk, the broadline cloud region, or the infra-red dust surrounding the blazar nucleus (see [35] for a review of the models). Each of these processes has a contribution in different segments of the EGRET energy range. A careful examination of the νF_ν spectra could reveal interplay of these processes during the different states of flaring activity. The mission aggregated νF_ν could also reveal the extent of contribution of these components. The largest collection to date (33 sources), of EGRET contribution to the broadband SED was compiled by Von Montigny *et al.* [37], which

consisted of a single spectrum for each source. Other studies have presented the νF_ν spectra as a part of multi-wavelength campaigns or through TOOs initiated by EGRET or by other wavelengths, and typically show the flare spectra of the sources. The only blazars for which a multi-epoch broadband spectra were published in the same study (for a comparison to be possible) are PKS 0528+134 [39], 3C 279 [38] and 3C 273 [119] (multiple observations during Cycle 6 flare).

During our spectral study discussed in Chapter 3 [103], we observed that although the error bars on EGRET spectral indices are often large due to low statistics, some of those instances are due to the intricacies in the νF_ν spectra. A systematic study will help identify the specific cases. We are extending our spectral analysis in from Chapter 3, and presenting the individual and mission aggregated νF_ν spectra for all the well observed blazars. There will be a renewed interest in gamma-ray data from blazars after the launch of the Gamma Ray Large Area Telescope in early 2008 and this compilation will be a useful reference for that purpose. We present the analysis in section §5.2, and discuss the results in §5.3.

5.2 Analysis

We analyzed the data as described in section 2.1 and extracted the flux (>100 MeV) and significance of detection of each source. If the source of interest was detected at a significance $> 4\sigma$ in the energy interval >100 MeV, then a four point spectrum was determined using counts recorded in the energy intervals (in MeV) 30-100, 100-300, 300-1000 & >100. If the overall significance of detection of the source was greater than 6σ, the energy intervals with a strong detection were further split up into smaller intervals (for which standard EGRET maps exist) to determine the νF_ν spectra. For the strongest sources, the standard 10 intervals 30-50, 50-70, 70-100, 100-150, 150-300, 300-500, 500-1000, 1000-2000, 2000-4000, 4000-10000 (all in MeV) were utilized.

The sample of EGRET data analyzed in chapter 3 consists of 66 flat-spectrum radio quasars (FSRQ), 17 low-frequency peaked BL Lacs (LBL), 4 high-frequency peaked BL Lacs (HBL), 10 flat-spectrum radio sources (FSRS) and 1 radio galaxy. For the 26 blazars that were observed multiple times, we extracted the νF_ν spectra for the viewing periods and viewing period combinations mentioned in Table 3.3 in chapter 3. For the rest of the sources we repeated the analysis mentioned above for integrated maps for Cycles 1-4, Cycle 5 + Cycle 6, Cycle 7 + Cycle 8 + Cycle9. The Cycles in the latter half of the mission were not analyzed individually due to the restricted mode of operation of the instrument and the decrease in the detection efficiency, that ultimately lead to smaller number of counts overall. For sources that underwent a major flare, we extracted the spectra for that particular viewing period. And finally, we extracted the mission aggregated spectra for each source.

5.3 Results and Discussion

A variety of inverse-Compton mechanisms contribute to gamma-ray emission in the EGRET energy range. The synchrotron-self Compton (SSC) models [14, 15, 16, 17] assume that the seed-photons for inverse-Compton emission come from synchrotron emission itself. These models have had great success in fitting simultaneous X-ray and TeV data from HBLs, Mrk 421 [102, 75], PKS 2155-304 [71, 72], and Mrk 501 [76, 78].

Conversely, the photons could originate outside the jet under the broad class of external-Compton (EC) models. The possible sources are: the accretion disk (termed as ECD, external Compton scattering of direct disk radiation-[18, 19]), accretion disk photons after being re-scattered by surrounding broad-line-region (BLR) clouds as in the ECC models (external Compton scattering from clouds,[20, 21, 22]), and the infrared (IR) dust that surrounds the blazar nucleus (External Compton from infrared dust-ERC(IR); [24, 25]). The dust is more concentrated in

a torus that lies in the equatorial plane of the blazar [26]. Quite often, a combination of these models is required to fit the broadband spectrum FSRQs. Model fits to the broadband spectrum from 3C 279 by [38] & [68] and PKS 0528+134 by [66] show that moderate to large flares require a greater contribution from the ERC processes. In case of LBLs, while the low to moderate states can be fit with the SSC model, but large flares require an ERC contribution [69]

Each of the inverse-Compton component processes has a peak at a different frequency. The ERC(IR) process has a predominant contribution in the lower MeV (1 MeV -30 MeV $\sim 10^{20}$-10^{22} Hz) region [25], leading to a steep component in the SED at EGRET (30 MeV-10 GeV) energies. The ECD process due comptonization of the accretion disk photons also leads to a bump peaking in the same range of frequencies [38]. The ECC process (due to seed photons from the broad line cloud region) however has peak at a much higher frequency, $\sim 10^{23}$ Hz. In contrast, the SSC emission does not have a pronounced peak, and has the form of a plateau instead, which could extend from $10^{19} - 10^{23}$ Hz. The present data do not have sufficient resolution in frequency and time to constrain the parameters in the theoretical models, and visually identify the various external components in play, even in situations when the data show a significant excess above SSC emission. But a careful examination of the different SEDs will shed light on the variation and the relative importance of *some* EC component in the gamma-ray emission. We discuss νF_ν spectra of some of the individual sources below which were observed multiple times during the EGRET mission.

5.3.1 3C279

3C 279 was the first blazar (an FSRQ) recognized in the EGRET data [122]. The source flared several times over the course of the mission. Multi-epoch broadband spectra using simultaneous data were presented in Hartman *et al.* 2001 [38].

The data were fitted using a leptonic model [125]. The spectral states during a flare needed a considerable contribution from the external component due to the broad line clouds (ECC). Figures 5.1 & 5.2 show the multi-epoch νF_ν spectra for 3C 279. The spectrum from the large flares during VP 3.0, VP 11.0, VP 511.5 show a distinct bump. This is most likely caused by a combination of inverse-Compton emission from the broad line clouds.

We also extracted the mission long νF_ν spectrum to get an idea of the extent of the inverse Compton contribution shown in Figure 5.2-(e). The scale has been readjusted to make the picture clearer. The 9-year spectrum cannot be represented by a power law, which is to be expected considering the contribution from different time-varying inverse-Compton processes. However, an extremely clear presence of a EC component due to broad line clouds and/or accretion disk (most probably a combination of both) can be seen. It will be instructive to compare this feature with the other well observed blazars to see which of them have a lasting contribution from the EC processes. With the increased sensitivity of GLAST, such a spectrum can be captured in a much shorter time, enabling a correlation analysis between different bands.

The spectral index vs flux plot for 3C 279 shown Figure 3.5 shows an interesting trend (this was discussed in detail in Chapter 3) at low fluxes. The index softens with increasing flux. The lowest flux state is relatively hard, with a spectral index of 1.88$\pm$ 0.22 in the aggregated data from Cycle 6. The νF_ν spectrum in Figure 5.2 (a), shows an increasing contribution from the last four intervals spanning 500 MeV -10 GeV. However, this is not a feature common to aggregated states. The spectrum from Cycle 3 is steep with an index of 2.34$\pm$0.1. GLAST will be able to measure the spectra during low states with a higher accuracy and effectively capture the spectrum beyond 10 GeV, due to the larger effective area and a better design to circumvent the self-vetoing problem that EGRET had.

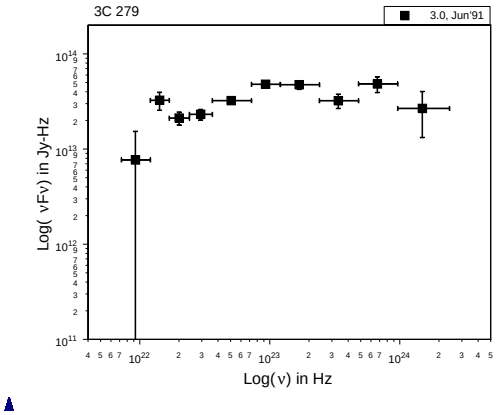

(a) Viewing period 3.0

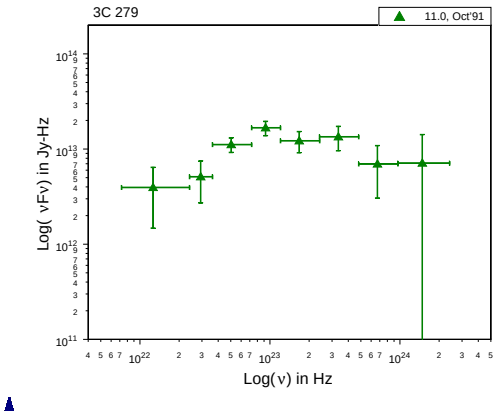

(b) Viewing period 11.0

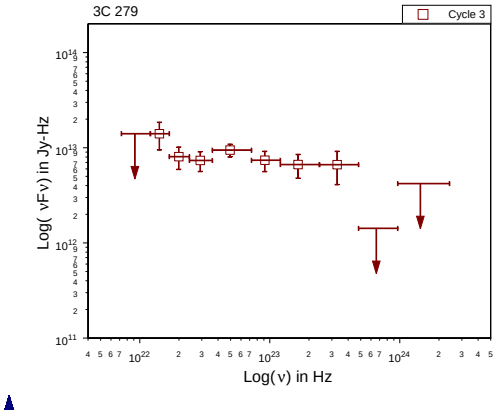

(c) Cycle 3 Average Spectrum

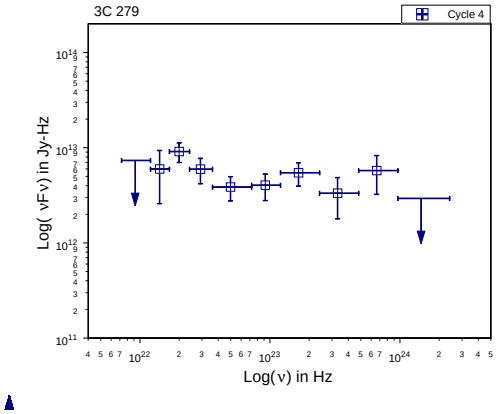

(d) Cycle 4 Average Spectrum

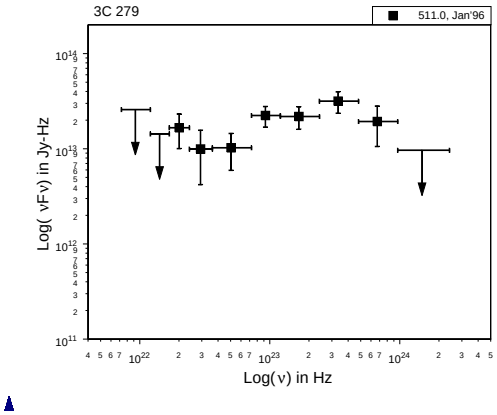

(e) Viewing period 511.0

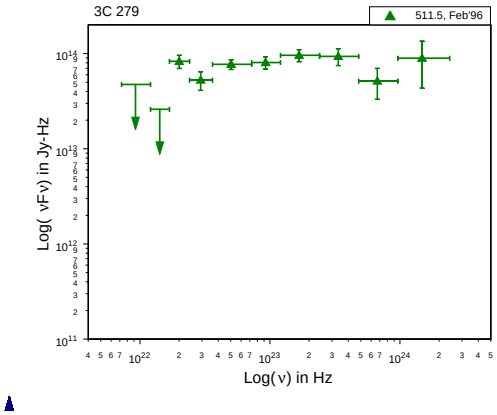

(f) Viewing period 511.5, Largest Flare

Figure 5.1: Multi-epoch νF_ν spectra for 3C 279

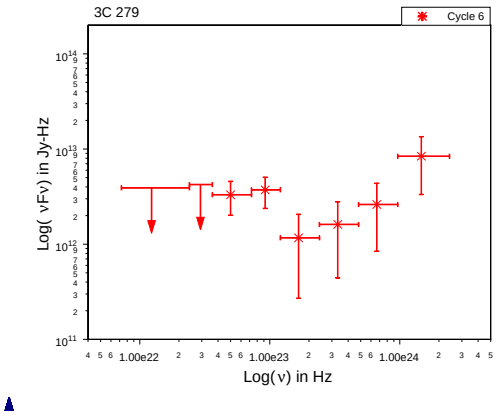

(a) Viewing period 806.5

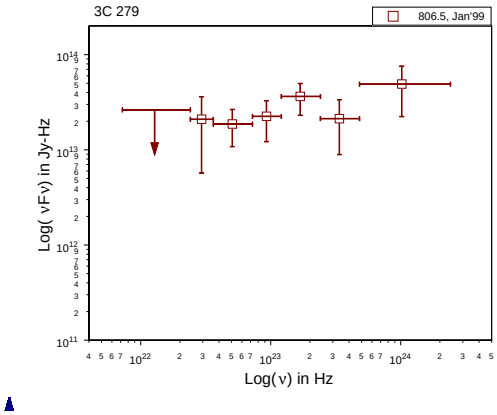

(b) Viewing period 806.5

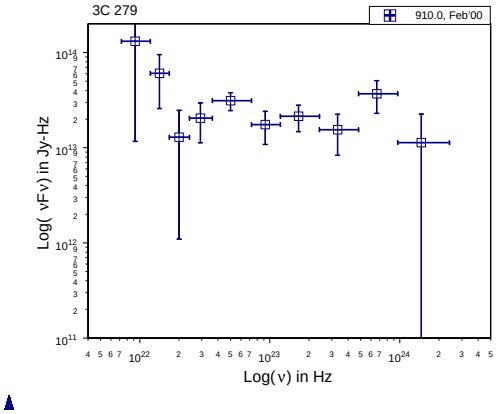

(c) Viewing period 910.0

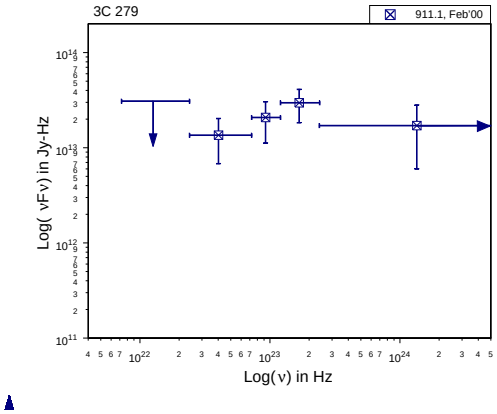

(d) Viewing period 911.1

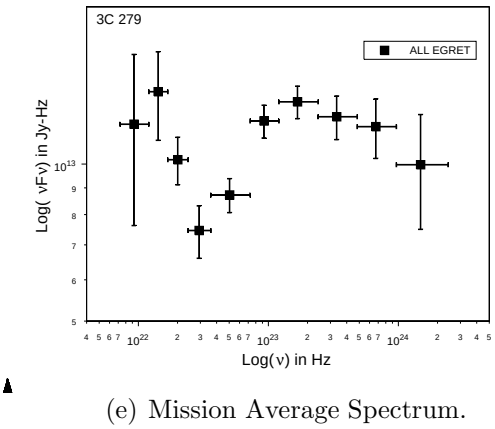

(e) Mission Average Spectrum.

Figure 5.2: Multi-epoch νF_ν spectra for 3C 279

5.3.2 PKS 1622-297

PKS 1622-297 was not a significant EGRET source until it flared in Cycle 4 (4 consecutuve viewing periods 421.0, 422.0, 423.0, and 423.5 in June 1995). The source showed rapid varibility on time scales of hours (doubling time of 8 hrs [52]). Counterclock wise spectral hysteresis was observed during the flare (we saw this in Figure 3.8), which was explained as the onset of an external component. This evolution can be observed in the four νF_ν spectra shown in Figure 5.3 a-d. The spectrum in 421.0 was soft. Elevated emission (probably the onset of EC component) can be seen at higher energies, propagating to lower energies during the course of the next two viewing periods.

5.3.3 PKS 1406-076

PKS 1406-076, a flat spectrum radio quasar, underwent a moderate flare in December, 1992. The light profile, shown in Figure 3.8 during 4 consecutive viewing periods 203.0-207.0 of observation consisted of a rise and fall, followed by a subsequent rise in flux. Figure 5.5 a-d show the SED during those 4 viewing periods. The spectral index shows a counter-clock wise hysteresis (see Figure 3.8). The appearance, decrease and reappearance of a component at higher EGRET energies can be seen in VPs 205.0, 206.0 and 207.0.

5.3.4 PKS 0528+134

PKS 0528+134 is a flat spectrum radio-quasar (farthest one detected yet, z$\sim$ 2), which has shown repeated outburts in gamma-rays. The next best observed blazar after 3C 279, it went though a flaring episode April-May 91 when it was observed in during four consecutive (shortened) viewing periods- 0.2, 0.3, 0.4 and 0.5. The multiwavelength fits to simultaneous data (Mukherjee *et al.* 1999 [39]) show

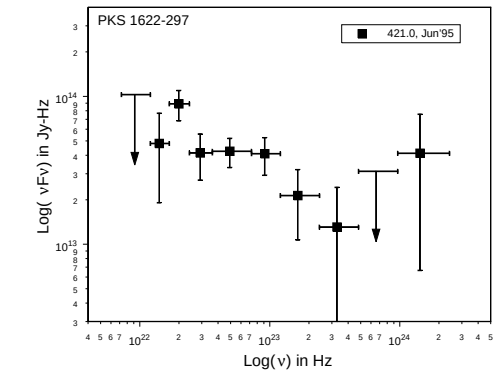

(a) Viewing period 421.0

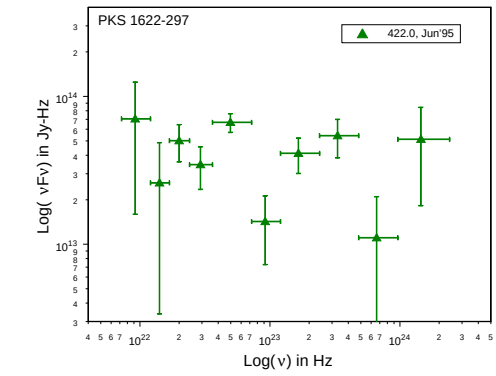

(b) Viewing period 422.0

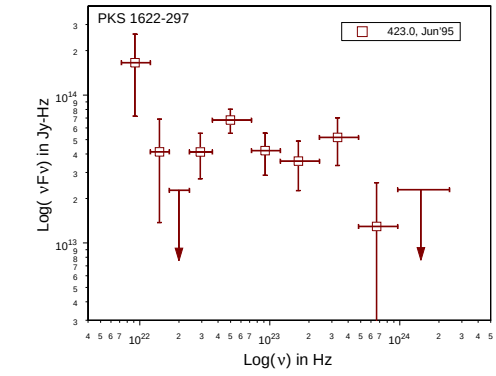

(c) Viewing period 423.0

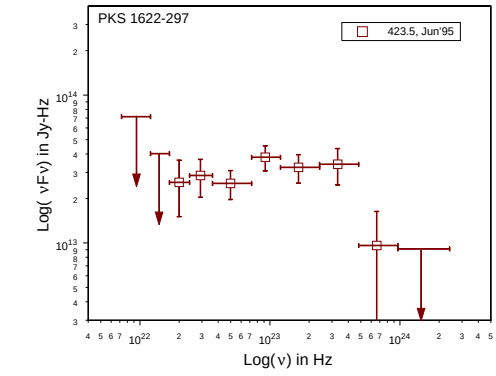

(d) Viewing period 423.5

Figure 5.3: Multi-epoch νF_ν spectra for PKS 1622-297 during the giant flare in 1997.

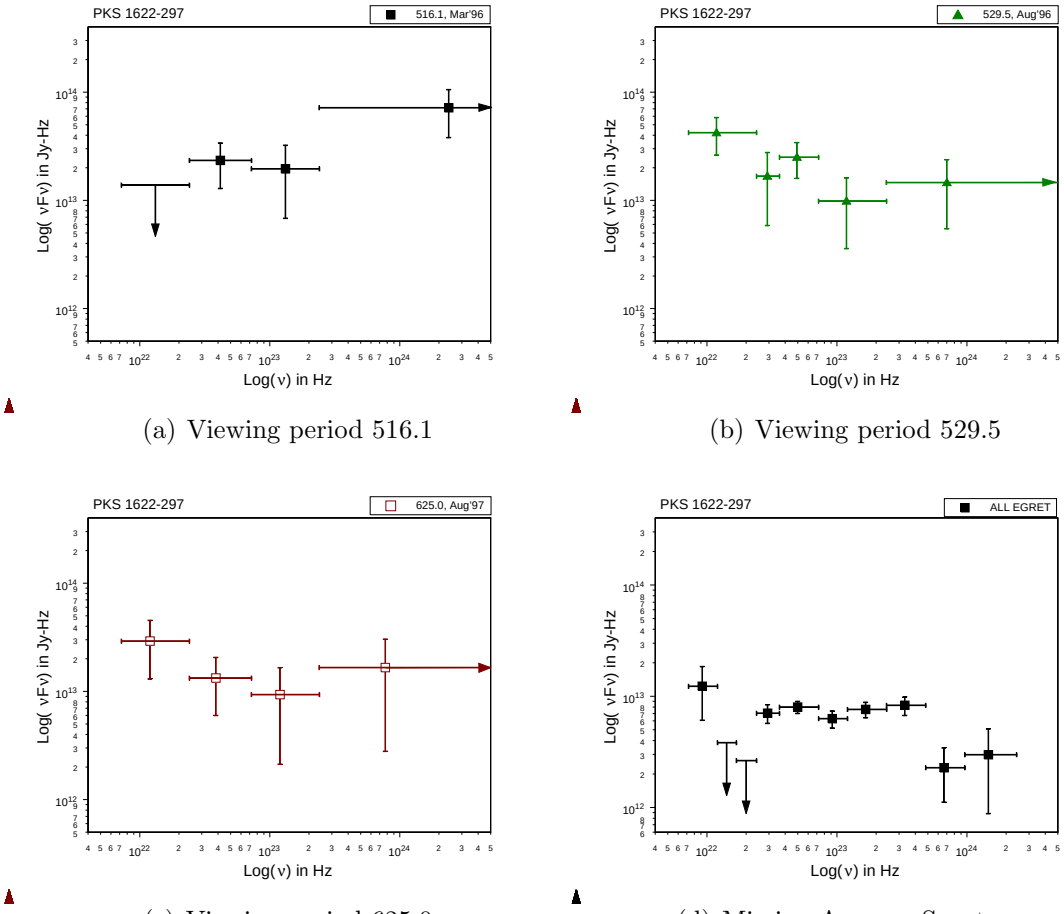

(a) Viewing period 516.1

(b) Viewing period 529.5

(c) Viewing period 625.0

(d) Mission Average Spectrum

Figure 5.4: Multi-epoch νF_ν spectra for other states of PKS 1622-297. All plots are on the same scale that different from the scale used in figure 5.3, which show the flaring states.

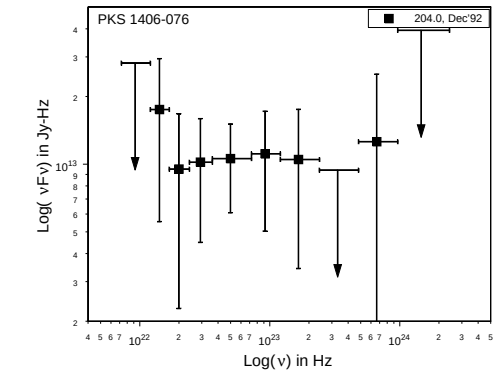

(a) Viewing period 204.0

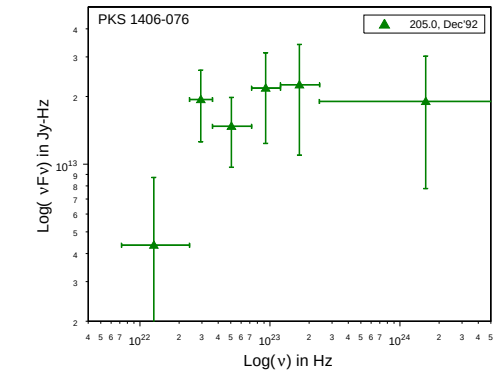

(b) Viewing period 205.0

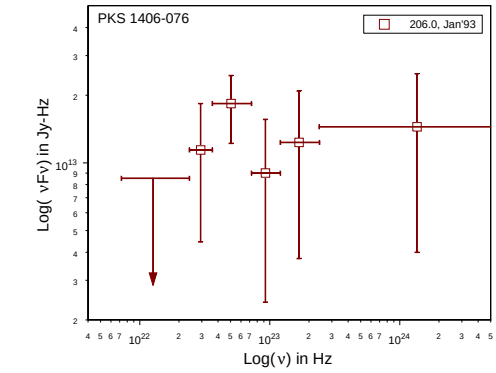

(c) Viewing period 206.0

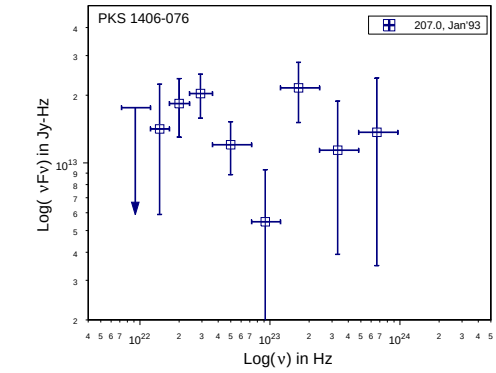

(d) Viewing period 207.5

Figure 5.5: Multi-epoch νF_ν spectra for PKS 1406-076 during 4 consecutive viewing periods

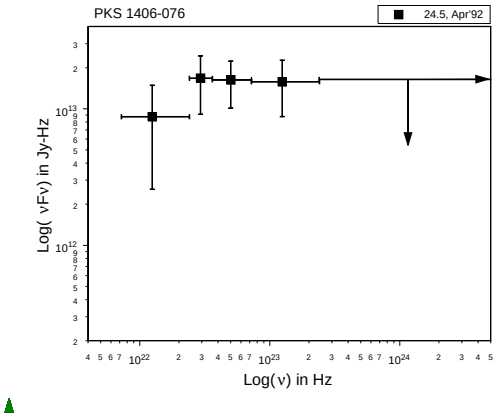

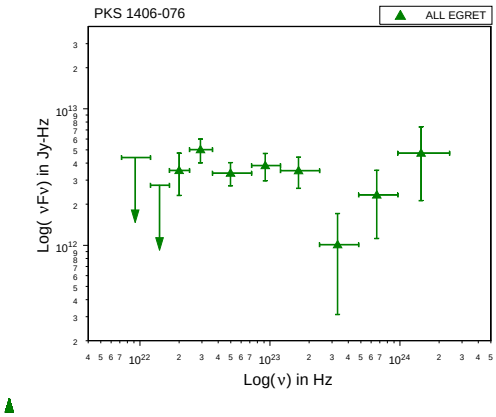

Figure 5.6: Multi-epoch νF_ν and ALL-EGRET spectrum for PKS 1406-076

that the low flux states could be fitted well with SSC emission. The flaring states needed a contribution from external Compton emission. Figure 5.7 shows the SED from the four states. As with other sources, one can see the emergence of another component at higher energies. It is interesting to note that the spectrum during the largest flare (Viewing period 213.0) does not have any recognizable kinks (Figure 5.8). The 9-year mission average spectrum does not show any lasting presence of an external component. It is possible that there is another source of emission (Comptonizaion of infrared dust from torus) that surpasses the emission from the other two EC components. This has been postulated for PKS 0528+134 [25] and was not included in the fits in [39]. The subject of MeV emission in some blazars is discussed in the next section.

5.3.5 MeV Blazars

The external-Compton models predict a spectral break (MeV break) of 0.5 in the MeV gamma-ray region, which is location of the inverse-Compton peak for FSRQs [24]. Some blazars, categorized as MeV blazars, are bright in the MeV region (below the EGRET energy range and spanned by the Compton telescope COMPTEL), and are expected to have an "MeV break" that is greater than 0.5 The value is computed using the difference between the spectral indices on both sides of the break. The EGRET region falls on the higher energy side of the IC peak. Consequently getting this index is not a problem. However, not much data is available on the lower energy side due to the limited sensitivity of COMPTEL. Assuming that there is no additional break in the power law on the rising branch of the inverse-Compton peak, a spectral difference between the EGRET index and an X-ray spectral index could provide an estimate of how much the MeV break could be, and would be useful to compute in the absence of MeV data. A detailed analysis of simultaneous data between the EGRET and XTE missions (Nandikotkur *et al.*

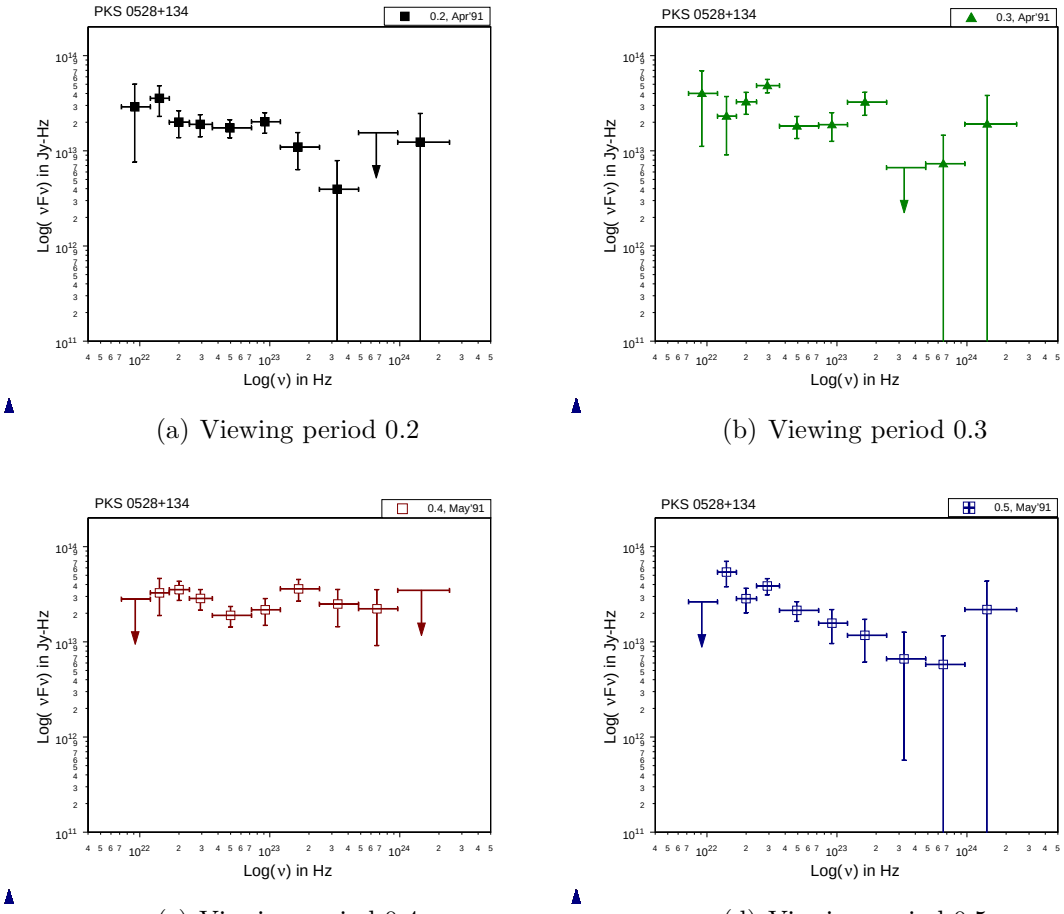

(a) Viewing period 0.2

(b) Viewing period 0.3

(c) Viewing period 0.4

(d) Viewing period 0.5

Figure 5.7: Multi-epoch νF_ν spectra for PKS 0528+134 during a flare that lasted 20 days (4 consecutive viewing periods). The spectral index shows a counter clockwise hysteresis as shown in Fig. 3.8

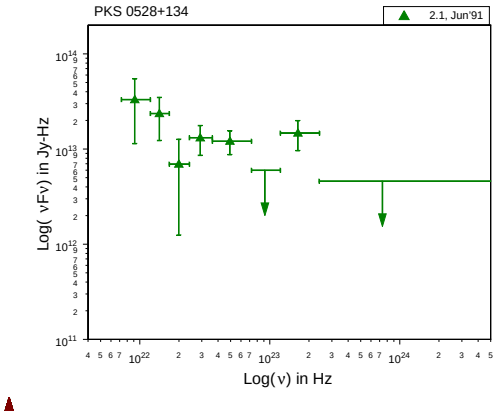

(a) Viewing period 2.1

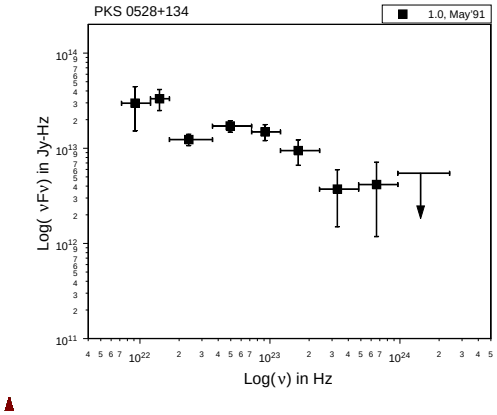

(b) Viewing period 10.0

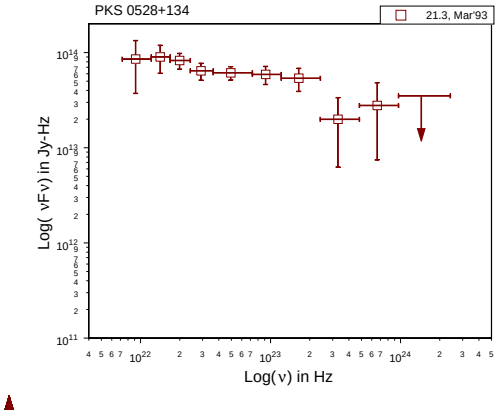

(c) Viewing period 213.0

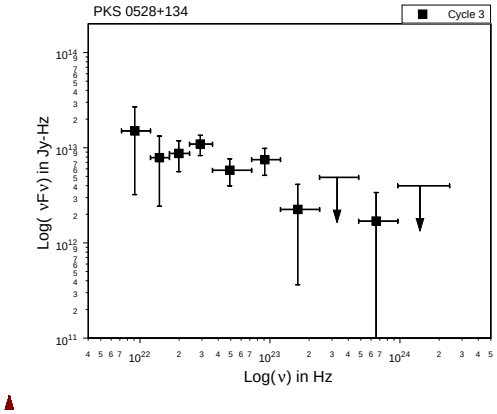

(d) Viewing period Cycle 3

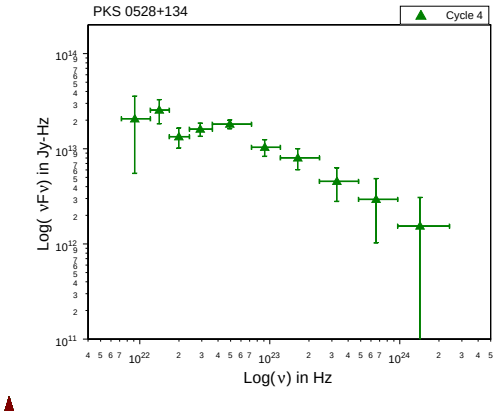

(e) Viewing period Cycle 4

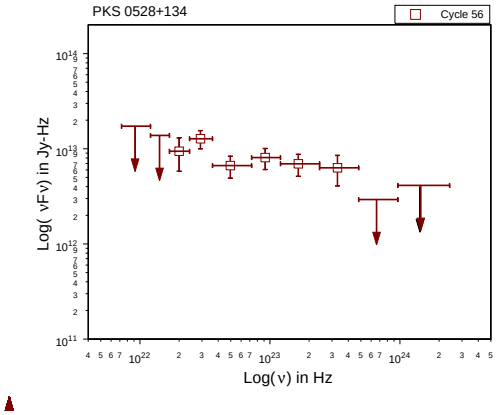

(f) Viewing period CYcle 5

Figure 5.8: Multi-epoch νF_ν spectra for PKS 0528+134

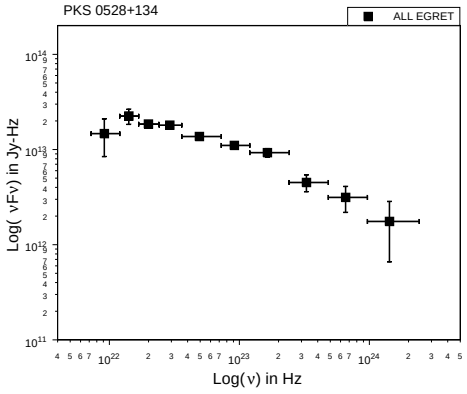

(a) 9 Year EGRET spectrum for PKS 0528+134

Figure 5.9: Mission Average spectrum for PKS 0528+134

2001 [117]) showed interesting pattern in the spectral breaks of blazars. The sources PKS 0208-512, PKS 0528+134, PKS 1156+295 and 3C 273, which were detected by COMPTEL due to their strong emission in the MeV region, had breaks greater than 0.5. The other FSRQs, 3C 279 and PKS 1622-297, had a break that was less than 0.5. A recent analysis by Stacy *et al.* 2003 [62], found no evidence of spectral breaks in the combined multi-epoch COMPTEL and EGRET data for PKS 0208-512. They suggested that PKS 0208-512 should not be classified as an "MeV Blazar".

Figure 5.10 shows all the νF_ν spectra for PKS 0208-512. In our spectral study in chapter 3 (see Figure 3.3), this source showed in interesting relationship between spectral index and flux. The index softened with increasing flux at lower fluxes and then subsequently hardened. These spectral changes are also seen in the νF_ν spectra. The flaring viewing period 517.0 shows a hard spectrum with a bump which could possibly signify an external component. Such an effect can also be seen in spectrum from VP 10.0 and Cycle 3. These bumps are similar in appearance to those in 3C 279, where the contribution to the SED from the broad line cloud region is pronounced. Also note worthy is the hard spectrum in the lowest state.

3C 273 is definitely known to have a strong MeV component, and was detected by COMPTEL [83]. The spectra (Figure **??**) show steep indices and no recognizable

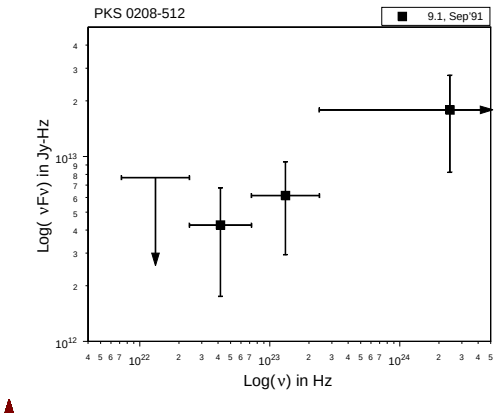

(a) Viewing period 9.1

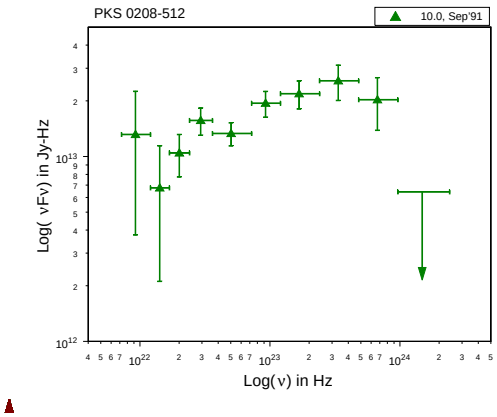

(b) Viewing period 10.0

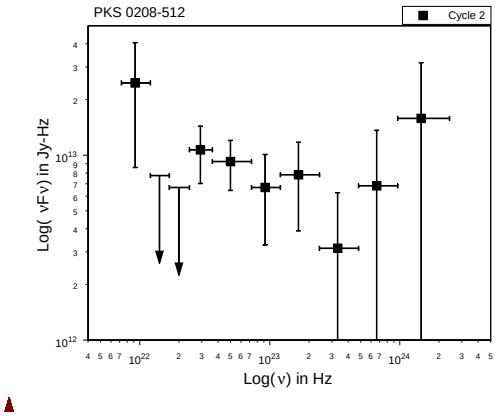

(c) Cycle 2

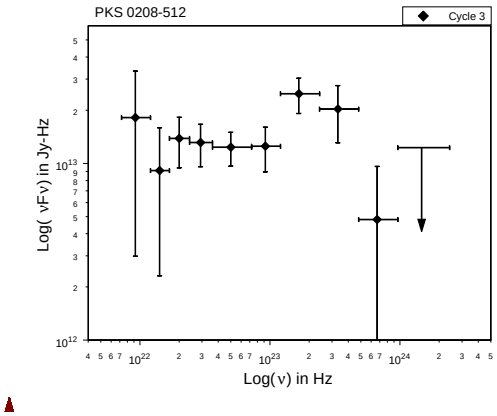

(d) Cycle 3

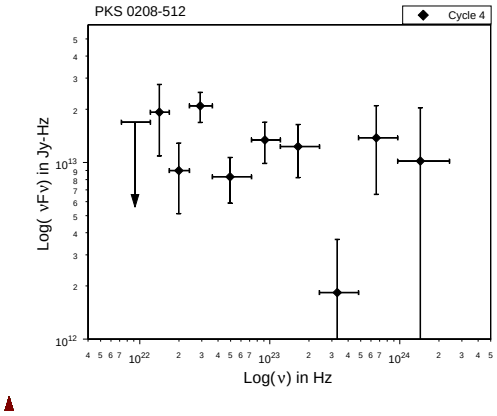

(e) Cycle 4

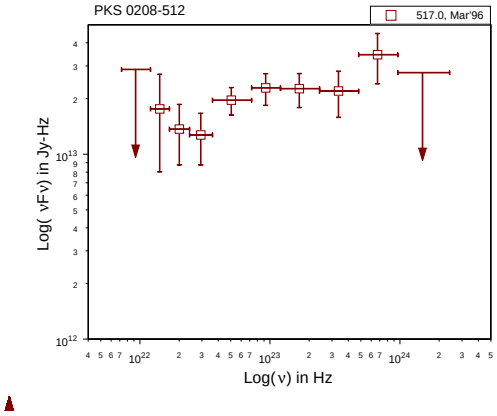

(f) Viewing Period 517.0

Figure 5.10: Multi-epoch νF_ν spectra for PKS 0208-512

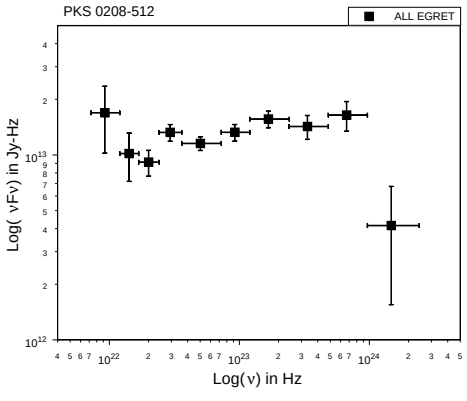

(a) 9 Year EGRET spectrum for PKS 0208-512

Figure 5.11: Mission average spectrum for PKS 0208-512

contribution from a separate ccomponent in the EGRET band. The 9-year spectra for PKS 0528+134 and 3C 273 are similar and featureless. But these are distinctly different from that for PKS 0208-512, indicating that the latter has variable levels of activity in the different EGRET bands. While it might be strong at sub-EGRET MeV energies, it could potentially show complicated variability it the EGRET energy range. Upcoming observations by GLAST would help identify and classify the variability patterns.

The νF_ν spectra for the remaining blazars, that were observed multiple times, are shown in Figures 5.15 - 5.27.

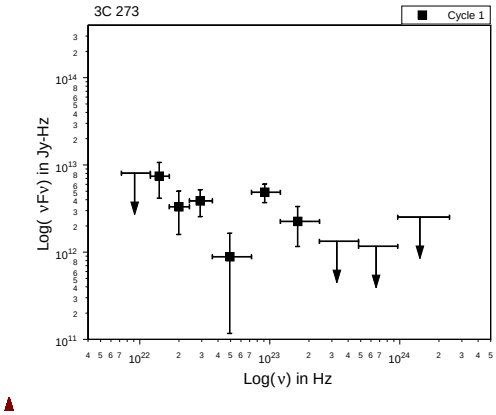

(a) Cycle 1

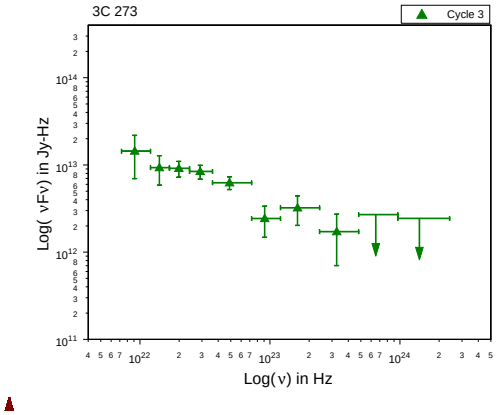

(b) Cycle 3

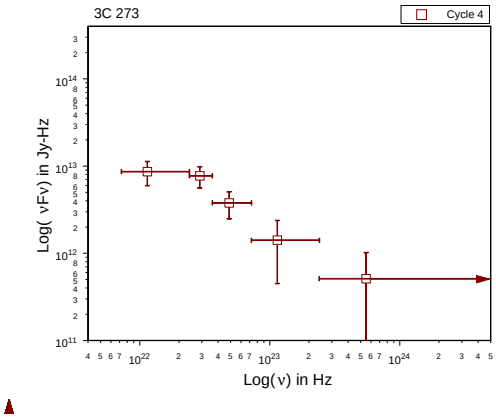

(c) Cycle 4

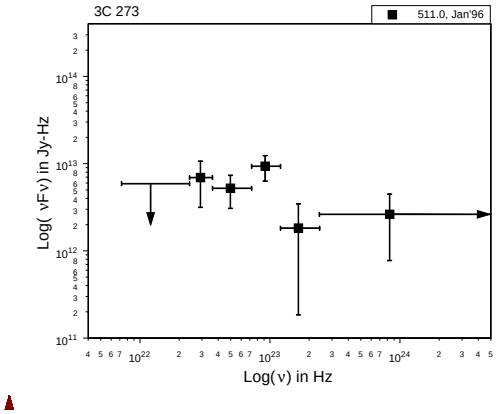

(d) Viewing Period 511.0

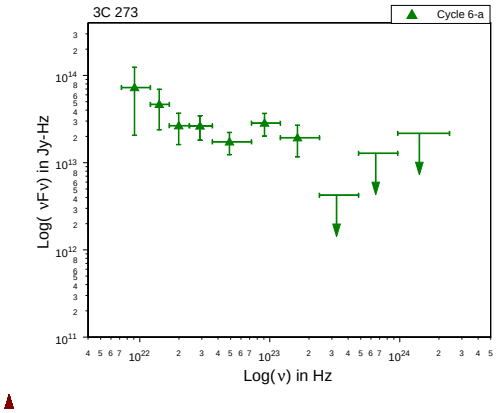

(e) Cycle 6a- Viewing Periods 609.0, 610.0

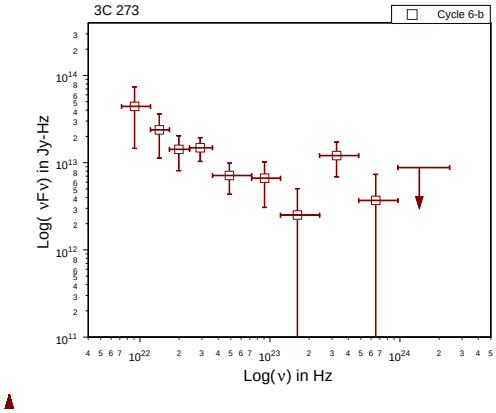

(f) Cycle 6b

Figure 5.12: Multi-epoch νF_ν spectra for 3C 273

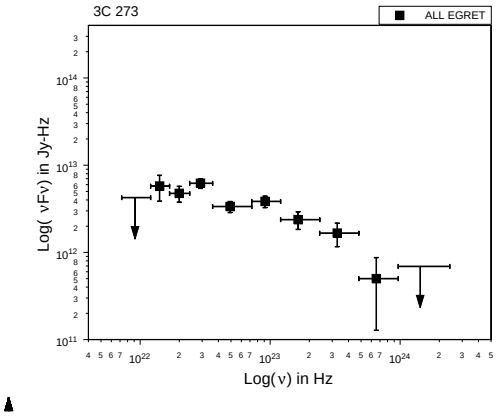

(a)

Figure 5.13: Mission Average νF_ν spectrum for 3C 273

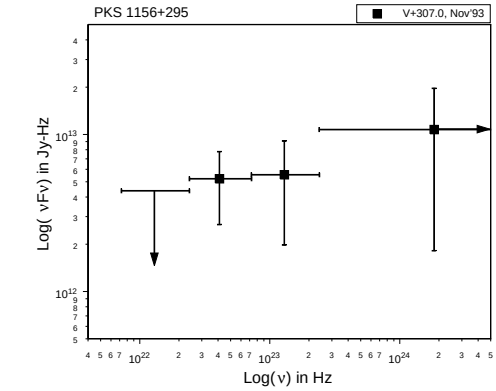

(a) Viewing Period 307.0

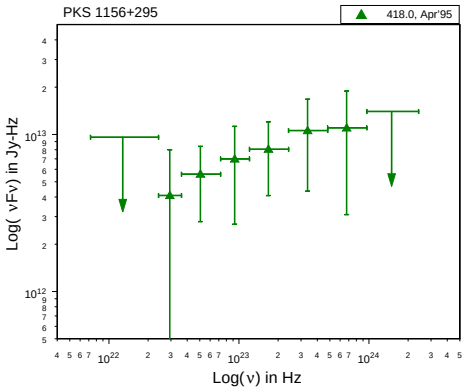

(b) Viewing Period 418.0

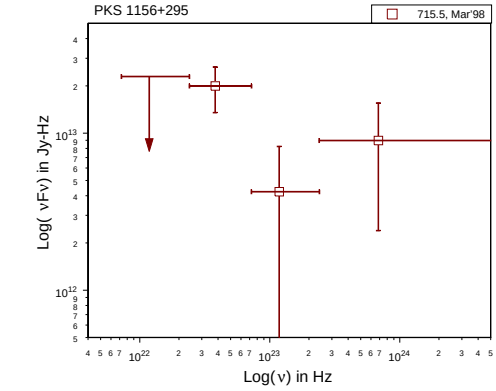

(c) Viewing Period 715.5

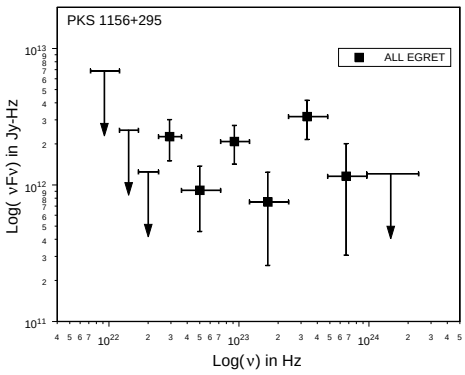

(d) Multi -epoch for νF_ν PKS 1156+295

Figure 5.14: Multi-epoch νF_ν spectra for PKS 1156+295

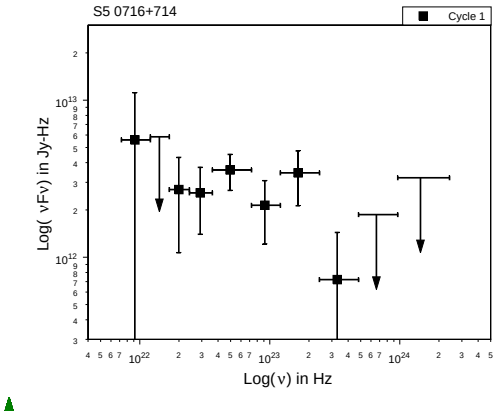

(a) Cycle 1

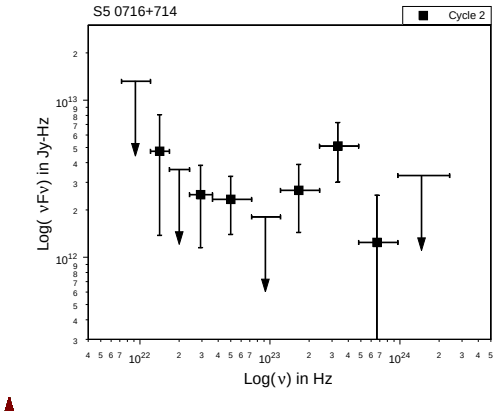

(b) Cycle 2

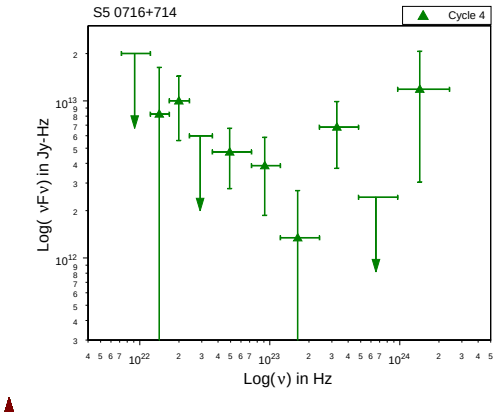

(c) Cycle 4

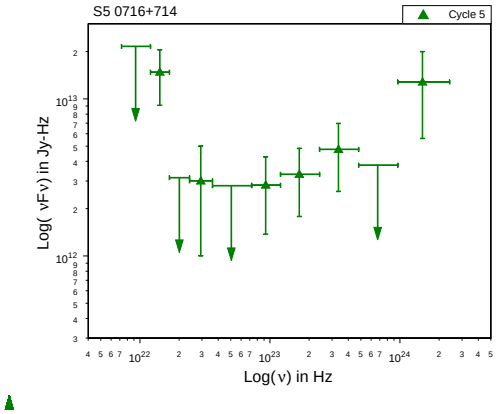

(d) Cycle 5

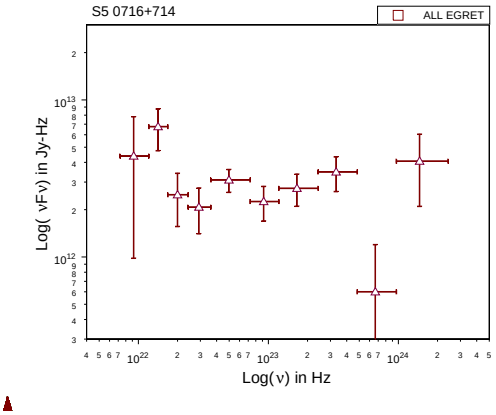

(e) Mission Average Spectrum

Figure 5.15: Multi-epoch νF_ν spectra for S 0716+714

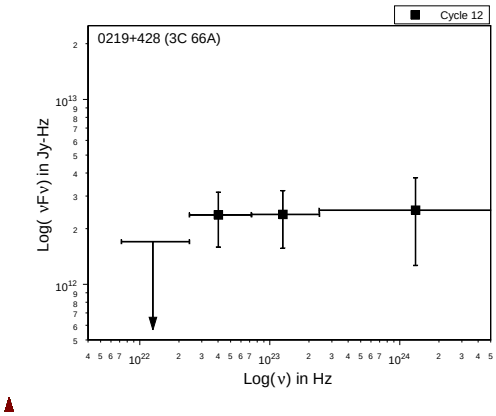

(a) Cycle 1+2

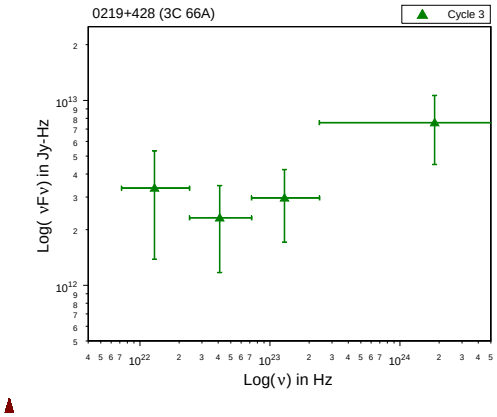

(b) Cycle 3

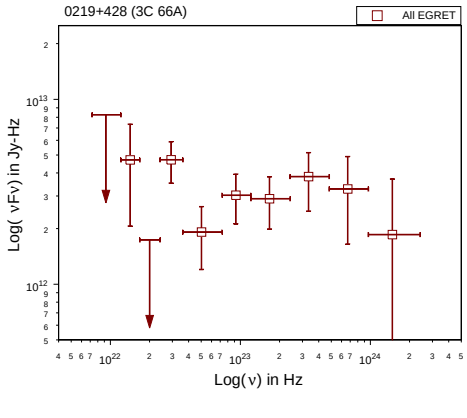

(c) Misson Average SED

Figure 5.16: EGRET SED for 0219+428 (3C 66A)

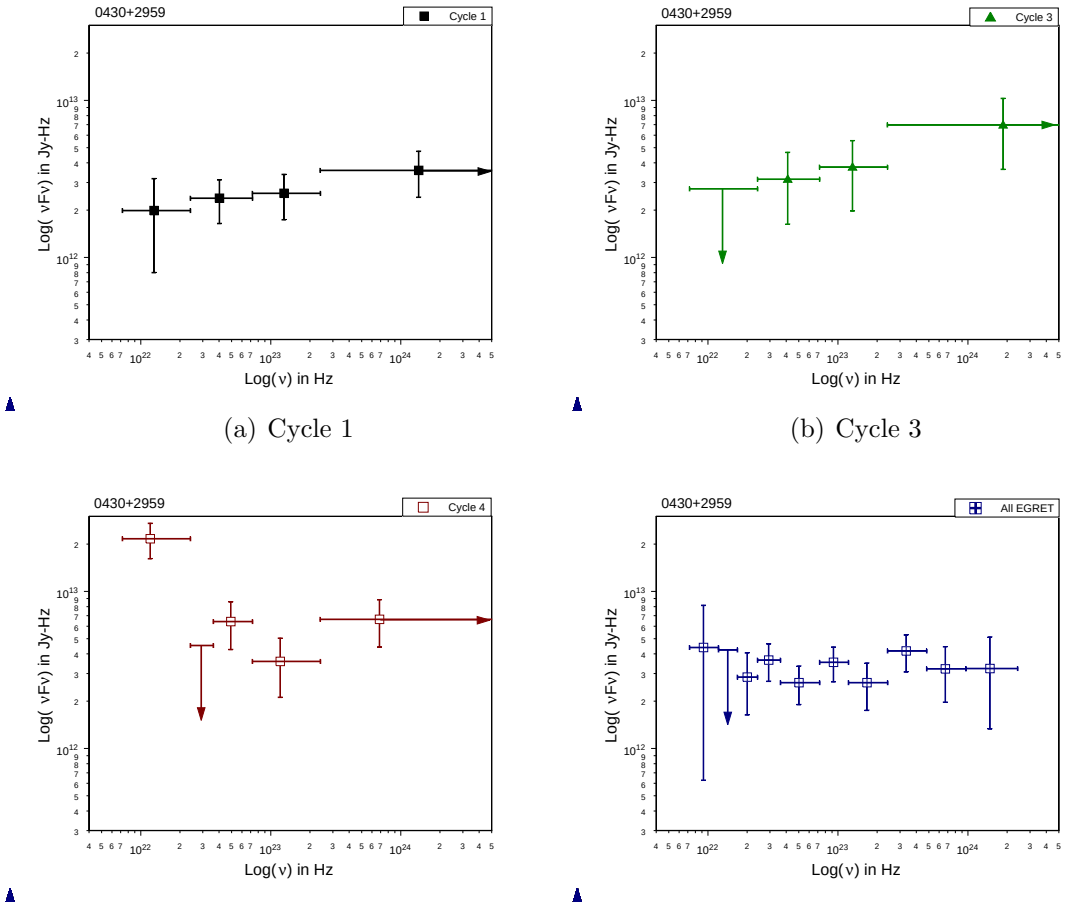

(a) Cycle 1

(b) Cycle 3

(c) Cycle 4

(d) Mission Average Spectrum

Figure 5.17: EGRET SED for 0430+2859

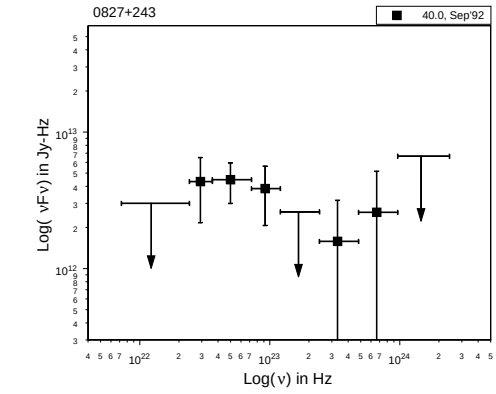

(a) Viewing Period 40.0

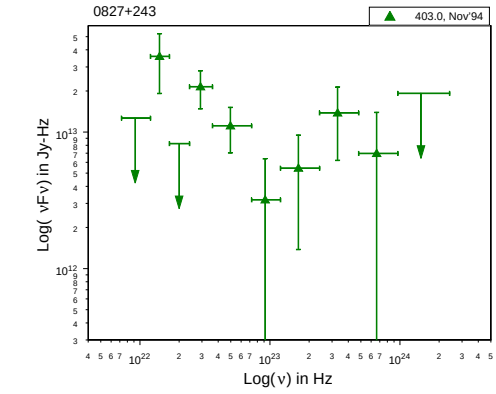

(b) Viewing Period 403.0

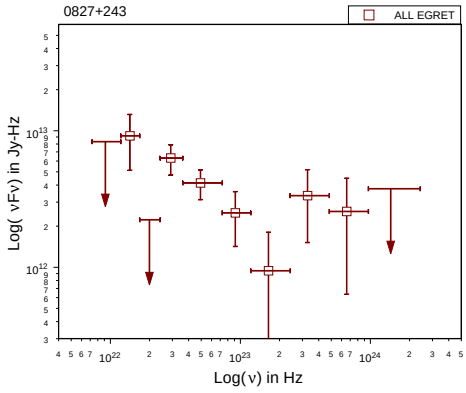

(c) Mission Average Spectrum

Figure 5.18: EGRET SED for 0827+243 (OJ 248)

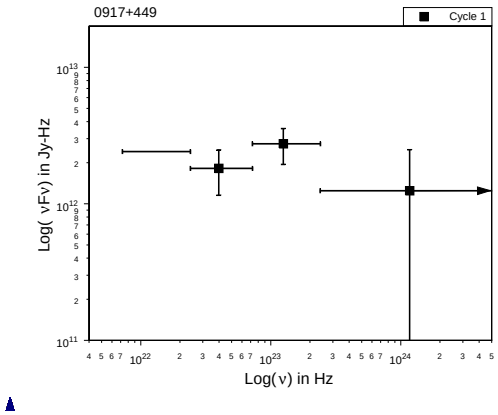

(a) Cycle 1

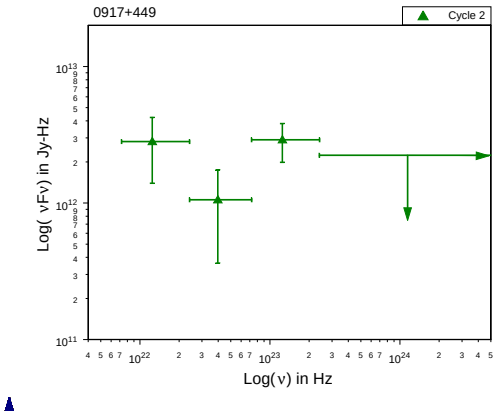

(b) Cycle 2

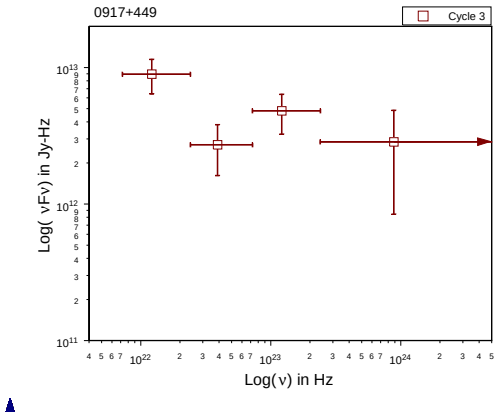

(c) Cycle 3

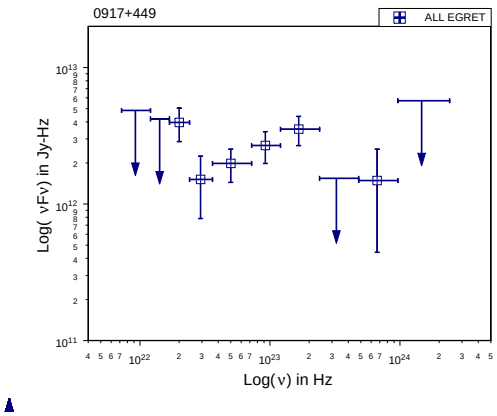

(d) Mission Average Spectrum

Figure 5.19: EGRET SED for 0917+449

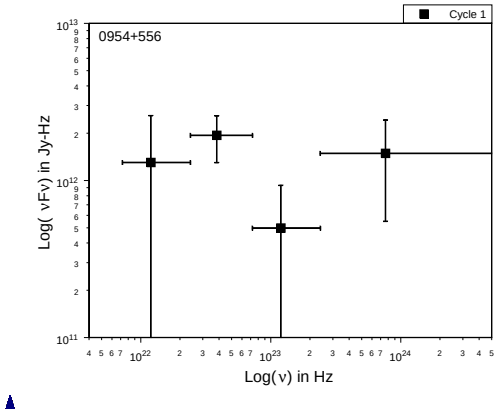

(a) Cycle 1

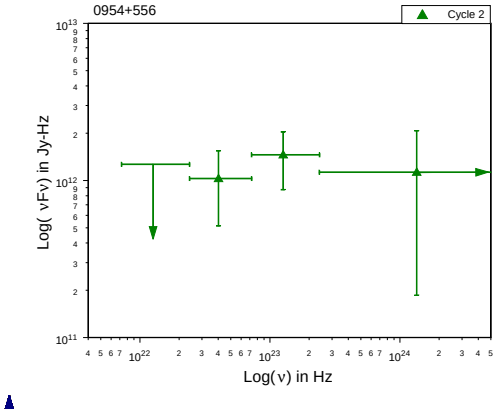

(b) Cycle 2

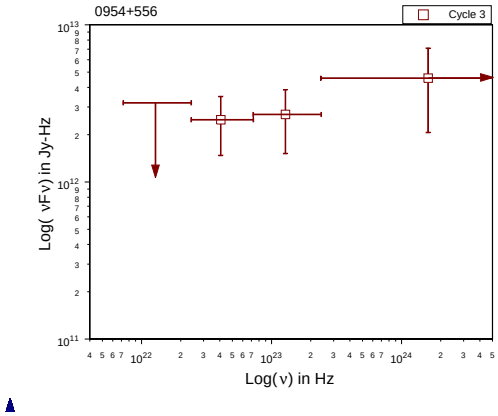

(c) Cycle 3

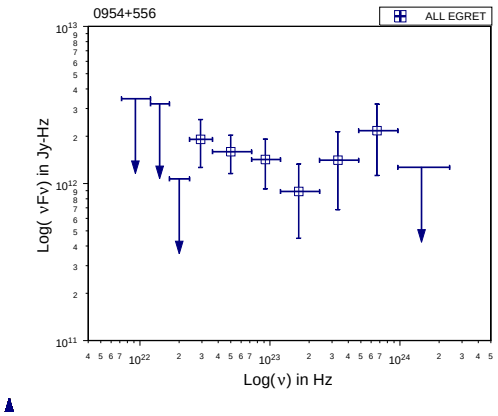

(d) Mission Average Spectrum

Figure 5.20: EGRET SED for 0954+556

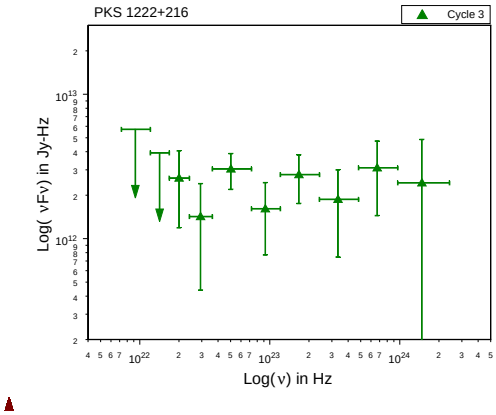

(a) Cycle 2

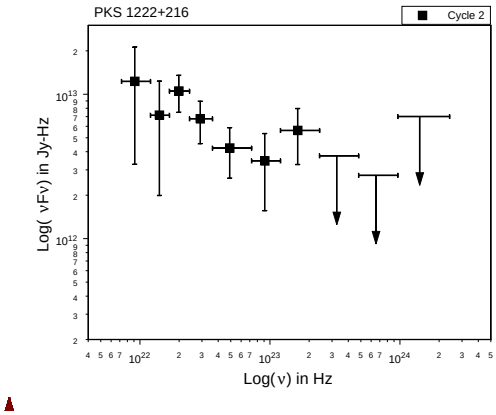

(b) Cycle 3

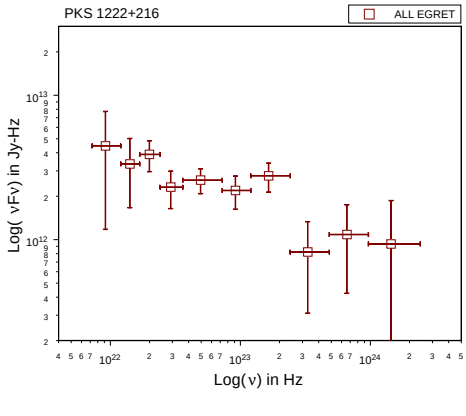

(c) Mission Average Spectrum

Figure 5.21: EGRET SED for 1222+216

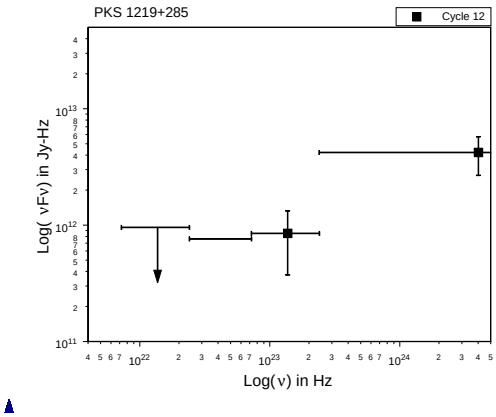

(a) Cycle 1+2

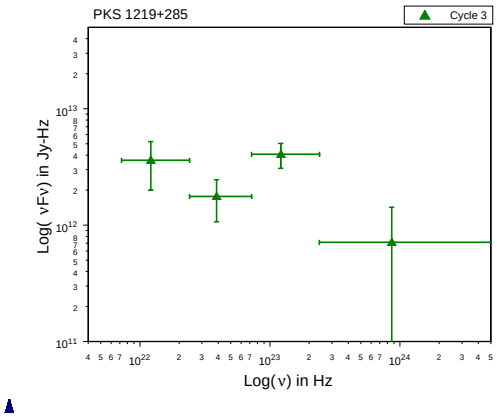

(b) Cycle 3

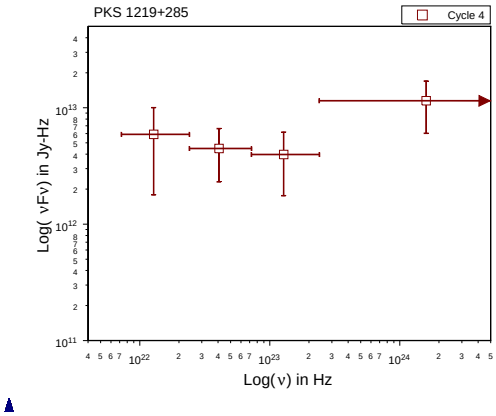

(c) Cycle 4

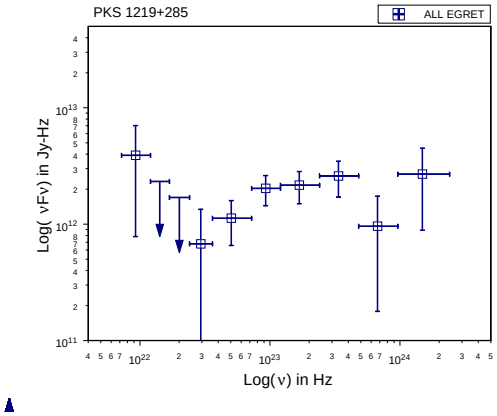

(d) Mission Average Spectrum

Figure 5.22: EGRET SED for 1219+285

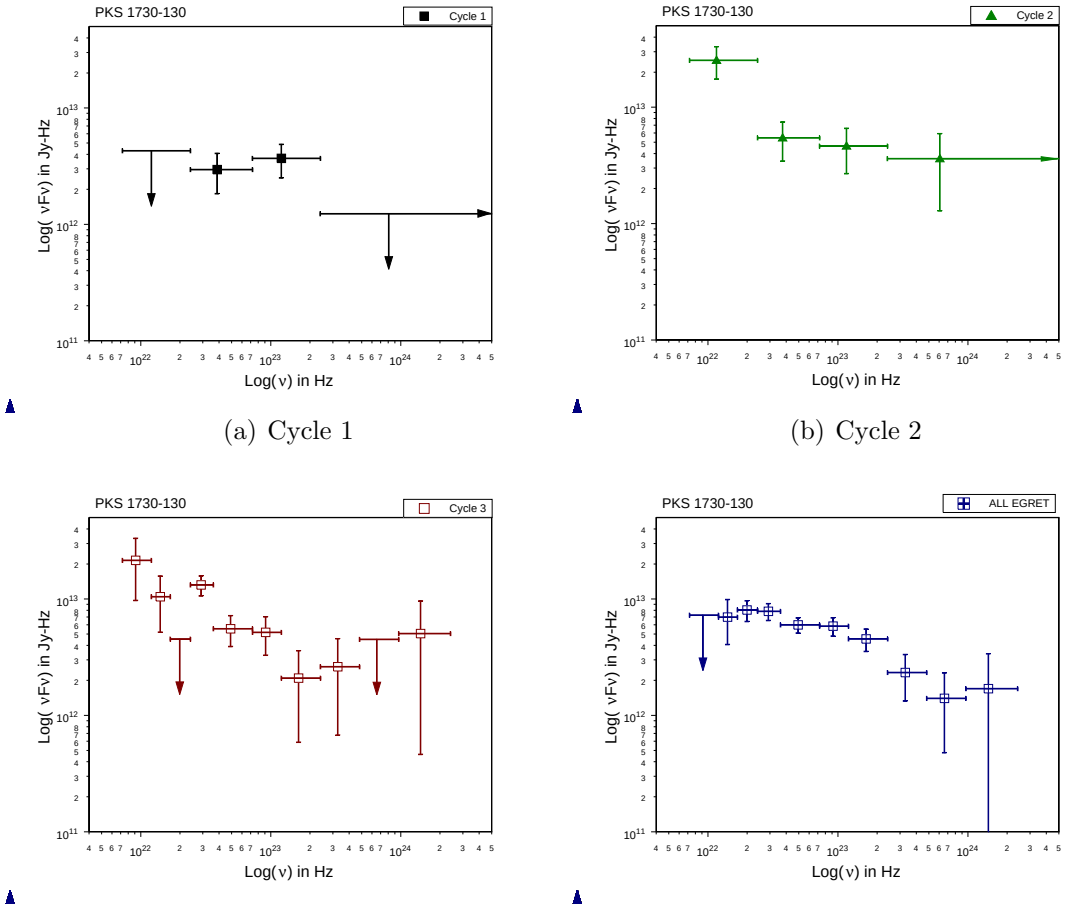

(a) Cycle 1

(b) Cycle 2

(c) Cycle 3

(d) Mission Average Spectrum

Figure 5.23: EGRET SED for 1730-130

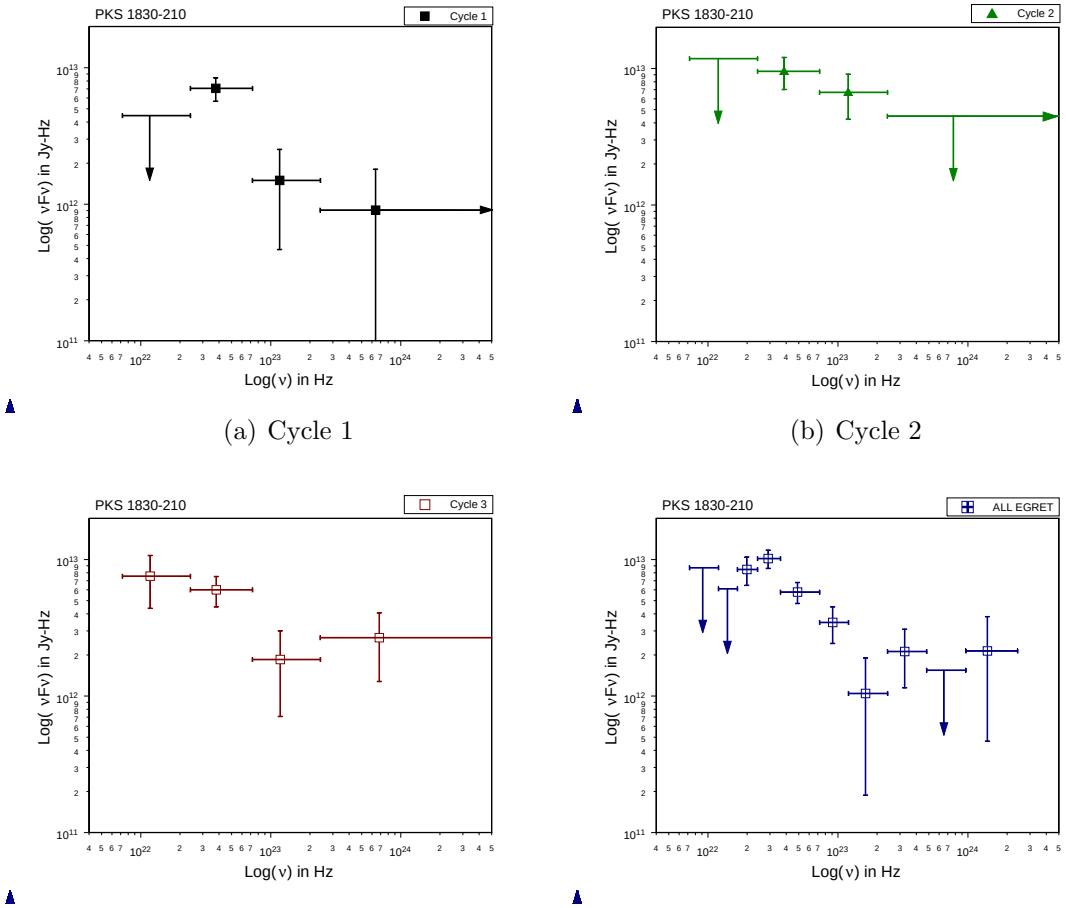

(a) Cycle 1

(b) Cycle 2

(c) Cycle 3

(d) Mission Average Spectrum

Figure 5.24: EGRET SED for 1830-210

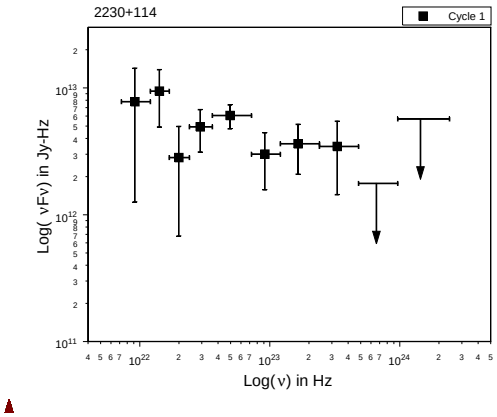

(a) Cycle 1

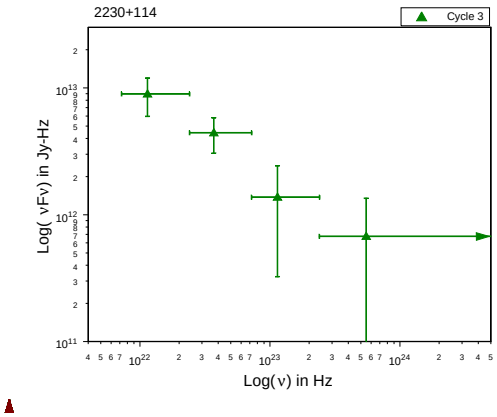

(b) Cycle 3

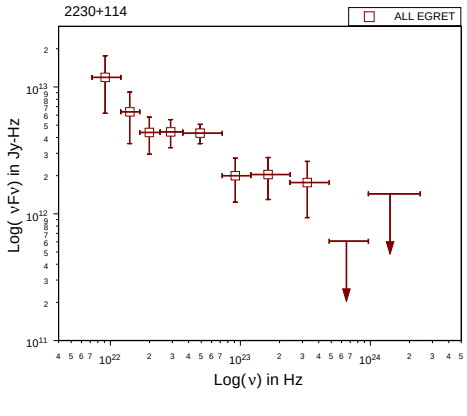

(c) Mission Average Spectrum

Figure 5.25: EGRET SED for PKS 2230+114

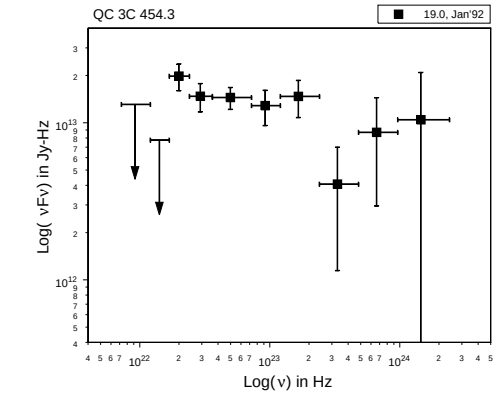

(a) Viewing Period 19.0

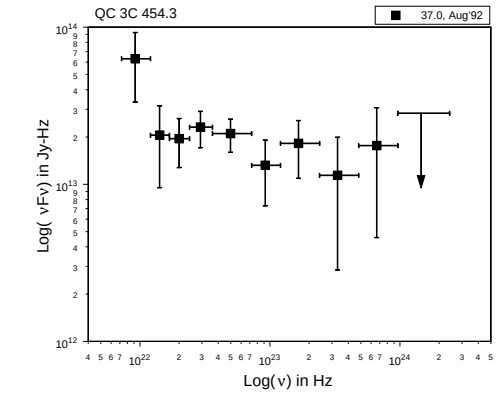

(b) Viewing Period 37.0

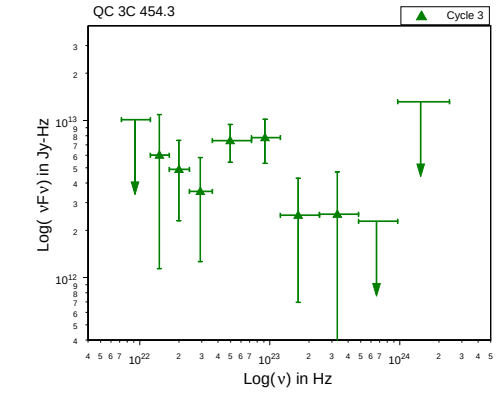

(c) Cycle 3

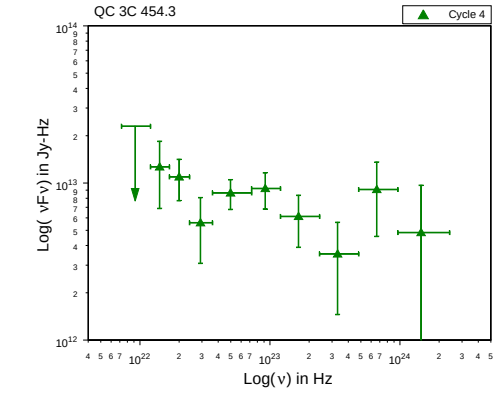

(d) Cycle 4

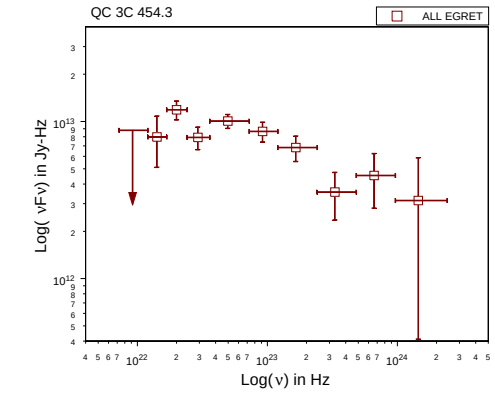

(e) Mission Average Spectrum

Figure 5.26: Multi-epoch νF_ν spectra for QC 3C 454.3

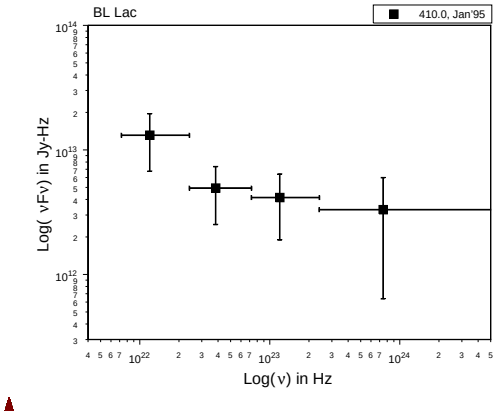

(a) Viewing Period 410.0

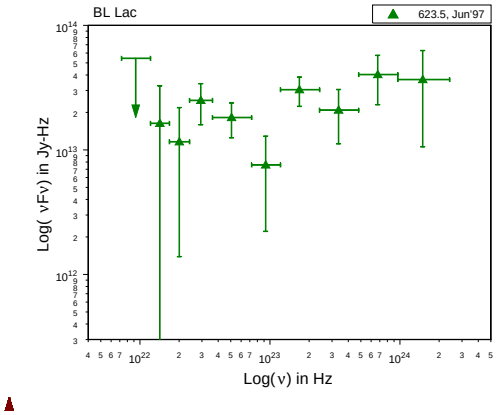

(b) Viewing Period 623.5

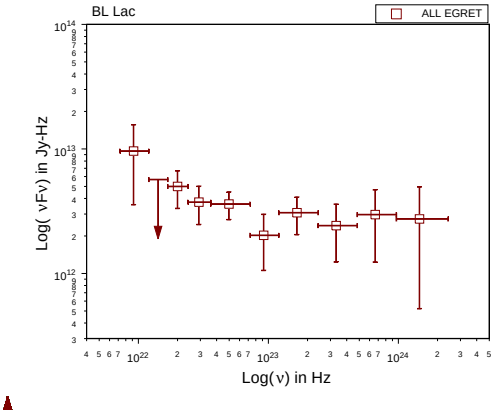

(c) Mission Average Spectrum

Figure 5.27: EGRET SED for BL Lac

Chapter 6

Future Research and Conclusion

6.1 Gamma Ray Large Area Space Telescope

The launch of the Gamma Ray Large Area Space Telescope will be a leap forward in blazar research due to the higher effective area, duty cycle, enhanced sensitivity due to use of better technology, when compared with EGRET. The physical mechanism driving photon detection is still based on pair production. There are three main components: Anticoincidence detector (ACD) that vetoes the charged particles, the tracker (which converts the photon into pairs and tracks them), and the calorimeter which absorbs the shower created by the incoming particles and determines the energy of the photon. Figure 6.1 shows a schematic view of the instrument.

EGRET had a spark chamber to convert photons and track the resulting electron positron pair. The gas quality deteriorated over time causing a degradation in the efficiency,and had to be refilled time to time. GLAST uses silicon strip detectors that do not have a degradation problem, with higher efficiency over a wide range of incidence angles. EGRET used two projected views of the spark chamber tracks to reconstruct the arrival direction of the photon, whereas the SSD detectors on LAT modules use three (x, y, and z) coordinates to track the position of the particles. This leads to a more accurate particle trajectory computation.

EGRET had a $\sim$ 30% probability of photon producing a pair in the spark chamber. The remaining 70% of the photons were lost. GLAST's calorimeter has the ability to determine the arrival direction of these photons that do not convert in the tracker. The angular resolution however is poorer. But this a substantial

improvement in efficiency from EGRET.

One of EGRET's limitations was the high rate of rejection of good events at high energies due to vetoing by the anticoincidence dome. The ACD on GLAST avoids this problem by segmenting the ACD into individual tiles [114] to accept a greater fraction of photons above 10 GeV.

The effective area of LAT is much higher than that of EGRET. Figure 6.2 shows the comparison between the effective area of GLAST and EGRET. EGRET had an effective area of ~ 1500 cm^2 between 100 MeV and 1 GeV. GLAST has an effective area of about 2000 cm^2 at 20 MeV which increases to about 8000 cm^2 1 GeV and stays roughly constant till 100 GeV. And, finally, LAT has approximately 4 times larger field of view (~ 2 Sr) than EGRET. In the first few years, LAT will be operated in the scanning mode. Consequently there will be more data available for each source. All these factors translate to ~ 30 times increase in sensitivity and a decrease in the lowest flux that can be detected form blazars. The largest integration time for which spectral measurement was possible with EGRET was for 3C 279 which was observed for 7 viewing periods (Table 3.2) during Cycle 6 when the flux was at its lowest value that could be detected by EGRET. The flux during this period (a ~ 50 days) was $\sim 4 - 5 \times 10^{12}$ Jy-Hz (see figure 5.2, or $4 - 5 \times 10^{-11}$ ergs cm^{-2} s^{-1}. The lowest flux that can be detected during first year of GLAST observations is $\gtrsim 10^{-12}$ ergs cm^{-2} s^{-1} (figure 6.3), an improvement by a factor of $\sim 40 - 50$.

6.2 What can we do with GLAST?

In our comprehensive EGRET analysis (discussed in chapter 3 and chapter 4, also in Nandikotkur et. al. 2007), 26 of the 98 blazars were observed multiple times and were bright enough to perform spectral variability studies. The study revealed several new results which differed substantially from previous analyses: We did not

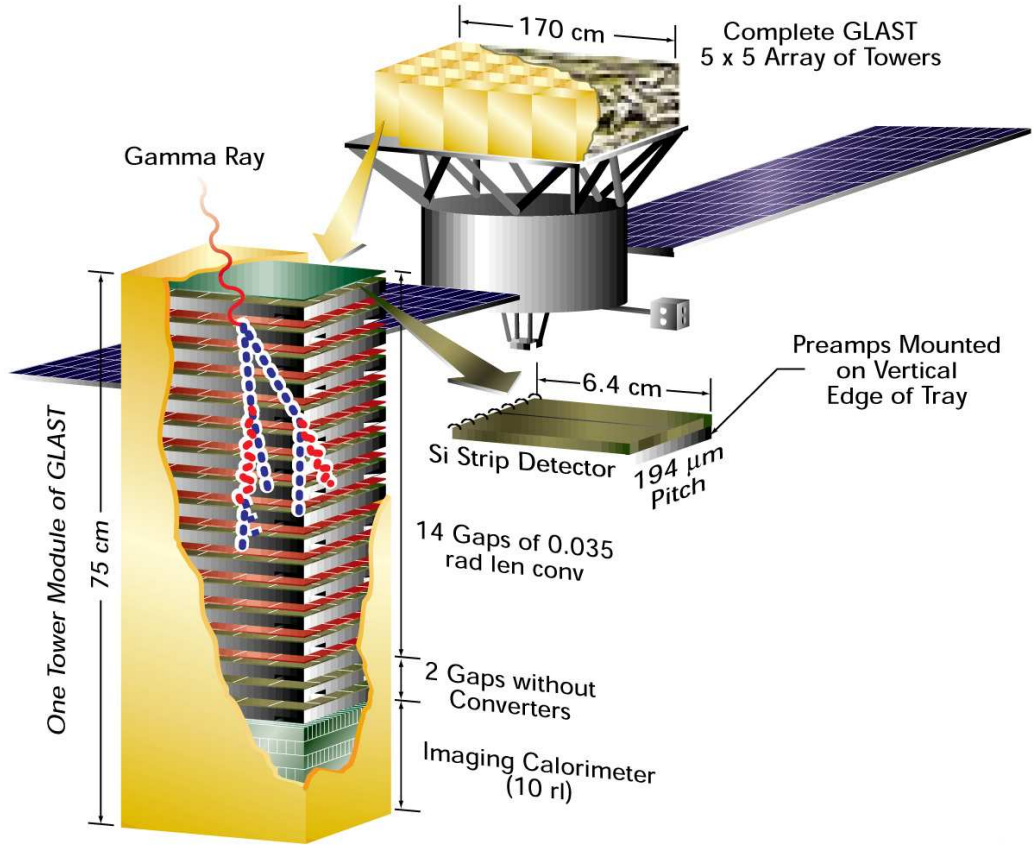

Figure 6.1: Schematic view of GLAST

find the spectral hardening observed during the first two cycles in PKS 0528+134 and during the flare from PKS 1622-297. However, there were indications of several interesting features (see details below) that were observed, but requiring substantially improved sensitivity to be confirmed or rejected. In order to investigate the details of those features with the 30-times improved sensitivity of GLAST, we propose to analyze the publicly available light curve and time-dependent spectral data for FSRQs (PKS 0208-512, PKS 0528+134, 0827+243, OJ 287, 3C 273, 3C 279, PKS 1406-076, PKS 1510-089, PKS 1622-297, 1633+382, 1730-130 and 3C454.3) and LBLs (PKS 0235+164, S5 0716+714, 1219+285, 2200+420) on the list of LAT monitored sources.

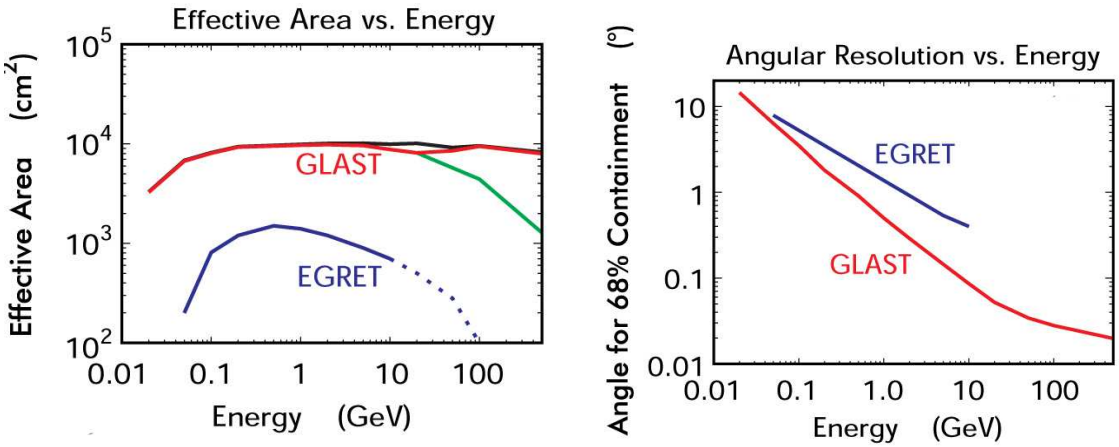

(a) Comparison between effective area of GLAST and EGRET

(b) Comparison between 68% containment cones

Figure 6.2: Comparison between GLAST and EGRET

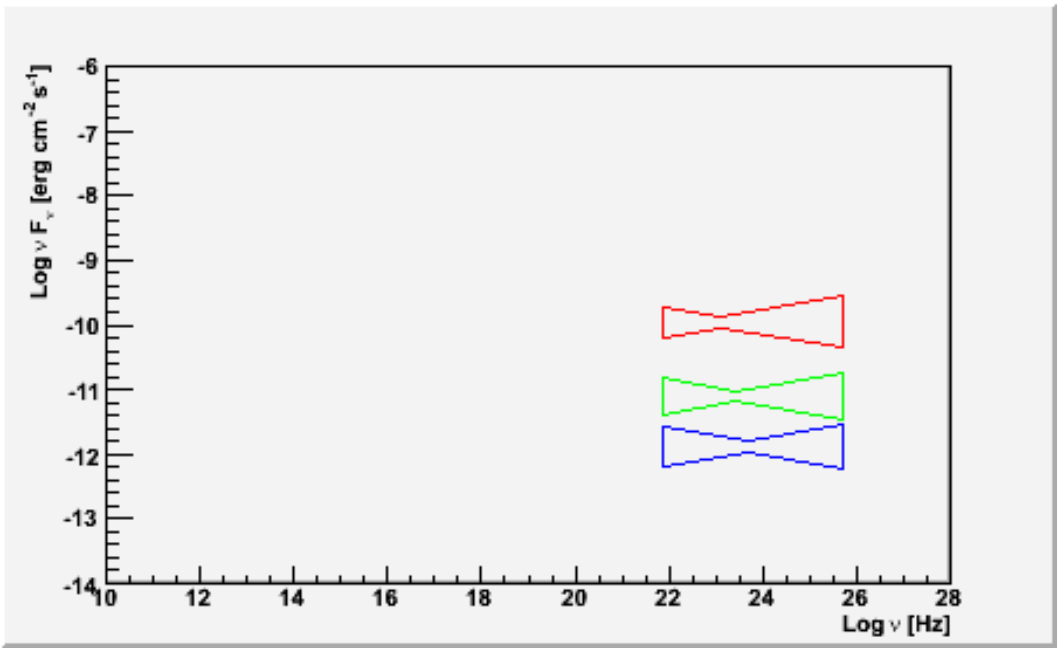

Figure 6.3: GLAST's sensitivity. Picture taken from the LAT instrument performance website http://www-glast.slac.stanford.edu/software/IS/glast_lat_performance.htm. The three bow tie plots shown are the minimum flux needed for a 20% determination of flux, 8 σ, detection and 6% determination in spectral index. after one-day, one-month and one-year observation by GLAST.

6.2.1 Short Term Spectral Variability

We observed a hint of a previously unreported counterclockwise hysteresis at weekly timescales in the spectral index vs. flux space in the 3 FSRQs PKS 0528+134,

PKS 1406-076, and PKS1622-297, which were observed for at least 4 contiguous viewing periods during a major flaring episode. The flux profiles of these sources were very different from each other. Figure 1 shows the light curve and spectral hysteresis plot for PKS 0528+134. A possible explanation for this may be the emergence of an EC component near the onset of the flare, dominating the SED at MeV – GeV energies. As the flare evolves and the emission region moves out, the intrinsically harder SSC radiation might take over, leading to a hardening of the spectrum as the flux is decreasing. With its increased sensitivity GLAST will be able to capture flares at a much higher time resolution. The largest flare in 3C 279 was characterized by average νF_ν flux values in the range $(2 - 9) \times 10^{-10}$ ergs cm^{-2} s^{-1}. Based on the LAT sensitivity information [a], a study of spectral hysteresis during individual flares could indicate if we are dealing with global, structural changes (including, e.g., a change of the bulk Lorentz factor), or with factors related to the co-moving electron dynamics (electron acceleration/cooling) (Kusunose et al. 2000 [87]; Böttcher, & Chiang 2002 [84]). GLAST should be able to give an 8 σ detection with a 6 % error on the spectral index in a time interval between $\sim$ a few hours and 1 day. In most FSRQs, major flares tend to last for several days, so that GLAST should provide a sufficient number of data points with sufficiently small error bars to clearly establish the presence or absence of hysteresis patterns. We plan to systematically isolate the principal light curve (covering the whole range of energy) for all the FSRQs and LBLs into individual flares and examine the spectral hysteresis pattern. If spectral hysteresis is found, we will examine the dependence of the loop behavior on the light curve profiles. Isolating clean flares at any resolution could still be a problem due to the intrinsic self-similarity in blazar variability (found at other wavelengths) which could not be seen in gamma-rays due to limited sensitivity of EGRET, but would definitely be seen with GLAST. For example, the 15 day flare

[a] http://www-glast.slac.stanford.edu/software/IS/glast_lat_performance.htm

shown in Figure 1 could be composed of several outbursts of a few days each, or the envelope of such a large flare could be superposed with several micro flares of smaller time scales. One way around it could be to smooth out the micro flares by adaptive rebinning while examining hysteresis pattern at larger time scales. A systematic study of the entire (1996 – 2006) RXTE data from Mrk 421 (Nandikotkur et al. in prep. a) has demonstrated that such a process reveals hysteresis patterns at the larger timescale.

Another important improvement with GLAST would be the detection of flares at lower peak fluxes which might be dominated by the SSC process alone and could have the opposite rotation direction than the larger flares. Since the SSC process is expected to be the dominant process in LBLs, as opposed to a mixture of EC and SSC processes in the case of FSRQs, classifying differences between the hysteresis patterns in FSRQs and LBLs will be a useful effort. The hysteresis pattern could also be different depending on the where the frequency at which the spectral index is evaluated is located in relation to the peak of the inverse-Compton bump. This has been predicted for HBLs for the frequency range near the synchrotron peak (Kirk et al. 1998 [113]) however, the predictions for FSRQs and LBLs near the inverse-Compton peak are not clear. The LAT instrument team will make light curves in roughly 10 energy bins publicly available. We will investigate the frequency dependence of the hysteresis by taking two spectral indices (or hardness ratios) calculated from the sets of light curves at low and high energies.

Previous studies (Hartman et al. 2001 [115]) have showed that gamma-ray flares also differ from each other in their correlations with the optical flares. We plan to use the available public databases, e.g. the Tuorla monitoring program [b] and the WEB Telescope resource [c] to perform correlation studies to complement our classification from spectral studies.

[b] http://users.utu.fi/kani/1m/index.html
[c] http://www.to.astro.it/blazars/webt/gasp/list.html

6.2.2 Long Term Spectral Variability

6.2.2.1 Overall Trend?

Of the 24 FSRQs and LBLs whose spectral variability and spectral index vs. flux correlation we examined, 16 objects did not show any overall trend (Pearson's correlation coefficient < 0.8). The prominent ones among these, 3C 279, 3C 273, PKS 0528+134, PKS 1622-297, PKS 0208-512, PKS 1406-076, 3C 454.3 and S5 0716+714, are all included in the list of LAT monitored sources. Three sources of this list showed a hysteresis behavior during flares, but there was no long term trend when all the data were analyzed together. Some of the blazars did not show any statistical evidence for variability due to large error bars and fewer observations. Part of this problem was due to the limited sensitivity of EGRET. With GLAST in the scanning mode, there will enough observations ($\gtrsim 50$, during Cycle 1). to conduct this study to achieve a statistical significance. Using publicly available spectral information, we will be able to address a few crucial questions: Is there a limit to the range of spectral variations? Is there a statistically significant difference in the spectral distributions of individual blazars? Given the variability of each blazar, would one be able to see a difference in spectral distributions between FSRQs and LBLs?

6.2.2.2 Spectral softening with Flux?

Figure 2 shows the spectral index – flux plots for 3C 279 and PKS 0208-512, which were extensively observed by EGRET. The trend at low fluxes is extremely interesting: The spectral index softens with increasing flux, an effect that was never

previously observed. In the case of PKS 0208-512, however, there is a clear sign of spectral hardening with increasing flux after the initial softening. Blazars undergo frequent outbursts, but are expected to spend 85 % of the time in the quiescent state (Achatz et al. 1990). Given the mixed results from results in Chapter 3, (spectral softening with increasing flux in some, hardening in others, lack of an overall trend in some, and the effect mentioned above) the question of how the spectrum looks when the source is in a quiescent state is still a very open question. This can be readily addressed with the proposed analysis of GLAST data. The lowest flux for which the EGRET 3C 279 data (which showed the largest variation observed for any blazar), yielded a spectral index was $\sim 18 \times 10^{-8}$ photons cm^{-2} s^{-1}. The νF_ν spectrum (Figure 3) is above 10^{12} JyHz. This should be achievable within a month of GLAST observations if the source is in its lowest state any time during the next cycle, for an 8 σ detection and a 6 % error on spectral index. Given the uniformly sampled light curves from GLAST, the question whether there is "a quiescent state", i.e. a flux state below which blazars spend more than 85 % of time, can be addressed within the first year. Although the source might not flare to its previous levels, we should definitely be able to address the softening at low fluxes.

6.2.2.3 Is it a Power Law?

3a) External Compton Contribution: The EGRET data for FSRQs and LBLs could be adequately fit with a simple power law due to the large error bars, but some deviations from a power law can seen in the νF_ν plots, which can be interpreted as the emergence of the EC component. Figure 3 shows all the broadband spectra for 3C 279 and PKS 0208-512 from the EGRET mission. EGRET's limited sensitivity did not allow a systematic study of this deviation using broken power law models, but we will attempt to quantify the deviation from power law, and track

the evolution of the EC and the SSC component in the GLAST data. Measuring correlations between the light curves in the two branches of the power law would then tell us if the same population of electrons are involved in the gamma-ray emission.

3b) MeV Blazars: Leaving traces at Low GLAST energies The blazars PKS 0208-512, PKS 1510-089, PKS 0528+134, and 3C 273 are all strong MeV emitters. Their spectra are expected to have a break around 1 – 30 MeV. Taking the rapid nature of blazar variability, there is an outside chance that this break could move into the GLAST regime, and this should reveal itself in our spectral studies. In fact, PKS 0028-512, does not seem to show a falling spectrum in Figure 3. Moreover, the MeV emission shows an occasional anticorrelation with GeV emission at EGRET energies (Collmar et al. 1997) during an MeV flare. We will test for this by examining correlations between the light curves above and below ~ 200 MeV.

We will use publicly available day-scale light curves from SWIFT and ASM (RXTE) (which will be simultaneous with GLAST) to get an estimate of the MeV break. Although the X-ray range used will be far from the MeV region, the spectral break still shows the difference between MeV blazars and other FSRQs (Nandikotkur et al. 2001 [117]). High quality X-ray data (simultaneous with GLAST) from PCA will also be available due to the proposed RXTE schedule which will allow us to calculate the spectral break at high temporal resolution.

3c) Spectrum above 1 GeV The latest extragalactic γ-ray background (EGRB) spectrum shows convex curvature with a break at around 2 GeV (Strong et al. 2004). The index below the break is 2.24 ± 0.01 which is very close to 2.25 ± 0.03, the average spectral index of all the blazars observed by EGRET (see-section 3.4.2.1). If blazars are the sole contributors to EGRB, then replicating the convex curvature would require a hardening in the spectral index with increasing flux (Stecker &

Salamon 1996), for which we do not find any strong evidence in the entire EGRET data. There is no reason from a theoretical standpoint to expect a convex break in the blazar spectrum near 2 GeV. GLAST's increased effective area will allow us to measure accurately the shape of the blazar spectrum above 2 GeV, which was impossible with EGRET, because of a high rejection rate of events due to self-vetoing effects.

4 TIME SCALES OF VARIABILITY

With its regularly sampled light curves at an unprecedented resolution in γ-rays, GLAST will allow us to explore variability at multiple timescales. We will use *Structure Functions* (Simonetti et. al. 1985 [127]) to identify the various timescales on which blazars vary. Previous studies for EGRET blazars were possible only during flares, using raw light curves (Nandikotkur et. al. 1997a [86] & 1997b [126]). A cross structure function analysis between light curves of the high and low energy GLAST bands will shed light on any systematic link between the two.

6.2.3 Spectral Variability in HBLs

Search for the break: We propose to do a systematic and comprehensive spectral study of all the GLAST data from all the HBLs, Mrk 421, PKS 2155-304, Mrk 501, 1ES 1426+428, 1ES 2344+514, 1ES 1959+650 and look for the convex break. The flux in any individual bin recorded for Mrk 421 (from Figure 1 and 2) is between $\sim 10^{12} - 10^{13} JyHz$, or $10^{-11} - 10^{-10}$ ergs cm^{-2} sec^{-1} which can be achieved by GLAST within 2-3 weeks[d]. One month of operation achieves a 8 sigma detection if the SED lies just above 10^{-11} ergs cm^{-2} sec^{-1}, for a 6% determination of the spectral index, which can easily distinguish between the soft and hard states. The GLAST data will include $\sim$ 10 light curves over the complete energy band.

[d]http://www-glast.slac.stanford.edu/software/IS/glast_lat_performance.htm

In addition to tracking the spectral indices for the whole range, we will extract spectral information for the intervals below and above the break (which could be $\sim 200 - 400 MeV$) from a subset of these light curves.

Correlation between energy bands: A convex break in the HBL spectrum is perplexing from the point of view of theoretical models. Simple calculations (Nandikotkur et al. 2007b [121]) show that none of the external Compton processes can give rise to a steep spectrum in HBLs at EGRET/GLAST energies, as it would require the two inverse -Compton peaks (one at low MeV and another already existing one at TeV) and seed photons with such a large separation in frequencies are not available in the blazar environment. While a convex break in the electron energy distribution (EED) can reproduce the spectrum, it would require a positive correlation between the low and high energy branches of the gamma-ray spectrum. But we observe the contrary in Figure 1, where during Cycle 3 (V+ 322.0) the soft low energy EGRET SED has disappeared, while the hard high energy EGRET component is very pronounced. We will examine the correlation between the two sets of light curves above and below the break, to track the evolution of the soft and hard components. Hysteresis in the hardness ratio vs. flux (total) space is a convenient way to study the relative variation of the two light curves.

While multiwavelength efforts are useful in extracting physical parameters associated with blazar emission, a comprehensive and systematic study of spectral and temporal variability focused on the γ-ray range, is crucial in helping identify, classify and quantify the spectral characteristics and time scales in individual blazars, and examine the differences between them. The ensemble of results expected from the study will set a large framework that will guide theoretical efforts and complement

the multiwavelength efforts. Such a study was was possible only after the EGRET mission was over. However, considering the unprecedented spectral and temporal resolution of GLAST and the volume of data that it will generate, a systematic study early on during the mission is a worthwhile effort. Although the volume of data that we propose to analyze is large, the data is going to be in FITS format that will allow us to run the standard ftools (including XRONOS for hardness ratio calculations) in addition to the ftools that will be made public. We will use the experience gathered during the multi-step analysis of large volumes of RXTE data (Nandikotkur et al. in prep.(a) [128]) to develop a processing pipeline that will streamline the process.

Bibliography

[1] Urry, C. M., and Padovani, P., 1995, *Publications of the Astronomy Society of the Pacific*, 107, 715

[2] Terlevich, R., et al., *The Monthly Notices of the Royal Astronomical Society*, 255, 713

[3] Fritz, J., et al., 2006, *The Monthly Notices of the Royal Astronomical Society*, 366, 767

[4] Krolik, J. H., & Begelman, M. C., 1988, *The Astrophysical Journal*, 329, 702

[5] Rees, M. J., 1966, *Nature*, 211, 468

[6] Ghisellini, G., et al., 1993, *The Astrophysical Journal*, 407, 65

[7] Blandford, R., and Znajek, R. L., *The Monthly Notices of the Royal Astronomical Society*, 179, 433

[8] Hartman, R. C., et al. 1999, *The Astrophysical Journal, Supplement Series*, 123, 79

[9] Punch, M, et al., 1992, *Nature*, 358, 477

[10] Quinn, J., et al., 1996, *The Astrophysical Journal, Letters*, 456, L83

[11] Giommi P., and Padovani P., 1994, *The Monthly Notices of the Royal Astronomical Society*, 268, L51

[12] Fossati, G., et al., 1998, *The Monthly Notices of the Royal Astronomical Society*, 299, 433

[13] Sambruna, R. M., Maraschi, L., & Urry, C. M. 1996, *The Astrophysical Journal*, 463, 444

[14] Ghisellini, G., Maraschi, L., & Treves, A., *Astronomy and Astrophysics*, 146, 204, 1985

[15] Maraschi, L., Ghisellini, G., & Celotti, A., *The Astrophysical Journal*, 397, L5, 1992

[16] Marscher, A.P., & Gear, W.K. 1985, *The Astrophysical Journal*, 298, 114

[17] Bloom S. D., & Marscher, A. 1996, *The Astrophysical Journal*, 461, 657

[18] Dermer, C.D., Schlickeiser, R., & Mastichiadis, A. 1992, *Astronomy and Astrophysics*, 256, L27

[19] Dermer, C.D., & Schlickeiser, R. 1993, *The Astrophysical Journal*, 416, 458

[20] Sikora M., Begelman M. C., & Rees, M. J. 1994, *The Astrophysical Journal*, 421, 153

[21] Blandford, R., & Levinson A. 1995, *The Astrophysical Journal*, 441, 79

[22] Dermer, C.D., Sturner, S.J., & Schlickeiser, R. 1997, *The Astrophysical Journal*s, 109, 103

[23] Ghisellini, G., & Madau, P. 1996, *The Monthly Notices of the Royal Astronomical Society*, 280, 67

[24] Sikora M., et al. 2002, *The Astrophysical Journal*, 577, 78

[25] Blażejowski, M., et al. 2000, *The Astrophysical Journal*, 545, 107

[26] Wagner, S. J., et al. 1995, *Astronomy and Astrophysics*, 298, 688

[27] Ghisellini, G., et al. 1998, *The Monthly Notices of the Royal Astronomical Society*, 301, 451

[28] Mannheim, K., 1993, *Astronomy and Astrophysics*, 221, 211

[29] Mannheim, K., & Biermann, P. l., 1992, *Astronomy and Astrophysics*, 252, L21

[30] Mücke, A., et al. 2003, Astropart. Phys., 18, 593

[31] Aharonian, F., 2000, *New Astron.*, 5, 377

[32] Mücke, A., & Protheroe, R. J., 2000, *AIP Conf. Proc.*, 515,149

[33] Rachen, J., & Meszaros, P., 1998, *Physical Review, D*, 58, 123005

[34] Mücke, A., & Protheroe, R. J., 2001, *Astroparticle Physics*, 15, 121

[35] Böttcher, M., 2007, Proceedings of "The Central Engine of Active Galactic Nuclei", Xi'An, China, 2006, *ASPCS*, in press.

[36] Mukherjee, R., et al. 1997, *The Astrophysical Journal*, 490, 116

[37] von Montigny, C., et al., 1995, *The Astrophysical Journal*, 440, 525

[38] Hartman, R. C., et al. 2001, *The Astrophysical Journal*, 553, 683

[39] Mukherjee, R., et al. 1999, *The Astrophysical Journal*, 527, 132

[40] E. B. Hughes, et al., 1980, *IEEE Transactions of Nuclear Science*, *NS-27*, 364

[41] Bertsch, D. L., 1984 *Advanced Space Research*, *3*, 515.

[42] D. A. Kniffen., 1989, *Annual NY Academy Science No. 571, 14th Texas Symp. on Relativistic Astrophysics* ed. E. J. Fenyves New York, AIP, 482

[43] G. Kanbach, et al. 1988, *Space Sciences Review*, *49*, 69

[44] G. Kanbach. 1989, *Proc. Gamma-Ray Observatory Sci. Workshop*, 2-1, ed. W. N. Johnson, Greenbelt, NASA

[45] R. C. Hartman, et al. 1979, *Astrophysical Journal*, *230*, 597

[46] Thompson, D. J., et al., 1993, *The Astrophysical Journal, Supplement Series*, 86, 629

[47] Mattox, J.R., et al., 1996, *The Astrophysical Journal*, 461, 396

[48] Hunter, S. D., et al., 1997, *The Astrophysical Journal*, 481, 205

[49] Esposito, J. A., et al., 1999, *The Astrophysical Journal, Supplement Series* , L23, 203

[50] Mukherjee, R., et al., 1996, *The Astrophysical Journal*, 470, 831

[51] Bertsch, D. L., et al., 2001, *Gamma 2001*, ed. Ritz, S., Gehrels, N., Shrader, C. R., AIP conference Proceedings , 587

[52] Mattox, J.R.. et al., 1997, *The Astrophysical Journal*, 476, 692

[53] Jahoda, K. M., et al., 1996, SPIE, 2808, 59J

[54] Jahoda, K. M., et al., 2006, *The Astrophysical Journal, Supplement Series* ,163,401

[55] Dickey, J. M., and Lockman, F. J., 1990, *Annual Review of Astronomy and Astrophysics*, 28, 215

[56] Hink, P., Pelling, M., and Rothschild, R. E., 1992, *SPIE*, V1743, 140

[57] Rothschild, R. E., Pelling, M. R., Gruber, D. E., and Matteson, J. L., *SPIE*, 1159, 139, 1989

[58] Vermeulen, R. C., & Cohen, M. H., 1994, *The Astrophysical Journal*, 430, 467

[59] Mukherjee, R., et al. 1995, *The Astrophysical Journal*, 445, 189

[60] Sreekumar, P., et al. 1996, *The Astrophysical Journal*, 464, 628

[61] Bloom, S. D., et. al. 1997, *The Astrophysical Journal*, 490, L145

[62] Stacy, J. G., Vestrand, W. T., & Sreekumar, P. 2003, *The Astrophysical Journal*, 598, 216

[63] Sreekumar, P., et al. 2001 in in Gamma 2001, ed. Ritz, S., Gehrels, N., Shrader, C. R., AIP conference Proceedings, 587, 314

[64] Sreekumar, P., et al. 1998, *The Astrophysical Journal*, 494, 523

[65] Stecker, F. W., & Salamon, M. H. 1996, *The Astrophysical Journal*, 464, 600

[66] Mukherjee, R., et al. 1999, *The Astrophysical Journal*, 527, 132

[67] Hartman, R. C., et al. 1997, Proceedings of the Fourth Compton Symposium, AIP Conference Proceedings, 410, 307

[68] Ballo, L., et al. 2002, *The Astrophysical Journal*, 567, 50

[69] Böttcher, M., & Bloom, S. D. 2000, *The Astronomical Journal*, 119, 469

[70] Kataoka, J., et al. 2002, *The Monthly Notices of the Royal Astronomical Society*, 336, 932

[71] Chiappetti, L., et al. 1999, *The Astrophysical Journal*, 521, 552

[72] Kataoka, J., et al. 2000, *The Astrophysical Journal*, 528, 243

[73] Aharonian, F., et al. 2001, *The Astrophysical Journal*, 559, 187

[74] Takahashi, T., et al. 2000, *The Astrophysical Journal*, 542, L105

[75] Krawczynski, H., et al. 2001, *The Astrophysical Journal*, 559, 187

[76] Tavecchio, F., et al. 2001, *The Astrophysical Journal*, 554, 725

[77] Kataoka, J., et al. 1999, *The Astrophysical Journal*, 514, 138

[78] Krawczynski, H., Coppi, P., & Aharonian, F.A. 2002, *The Monthly Notices of the Royal Astronomical Society*, 336,721

[79] Petry, D., et al. 2000, *The Astrophysical Journal*, 536, 742

[80] Lin, Y. C., et al. 1999, *The Astrophysical Journal*, 525, 191

[81] Skibo J. G., Dermer, C.D., & Schlickeiser, R.C. 1997, *The Astrophysical Journal*, 483, 56

[82] Blom, J. J., et al. 1995, *Astronomy and Astrophysics*, 298, L33

[83] Collmar, W., et al. 1997, *Astronomy and Astrophysics*, 328, 33

[84] Böttcher, M., & Chiang, J. 2002, *The Astrophysical Journal*, 581, 127

[85] Li, H. & Kusunose, M. 2000, *The Astrophysical Journal*, 536, 729

[86] Nandikotkur, G., M.S. thesis, Iowa State University, 1997

[87] Kusunose, M., Takahara, F., & Li, H. 2000, *The Astrophysical Journal*, 536, 299

[88] Takahashi, T., et al. 2000, *The Astrophysical Journal*, 542, L105

[89] Sembay, S., et al. 1993, *The Astrophysical Journal*, 404, 112

[90] Gliozzi, M., et al. 2006, astro-ph/0603693

[91] Cui, Wei., 2004, *The Astrophysical Journal*, 605, 662

[92] Sambruna et al. 2006, ApJ, 646, 23

[93] Georganopoulos, M., & Kazanas, D. 2003, *The Astrophysical Journal*, 594, L27

[94] Strong, A. W., Moskalenko, I. V., & Reimer, O., 2004, *The Astrophysical Journal*, 613, 956

[95] Chiang, J., & Mukherjee, R. 1998, *The Astrophysical Journal*, 496, 754

[96] Mücke, A., & Pohl, M. 2000, *The Monthly Notices of the Royal Astronomical Society*, 312, 177

[97] Ghisellini, G., et al. 1999, *Astronomy and Astrophysics*, 348, 63

[98] Hartman, R. C., et al. 1999, *The Astrophysical Journal*s, 123, 79

[99] Hughes, E. B., et al. 1980, IEEE Trans. Nucl. Sci., NS-27, 364

[100] Kanbach,G., et al. 1988, Space Sci. Rev., 49, 69

[101] Schonfelder V., et al. 2000, *The Astrophysical Journal*s, 143, 145

[102] Blażejowski, M., et al. 2005, *The Astrophysical Journal*, 630, 130

[103] Nandikotkur, G., et al., 2007, *The Astrophysical Journal*, 657, 706

[104] Carson, J., et al. 2007, *The Astrophysical Journal*, 662, 199

[105] Lichti, G. et al. http://arxiv.org/pdf/0704.2338

[106] Aharonian, F., et al. 2005, *Astronomy and Astrophysics*, 430, 865

[107] Georganopoulos, M. Kirk, J. G., & Mastichiadis, A. 2001, *The Astrophysical Journal*, 561, 111

[108] Costamante, L. & Ghisellini, G. 2002, *Astronomy and Astrophysics*, 384, 56

[109] Perlman, E. S., et al. 2005, *The Astrophysical Journal*, 625, 727

[110] Guilbert, P. W., Fabian, A. C., & Rees, M. J. 1983, *The Monthly Notices of the Royal Astronomical Society*, 205, 593

[111] de Jager, O. C., et al. 1996, *The Astrophysical Journal*, 457, 253

[112] Ghisellini, G. 1998, Astroparticle Physics, 11, 11

[113] Kirk, J. G., Rieger, F. M., & Mastichiadis, A. 1998, *Astronomy and Astrophysics*, 333, 452

[114] Moiseev, A. A., et al., 2007, *Astroparticle Physics*, 25, 339

[115] Hartman, R. C., et al. 2001, *The Astrophysical Journal*, 558, 583

[116] Achatz, U., et al., 1990, *Astronomy and AStrophysics*, 233, 391

[117] Nandikotkur, G., et al., in *Gamma 2001*, AIP Conference Proc., 2001

[118] Nandikotkur, G., et al.,(in prep.a), "A comprehensive study of spectral Hysteresis in Mrk 421 using RXTE data from 1996-2006."

[119] Collmar, W., et al., 2000, *Astronomy and Astrophysics*, 354, 513

[120] Nandikotkur, G,, et al, 2007AAS...210.0226N

[121] Nandikotkur, G., et al., Submitted to ApJ

[122] Hartman, R. C., et al., 1992, *The Astrophysical Journal*, 382, L1

[123] Thompson, D. J., et al., 1995, *The Astrophysical Journal, Supplement Series*, 101, 259

[124] Thompson, D. J., et al., 1996, *The Astrophysical Journal Supplement Series*, 107, 257

[125] Böttcher, M., Mause, H., and Schlickeiser, H., 1997,*Astronomy and Astrophysics* ,324, 395

[126] Nandikotkur, G., Sreekumar, P., & Carter-Lewis, D., 1997b, Proc. of IVth Compton symposium.

[127] Simonetti, J. H., et al., 1985, *The Astrophysical Journal*, 296, 46

[128] Nandikotkur, G., et al.,(in prep.a), "A comprehensive study of spectral Hysteresis in Mrk 421 using RXTE data from 1996-2006."